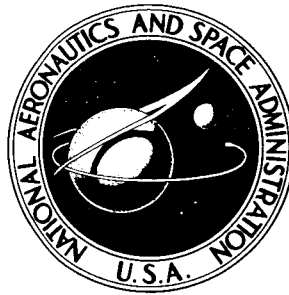


NASA TECHNICAL NOTE

NASA TN D-3890

NASA TN D-3890



N 67 19843

FACILITY FORM 602

(ACCESSION NUMBER)	(THRU)
110	None
(PAGES)	(CODE)
	31
(INASA CR OR TMX OR AD NUMBER)	
(CATEGORY)	

STABILITY CHARACTERISTICS OF THE APOLLO COMMAND MODULE

by William C. Moseley, Jr., Robert H. Moore, Jr.,
and Jack E. Hughes

Manned Spacecraft Center
Houston, Texas

STABILITY CHARACTERISTICS OF THE
APOLLO COMMAND MODULE

By William C. Moseley, Jr., Robert H. Moore, Jr.,
and Jack E. Hughes

Manned Spacecraft Center
Houston, Texas

NATIONAL AERONAUTICS AND SPACE ADMINISTRATION

For sale by the Clearinghouse for Federal Scientific and Technical Information
Springfield, Virginia 22151 - CFSTI price \$3.00

ABSTRACT

Investigations have been made to determine the static and the dynamic stability characteristics of the Apollo command module with and without surface protuberances and cavities at angles of attack from 0° to 360° , as necessary. The tests covered Mach numbers from 0.2 to 18.73. It was shown that design placement of the center of gravity can provide, within limits, the necessary entry lift-to-drag ratio while still maintaining stability. Static stability data showed an undesirable trim point, apex forward, at angles of attack between 10° and 50° . Test results indicated that the command module generally has positive damping in the entry flight attitude except at low subsonic Mach numbers.

CONTENTS

Section	Page
SUMMARY	1
INTRODUCTION	1
SYMBOLS	2
FACILITIES AND MODELS	4
Test Facilities	4
Models	4
TEST TECHNIQUES AND ACCURACY	5
Test Techniques	5
Accuracy of Data	6
RESULTS AND DISCUSSION	6
Static Stability Characteristics	7
Dynamic Stability Characteristics	9
CONCLUDING REMARKS	11
REFERENCES	13

TABLES

Table		Page
I	TEST FACILITIES AND CAPABILITIES	15
II	MODELS AND TEST RANGES	16
III	TEST CONDITIONS	17
IV	DATA ACCURACY	20

FIGURES

Figure		Page
1	Sketch showing body system of axes	21
2	Sketch of Apollo CM	
	(a) Block I configuration without protuberances	22
	(b) Block I configuration with protuberances	23
	(c) Block II configuration without protuberances	24
	(d) Block II configuration with protuberances	24
3	Typical photographs of Apollo CM test models	
	(a) Photograph of 0.105-scale model of the clean Apollo CM in the 9- by 7-foot test section of the Ames UPWT	25
	(b) Photograph of 0.90-scale model of the Apollo CM	26
	(c) Photograph of 0.059-scale model of Apollo CM (with protuber- ances) mounted on transverse rod in NAA-TWT facility	27
4	Sketch showing model installation for free-to-tumble dynamic tests	28
5	Aerodynamic characteristics of the Apollo CM (without protuber- ances) obtained at Ames UPWT at $M = 0.7$ to 3.40	
	(a) Pitching-moment coefficient, apex, $M = 0.7$ to 1.35	29
	(b) Pitching-moment coefficient, apex, $M = 1.55$ to 3.40	30
	(c) Pitching-moment coefficient, c.g. $\left(\frac{x}{d} = -0.657, \frac{z}{d} = 0.035\right)$, $M = 0.7$ to 1.35	31
	(d) Pitching-moment coefficient, c.g. $\left(\frac{x}{d} = -0.657, \frac{z}{d} = 0.035\right)$, $M = 1.55$ to 3.40	32
	(e) Normal-force coefficient, $M = 0.7$ to 1.35	33
	(f) Normal-force coefficient, $M = 1.55$ to 3.40	34
	(g) Axial-force coefficient, $M = 0.7$ to 1.35	35
	(h) Axial-force coefficient, $M = 1.55$ to 3.40	36
	(i) Lift coefficient, $M = 0.7$ to 1.35	37
	(j) Lift coefficient, $M = 1.55$ to 3.40	38
	(k) Drag coefficient, $M = 0.7$ to 1.35	39
	(l) Drag coefficient, $M = 1.55$ to 3.40	40
6	Aerodynamic characteristics of the Apollo CM (without protuber- ances) obtained at NAA-TWT at $M = 0.2$ to 3.5	
	(a) Pitching-moment coefficient, apex	41
	(b) Pitching-moment coefficient, c.g. $\left(\frac{x}{d} = -0.657, \frac{z}{d} = 0.035\right)$	42

Figure	Page
	43
	44
	45
	46
7 Aerodynamic characteristics of the Apollo CM (without protuberances) obtained at AEDC-A, -B, and -C facilities at M = 3.0 to 10.0	
(a) Pitching-moment coefficient, apex	47
(b) Pitching-moment coefficient, c.g. ($\frac{x}{d} = -0.657$, $\frac{z}{d} = 0.035$)	48
(c) Normal-force coefficient	49
(d) Axial-force coefficient	50
(e) Lift coefficient	51
(f) Drag coefficient	52
8 Aerodynamic characteristics of the Apollo CM (without protuberances) obtained at JPL-20SWT and JPL-21HWT at M = 0.7 to 9.0	
(a) Pitching-moment coefficient, apex, M = 0.7 to 3.26 (flagged symbols denote data for an alternate configuration)	53
(b) Pitching-moment coefficient, apex, M = 4.0 to 9.0 (flagged symbols denote data for an alternate configuration)	54
(c) Pitching-moment coefficient, c.g. ($\frac{x}{d} = -0.657$, $\frac{z}{d} = 0.035$), M = 0.7 to 3.26 (flagged symbols denote data for an alternate configuration)	55
(d) Pitching-moment coefficient, c.g. ($\frac{x}{d} = -0.657$, $\frac{z}{d} = 0.035$), M = 4.0 to 9.0 (flagged symbols denote data for an alternate configuration)	56
(e) Normal-force coefficient, M = 0.7 to 3.26 (flagged symbols denote data for an alternate configuration)	57
(f) Normal-force coefficient, M = 4.0 to 9.0 (flagged symbols denote data for an alternate configuration)	58
(g) Axial-force coefficient, M = 0.7 to 3.26 (flagged symbols denote data for an alternate configuration)	59
(h) Axial-force coefficient, M = 4.0 to 9.0 (flagged symbols denote data for an alternate configuration)	60
(i) Lift coefficient, M = 0.7 to 3.26 (flagged symbols denote data for an alternate configuration)	61
(j) Lift coefficient, M = 4.0 to 9.0 (flagged symbols denote data for an alternate configuration)	62

Figure	Page
(k) Drag coefficient, $M = 0.7$ to 3.26 (flagged symbols denote data for an alternate configuration)	63
(l) Drag coefficient, $M = 4.0$ to 9.0 (flagged symbols denote data for an alternate configuration)	64
9 Aerodynamic characteristics of the Apollo CM (without protuberances) obtained at AEDC-H and CAL-48ST facilities at $M = 15.8$ and 18.73 ($\frac{x}{d} = -0.657$, $\frac{z}{d} = 0.035$)	
(a) Pitching-moment and normal-force coefficients	65
(b) Axial-force, lift, and drag coefficients	66
10 Aerodynamic characteristics of the Apollo CM (with and without protuberances) obtained at AEDC-A at $M = 2.0$ and 6.0 ($\frac{x}{d} = -0.657$, $\frac{z}{d} = 0.035$)	
(a) Pitching- and rolling-moment coefficients, $M = 2.0$	67
(b) Pitching- and rolling-moment coefficients, $M = 6.0$	68
11 Comparison of aerodynamic characteristics of the Apollo CM, with and without protuberances, obtained at Ames UPWT at $M = 0.7$ to 3.4	
(a) Pitching-moment coefficient, apex, $M = 0.7$ to 1.2	69
(b) Pitching-moment coefficient, apex, $M = 1.35$ to 3.4	70
(c) Pitching-moment coefficient, c.g. ($\frac{x}{d} = -0.657$, $\frac{z}{d} = 0.035$), $M = 0.7$ to 1.2	71
(d) Pitching-moment coefficient, c.g. ($\frac{x}{d} = -0.657$, $\frac{z}{d} = 0.035$), $M = 1.35$ to 3.4	72
(e) Normal-force coefficient, $M = 0.7$ to 1.2	73
(f) Normal-force coefficient, $M = 1.35$ to 3.4	74
(g) Axial-force coefficient, $M = 0.7$ to 1.2	75
(h) Axial-force coefficient, $M = 1.35$ to 3.4	76
(i) Lift coefficient, $M = 0.7$ to 1.2	77
(j) Lift coefficient, $M = 1.35$ to 3.4	78
(k) Drag coefficient, $M = 0.7$ to 1.2	79
(l) Drag coefficient, $M = 1.35$ to 3.4	80
12 Aerodynamic characteristics of the Apollo Block II CM (without protuberances) obtained at Ames UPWT at $M = 0.7$ to 3.4	
(a) Pitching-moment coefficient, apex	81
(b) Pitching-moment coefficient, c.g. ($\frac{x}{d} = -0.652$, $\frac{z}{d} = 0.044$)	82
(c) Normal-force coefficient	83
(d) Axial-force coefficient	84

Figure		Page
	(e) Lift coefficient	85
	(f) Drag coefficient	86
13	Comparison of aerodynamic characteristics of the Apollo Block II CM (with and without protuberances) obtained at Ames UPWT at $M = 3.0$ and 3.4 ($\frac{X}{d} = -0.652$, $\frac{Z}{d} = 0.044$)	
	(a) Pitching-moment and normal-force coefficients	87
	(b) Axial-force, lift, and drag coefficients	88
14	Longitudinal oscillatory stability derivatives for the Apollo CM (without protuberances) obtained at AEDC-A and -C facilities at $M = 2.5$ to 10.18	89
15	Longitudinal oscillatory stability derivatives for the Apollo CM (without protuberances) obtained at AEDC-A facilities at $M = 1.5$ to 3.00	90
16	Longitudinal oscillatory stability derivatives for the Apollo CM (with protuberances) obtained at NAA-TWT facility at $M = 0.5$ and 0.8	91
17	Longitudinal oscillatory stability derivatives for the Apollo CM (with umbilical fairing, vent, and surviving antenna) obtained at Ames 12-ft facility at $M = 0.3$ to 0.7	92
18	Comparison of C_m values obtained from static tests and dynamic (free-to-tumble) tests at $M = 0.2$ to 0.9	
	(a) Pitching-moment coefficient for $M = 0.2$ and 0.3	93
	(b) Pitching-moment coefficient for $M = 0.4$ and 0.5	94
	(c) Pitching-moment coefficient for $M = 0.7$	95
	(d) Pitching-moment coefficient for $M = 0.8$ and 0.9	96
	(e) Pitching-moment coefficient for $M = 0.4$, 0.5 , 0.8 , 1.55 , 1.59 , 1.98 , and 2.0	97
19	Summary of the longitudinal stability characteristics of the Apollo CM. Nominal c.g. of $\frac{X}{d} = -0.657$, $\frac{Z}{d} = 0.035$	98
20	Effect of c.g. variation of C_m , α_t , and $\frac{L}{D}$ for the Apollo CM	
	(a) $M = 1.35$	99
	(b) $M = 15.8$	100

STABILITY CHARACTERISTICS OF THE APOLLO COMMAND MODULE

By William C. Moseley, Jr., Robert H. Moore, Jr.,
and Jack E. Hughes*
Manned Spacecraft Center

SUMMARY

Investigations have been made to determine the static and the dynamic stability characteristics of the Apollo command module over a Mach number range of 0.2 to 18.73. The investigations included tests of the clean command module as well as tests of the refined vehicle with surface protuberances and cavities. The tests covered angles of attack between 0° and 360°, as necessary.

The hypersonic lift-drag ratio needed to control the flight path of the Apollo command module is obtained through a design which places the center of gravity in an off-set location, thus providing a trimmed entry angle of attack with the main heat shield forward. Through the Mach number range tested, it has been shown that, within limits, the lift-drag ratio necessary for entry can be obtained by proper placement of the center of gravity while still maintaining stability.

Static stability data indicate an undesirable trim point (apex forward) at angles of attack between 10° and 50°, which was especially prominent at subsonic speeds. A severe scattering of data resulted from a flow separation that was also associated with this angle-of-attack range.

Dynamic stability derivatives were obtained using forced-oscillation, limited free-oscillation, and free-to-tumble test techniques. The test results indicated that the command module generally has positive damping in the entry flight attitude, except at the low subsonic Mach numbers equal to or less than 0.7.

INTRODUCTION

The Apollo Spacecraft Program, with the ultimate goal of a lunar landing, was initiated by the National Aeronautics and Space Administration (NASA) as part of the continuing program of space exploration following Project Mercury and the Gemini Program. Initial study contracts, NASA Space Task Group studies, and other

*ITT/Federal Electric Corporation.

nonfunded studies established design requirements and specifications for the Apollo spacecraft. An integral part of these specifications was the selection of a configuration for development. Some of the early wind-tunnel studies that were used to support and verify this selection are reported in references 1 to 4.

The Apollo wind-tunnel testing program was established as part of the design and development program initiated in support of the Apollo Spacecraft Program. The total program, discussed more thoroughly in reference 5, was planned to yield design data on static and dynamic stability, aerodynamic heating, and aerodynamic loads and to thoroughly evaluate specific problems, such as interactions between separating bodies during normal or abort operations, jet-plume interactions or effects, and launch-vehicle suitability. The program had to provide the experimental data needed for efficient spacecraft design and for studies of all phases of the flight programs. The supporting programs had to be broad in scope and a wide variety of wind-tunnel facilities was needed because of the extremes in the operational spectrum of the flight programs and the wide range of Reynolds numbers for nominal and off-nominal flight conditions.

Investigations were made to determine the static and dynamic stability characteristics of the Apollo configurations. The purpose of this paper is to present the results of the stability studies on the Apollo command module (CM), which represents the entry configuration. Static stability data were determined for a Mach number range of 0.20 to 18.73 and for a large angle-of-attack range. Initial tests were made using the clean CM. Subsequently, tests were made using models with surface modifications. These modifications included antennas, umbilical fairing, vent protuberances, and window and tower-leg cavities. Dynamic stability studies were made over a Mach number range of 0.3 to 10.18 using forced-oscillation, limited-free-oscillation, and free-to-tumble techniques to determine the total pitch-damping derivative.

SYMBOLS

The positive direction of forces and moments and the body system of axes are illustrated in figure 1. The presented data are referred to both the body and stability systems of axes.

C_A	axial-force coefficient, $\frac{\text{axial force}}{q_\infty S}$
C_D	drag coefficient, $\frac{\text{drag}}{q_\infty S}$
C_L	lift coefficient, $\frac{\text{lift}}{q_\infty S}$
C_m	pitching-moment coefficient, $\frac{\text{pitching moment}}{q_\infty Sd}$

$C_{m,a}$	pitching-moment coefficient computed about theoretical apex
$C_{m,c.g.}$	pitching-moment coefficient computed about nominal center of gravity
$C_{m_q} + C_{m_{\dot{\alpha}}}$	damping-in-pitch parameter, $\frac{\partial C_m}{\partial \left(\frac{qd}{2V}\right)} + \frac{\partial C_m}{\partial \left(\frac{\dot{\alpha}d}{2V}\right)}$, per rad
$\overline{C_{m_q}} + \overline{C_{m_{\dot{\alpha}}}}$	average damping-in-pitch coefficient, over one full oscillation
C_{m_α}	pitching-moment curve slope parameter (measured at trim angle of attack), $\frac{\partial C_m}{\partial \alpha}$
C_N	normal-force coefficient, $\frac{\text{normal force}}{q_\infty S}$
C_Y	side-force coefficient, $\frac{\text{lateral force}}{q_\infty S}$
C_l	rolling-moment coefficient, $\frac{\text{rolling moment}}{q_\infty Sd}$
d	maximum body diameter, ft (154 in. full scale)
I	moment of inertia, ft-lb/sec ²
k	reduced frequency parameter, $\frac{\omega d}{2V}$
$\frac{L}{D}$	lift-drag ratio
M	free-stream Mach number
q	pitching angular velocity, rad/sec
q_∞	free-stream dynamic pressure, lb/sq ft
R	Reynolds number (based on maximum model diameter)
S	maximum cross-sectional area perpendicular to X body axis at maximum model diameter, sq ft
V	free-stream velocity, ft/sec

X, Y, Z	body reference axes
$\frac{x}{d}$	longitudinal location ratio of center of gravity measured from theoretical apex
$\frac{z}{d}$	vertical location ratio of center of gravity measured from centerline
α	angle of attack of model centerline, deg
$\dot{\alpha}$	rate of change of angle of attack, rad/sec
α_t	trim angle of attack, deg
β	angle of sideslip, deg
θ	angular displacement, rad
$\dot{\theta}$	angular velocity, rad/sec
$\ddot{\theta}$	angular acceleration, rad/sec ²
ω	circular frequency of oscillation, rad/sec

FACILITIES AND MODELS

Test Facilities

The broad range of expected flight conditions (extremes of Mach number, Reynolds number, and α) and the limitations of any single tunnel to simulate all these conditions dictated the use of a large number of wind-tunnel test facilities. All such facilities used to acquire stability data on the Apollo CM are listed in table I along with tunnel size and capability. The models and the ranges over which they were tested are outlined in table II. Test conditions, compiled by facility (when available), are listed in table III.

Models

The models used for the tests were constructed to precise scale, geometrically accurate, and machined to fine tolerances. The models varied from 0.020 to 0.105 scale of the Apollo CM. The Apollo CM without protuberances and with surface modifications (such as antennas, vent, umbilical fairing, and window and tower-leg cavities) is shown in figure 2. Tests were also made of models of the Apollo Block II CM. This model, without protuberances and with surface modifications, is shown in figures 2(c) and 2(d). This is a model of the lunar configuration with a truncated apex to simulate the latest Apollo Block II CM. Test models mounted in wind tunnels are

shown in figure 3. Model size was predicated on the tunnel size and on the capability of attaining simulation of desired flight conditions with minimum tunnel interference. Tunnel α sectors and balance systems are usually designed for small α ranges and for specified loading conditions. Selective model-mounting techniques made testing possible through the complete α range from 0° to 360° , as necessary. Balances were not readily adaptable to the large angle range required for the tests and were selected for the gross overall loading. Models were especially designed for use in more than one facility to allow efficient testing over the full range of expected Mach numbers and Reynolds numbers.

TEST TECHNIQUES AND ACCURACY

Test Techniques

Static stability tests. - Static force and moment tests were made using sting-mounted models attached to a strain-gage balance which measured the force and moment data. It was very difficult to measure the rolling moments to the desired accuracy. In some tests, the model or the balance was rotated 90° , so that the more sensitive side-force gages measured the normal force.

To test over the desired α range, a series of models was used. The models were identical except for the location of the balance cavities, which were positioned to allow different installations. Thus, variations were obtained in the angle between the axis of symmetry of the model and the balance axis. The basic angle range for the support systems was also adjustable and, with the various model offset angles, allowed testing over the complete α range from 0° to 360° , as necessary.

Dynamic stability tests. - Dynamic stability data were acquired by using the following test techniques:

- (1) Forced oscillation
- (2) Limited free oscillation
- (3) Free-to-tumble

A detailed discussion of the techniques and apparatus used for measuring dynamic stability parameters for a rigidly forced oscillation system may be found in reference 6. A method for reducing these aerodynamic characteristics to coefficient form is described in reference 7. Limited free-oscillation test techniques, apparatus, and data-reduction methods are given in reference 8.

The free-to-tumble technique is a method which allows statically balanced models, mounted on a transverse rod through the center of gravity (c.g.), to tumble freely through an α range from 0° to 360° . A typical model installation for this test technique is shown in figure 4. Some problems were encountered in designing a method of mounting the model on a system in which friction and interference had to be at a minimum. A gas-bearing support, similar to one used successfully in the limited free-oscillation tests at supersonic Mach numbers, failed because of galling under the

buffeting subsonic loading conditions. A method of mounting, using precision ball bearings, was designed; and this method proved to be satisfactory. It was determined that friction or tare damping generally contributed a fractional part of the aerodynamic damping of the system. Bench tests were made to determine the friction damping under load, and tare corrections were applied to the data. Input data for calculating the damping-moment coefficient are acquired by using the θ time history. This is done by applying the single-degree-of-freedom equation of motion where:

$$I\ddot{\theta} + \left(C_{m_q} + C_{m_{\dot{a}}}\right) \left(\frac{q_\infty S d^2 \dot{\theta}}{2V}\right) + C_{m_\alpha} q_\infty S d \theta = 0$$

If C_m were available from static tests and I were measured in advance, it would be found that $(C_{m_q} + C_{m_{\dot{a}}})$ is the only variable. The equation of motion could be solved by integration with assumed values for $(C_{m_q} + C_{m_{\dot{a}}})$ until the θ time histories were simulated. A more thorough discussion of this technique is found in reference 9.

Accuracy of Data

Standard statistical analyses of balance calibration data and data repeatability indicated certain accuracy tolerances of the force and moment coefficients. Available accuracy estimates are presented in table IV.

RESULTS AND DISCUSSION

The data are presented in standard coefficient form and are referred to both the body and stability systems of axes of the model (fig. 1). The system of axes about which the data are reduced defines $\alpha = 0^\circ$ as the apex or small-end-forward attitude of the CM. In general, the pitching-moment data are referenced about both the theoretical apex of the model, as shown in the figure, and a representative or nominal center of gravity. Data, referenced about a typical c.g., are presented to provide a comparison with pitching-moment data obtained in free-to-tumble tests and to give a more realistic representation of the moment data.

Static longitudinal stability characteristics of the clean configuration of the Apollo CM are presented in figures 5 to 9. These same data are shown in figures 10 and 11 for the CM, with certain protuberances and tower-leg cavities. Static longitudinal stability characteristics for the Apollo Block II CM are given in figures 12 and 13. Longitudinal oscillatory stability characteristics for the clean configuration of the Apollo CM are presented in figures 14 and 15. Like data appear in figures 16 and 17 for the CM with certain protuberances and tower-leg cavities. A comparison

is presented in figure 18 of pitching-moment coefficients (C_m) obtained from tests in which the models were mounted on a transverse rod (free-to-tumble test technique). In figure 19, summary curves are presented showing $\alpha_t \frac{L}{D}$ at α_t and pitching-moment curve slope at α_t plotted against Mach number. Figure 20 depicts the effect of c.g. location on C_m in the α_t region, α_t and $\frac{L}{D}$ at α_t for the Apollo CM at Mach number 15.8.

Static Stability Characteristics

The longitudinal stability characteristics of the clean CM at an α range of -5° to 190° are presented in figure 5 for a Mach number range of 0.70 to 3.40. These data were obtained at the Ames Unitary Plan Wind Tunnels. Test Reynolds numbers varied from 5.0×10^6 to 2.7×10^6 (based on CM maximum diameter). Aerodynamic characteristics are presented in figure 6 for the clean CM for a Mach number range of 0.2 to 3.5 and an α range of -15° to 195° . These data were obtained at the North American Aviation Trisonic Wind Tunnel (NAA-TWT) for a Reynolds number range of 2.2×10^6 to 16.2×10^6 (based on CM maximum diameter). The general trends of the data in the transonic speed range were as expected. The data did indeed indicate that an undesirable trim point exists for the CM at angles of attack between 10° and 50° and that this trim point shows its strongest influence at subsonic speeds.

Entry into the atmosphere when α is at or near 15° would result in excessive heating on areas of the CM that were not designed to withstand such temperature extremes. Also, entry under these conditions could result in excessive g-loads on the spacecraft occupants. Another serious problem, introduced by the possibility of capture in the undesirable trim attitude, is successful deployment of the earth-landing system. Proper deployment of the earth-landing system as well as successful jettisoning of the apex cover is dependent upon orientation of the vehicle with the main heat shield (or blunt face) forward.

Several studies were made of possible configuration modifications designed to eliminate the undesirable trim point (ref. 5). Another significant point indicated by the data is the rather severe scattering of the data at angles of attack between 40° and 80° at subsonic Mach numbers from 0.2 to 0.7. At Mach numbers equal to or greater than 0.9, the severe scatter seems to be eliminated. The scatter phenomenon appeared to be the result of a flow separation confined to Mach numbers equal to or less than 0.7. Observations of the model during tests indicated a rather violent vibration of the model over α range of 40° to 80° . In some instances, this vibration was intense enough to damage the balance assembly. The scatter of the data is also evident at Mach number 0.7 for the data presented in figure 8. The data of figure 6 include a range of Reynolds numbers, but no attempt has been made to correlate a Reynolds number effect for the range of Reynolds numbers over which data are available.

The aerodynamic characteristics of the clean CM are presented in figure 7 for a Mach number range of 3.0 to 10.0 and an α range of -20° to 200° . These data were obtained at the Arnold Engineering Development Center (AEDC) von Karman gas

dynamic facilities over a Reynolds number range of 0.7×10^6 to 2.98×10^6 (based on CM maximum diameter). Aerodynamic characteristics of the clean CM for a Mach number range of 0.7 to 9.0 and an α range of -25° to 205° are given in figure 8. These data were obtained at the Jet Propulsion Laboratory (JPL) 20-inch supersonic wind tunnel and JPL 21-inch hypersonic wind tunnel over a Reynolds number range of 0.625×10^6 to 1.17×10^6 (based on CM maximum diameter). The data presented in figure 8 include, by way of supplementation, some results from tests using a model with a slightly different configuration. The flagged symbols denote data for a model the same as the one illustrated in figure 2(a), except that the radius of the apex is increased from 9.15 inches (full scale) to 15.4 inches (full scale) for the alternate configuration. The data for the alternate configuration are in very good agreement with the data for the clean CM. The data from figures 7 and 8 show that no apparent effect results from increasing the Mach number from 3.0 to 10.0.

Static stability data obtained at hypervelocity speeds are presented in figure 9. The data at Mach number 15.8 were obtained at the Cornell Aeronautical Laboratory 48-inch shock tunnel, and the Mach number 18.73 data were obtained at the AEDC-H tunnel. The data obtained at Mach number 18.73 were acquired over a limited α range near α_t . This was considered the most important area over which data were required.

Some of the Apollo flight vehicles will have protuberances (such as antennas, vent, and umbilical fairing) that will induce roll because of their location in the air-stream and because of their asymmetrical shape. Consequently, tests were conducted on models with these protuberances. The rolling-moment coefficient C_l and the C_m for the Apollo CM with surviving antenna are presented in figure 10. The C_m data show α_t as approximately 153.6° at Mach number 2.0. A small decrease in C_l with angle of sideslip β was evident as α was increased near α_t for a β -range of $+5^\circ$ to -14° , as discussed in reference 10.

Pitching-moment characteristics of the clean CM presented in figure 10(b) for Mach number 6.0 show an α_t of approximately 158.8° . This α_t compares with an α_t of 156° for the CM with umbilical fairing. The data for the clean CM (fig. 10(b)) indicate that the variation of C_l with respect to β is generally similar at $\alpha = 147^\circ$ and at $\alpha = 160^\circ$. There is, however, a small negative increment resulting from increasing α to 160° .

Static stability characteristics are presented in figure 11 for the Apollo CM (with antennas, vent, umbilical fairing, and tower-leg cavities, as shown in fig. 2) for a Mach number range of 0.7 to 3.5 and an α range of 80° to 125° . Static stability data for the CM with protuberances were not obtained for all Mach numbers and angles of attack. It was determined by comparison that the addition of protuberances did not materially affect the aerodynamic characteristics of the vehicle, except for pitching moment and rolling moment. These results generally confirmed pretest postulations and obviated additional testing, since static stability data for the clean configuration could

be used to supplement data for the CM with protuberances. For purposes of comparison and evaluation, data also appear in figure 11 for the clean configuration over a corresponding α range and speed range.

The static longitudinal stability characteristics of the clean Apollo Block II CM are given in figure 12 for an α range of 105° to 175° and a Mach number range of 0.7 to 3.4. In addition, data for the Apollo Block II CM, with protuberances, at Mach numbers 3.0 and 3.4 are presented in figure 13. The data indicate that the addition of the protuberances (umbilical fairing, antenna, and air vent) and tower-leg cavities had little or no effect on the aerodynamic characteristics except for the C_m about the nominal c.g. ($\frac{x}{d} = -0.652$, $\frac{z}{d} = 0.044$).

The basic concept of the Apollo entry configuration allowed for c.g. placement in entry module design as the method for providing a trimmed α and associated trimmed $\frac{L}{D}$ for flight path control. A summary of the longitudinal stability characteristics for the clean configuration of the Apollo CM is presented in figure 19. These data are referenced about a typical c.g. ($\frac{x}{d} = -0.657$, $\frac{z}{d} = 0.035$), which will probably vary from that for an actual flight vehicle, but will be similar and representative. Generally, $C_{m\alpha}$ is constant with Mach number over a Mach number range of 3.0 to 18.0. Also, α_t is constant at speeds greater than Mach number 7.0. The $\frac{L}{D}$ at α_t is nominally 0.34 to 0.36 at Mach numbers greater than 4.0. Variations in c.g. location produce marked effects in the C_m of the Apollo CM. Some of these effects are illustrated in figure 20 for an α range of 100° to 180° at Mach number 15.8. The pitching-moment curve referenced about a c.g. location ($\frac{x}{d} = -0.657$, $\frac{z}{d} = 0.045$) shows a tendency to eliminate the trim point and indicates that there are limitations in controlling α_t by varying the c.g. location. It is also noted that α_t and $\frac{L}{D}$ at α_t vary from 149.5° and 0.47 (for $\frac{x}{d} = -0.607$, $\frac{z}{d} = 0.045$) to 164° and 0.27 (for $\frac{x}{d} = -0.707$, $\frac{z}{d} = 0.025$).

Dynamic Stability Characteristics

Dynamic stability characteristics were determined using three test techniques, as discussed in the section entitled, "Test Techniques." The forced-oscillation technique was used to make the initial tests in the program (refs. 11 to 15). Some results of the forced-oscillation testing are presented in figure 14. These data were obtained from tests run at the AEDC-A and -C tunnels for a Mach number range of 2.5 to 10.18 over an α range of -15° to 40° and 100° to 160° . Data reported in references 12 to 15 are not presented here, primarily because the configuration tested differs slightly from the production Apollo CM. (The apex radius is 15.4 inches, full scale, compared to 9.15 inches, full scale, for the production Apollo CM.) The data in figure 14 indicate that the CM generally has positive damping with a value

for $(C_{m_q} + C_{m_{\dot{\alpha}}})$ of less than 1 in the α_t region ($\alpha \approx 155^\circ$). Large values of positive damping also are indicated where α is near 0° (CM apex forward). A region of data scatter is indicated when α is near 160° for a Mach number of 6.0. These values were found to be a function of oscillation amplitude. The largest positive damping was associated with the lower values of oscillation amplitude, which were varied from $\pm 0.5^\circ$ to $\pm 2.7^\circ$.

Dynamic stability derivatives were also determined by using a technique of limited free oscillation. The models used in these tests were sting-mounted and were similar to those used in forced-oscillation tests. Some results of these studies are presented in figure 15. These data were measured at the AEDC-A tunnel over a Mach number range of 1.5 to 3.0 and an α range of 138° to 148° . The data indicate that the clean CM has positive damping at these angles of attack for oscillation amplitudes up to approximately 14° . Note that these data were obtained using different oscillation centers and that they indicate that variations in location of the oscillation center result in appreciable differences in the damping parameter.

Using existing test hardware, it was impossible to locate the oscillation center of the equipment on the c.g. of the vehicle and still maintain geometric similarity of model sizes properly commensurate with tunnel sizes. Attempts to establish some method of transferring the data from a test c.g. to a desired flight c.g. were inconclusive (refs. 13 to 15). Thus, it is difficult to compare the obtained results when different oscillation centers are used. One method proposed to eliminate the problem of oscillation center was a free-to-tumble test technique in which the model was mounted on a transverse rod that passed through the oscillation center. Associated problems then became paramount, namely tare damping and interference effects of the model support system. Static C_m data obtained with the transverse rod support compared to those obtained with the more conventional sting support indicated that the data were in general agreement (fig. 18).

Damping derivative data for the Apollo CM with protuberances, determined using the free-to-tumble test method, are presented in figures 16 and 17. These data were obtained at the Ames 12-ft pressure tunnel and the NAA-TWT at a Mach number of 0.3 to a Mach number of 0.8. The data are generally similar for both facilities and indicate that the CM has negative damping in the α_t region at Mach numbers equal to or less than 0.7. At the higher subsonic Mach number, the vehicle has positive damping in the α_t region. Tests also were made of the clean CM in the Langley Research Center spin tunnel. Observations and motion-picture-film studies indicate that the vehicle has negative damping at low subsonic speeds. The data reported in reference 13 show similar trends of the data with values of $(C_{m_q} + C_{m_{\dot{\alpha}}})$ near zero for the α_t region ($\alpha \approx 150^\circ$).

Some results of free-flight tests of the Apollo CM at Mach numbers up to 35 appear in reference 16. A comparison of free-flight and conventional wind-tunnel stability tests of the Apollo CM is presented in reference 17.

CONCLUDING REMARKS

Data were obtained to determine the dynamic and static stability characteristics of the Apollo command module. The following conclusions result from an analysis of these data.

- (1) The Apollo command module is designed with an offset center of gravity to provide a trimmed entry angle of attack (with the heat shield forward). This design provides the hypersonic lift-drag ratio needed for flight path control. It has been shown that center-of-gravity placement can provide, within limits, the lift-drag ratio necessary for entry while still maintaining stability through the Mach number range tested.
- (2) The static stability data showed an undesirable trim point, apex forward, at angles of attack between 10° and 50° . This trim point was especially prominent in the subsonic speed range. Associated with the angle range near the undesirable trim point was a flow separation that resulted in a severe scattering of the data.
- (3) In the entry angle-of-attack region, the test results indicate that the command module generally has positive damping except at the low subsonic Mach numbers (equal to or less than 0.7).

Manned Spacecraft Center

National Aeronautics and Space Administration

Houston, Texas, January 16, 1967

914-50-89-00-72

REFERENCES

1. Morgan, James R.; and Fournier, Roger H.: Static Longitudinal Aerodynamic Characteristics of a 0.07-Scale Model of a Proposed Apollo Spacecraft at Mach Numbers of 1.57 to 4.65. NASA TM X-603, 1961.
2. Pearson, Albin O.: Wind-Tunnel Investigation of the Static Longitudinal Aerodynamic Characteristics of Models of Reentry and Atmospheric-Abort Configurations of a Proposed Apollo Spacecraft at Mach Numbers from 0.30 to 1.20. NASA TM X-604, 1961.
3. Pearson, Albin O.: Wind-Tunnel Investigation of the Static Longitudinal Aerodynamic Characteristics of a Modified Model of a Proposed Apollo Atmospheric-Abort Configuration at Mach Numbers from 0.30 to 1.20. NASA TM X-686, 1962.
4. Fournier, Roger H.; and Corlett, William A.: Aerodynamic Characteristics in Pitch of Several Models of the Apollo Abort System from Mach 1.57 to 2.16. NASA TM X-910, 1964.
5. Moseley, William C., Jr.; and Martino, Joseph C.: Apollo Wind Tunnel Testing Program - Historical Development of General Configurations. NASA TN D-3748, 1966.
6. Braslow, Albert L.; Wiley, Harleth G.; and Lee, Cullen Q.: A Rigidly Forced Oscillation System for Measuring Dynamic-Stability Parameters in Transonic and Supersonic Wind Tunnels. NASA TN D-1231, 1962.
7. Campbell, John P.; Johnson, Joseph L., Jr.; and Hewes, Donald E.: Low-Speed Study of the Effect of Frequency on the Stability Derivatives of Wings Oscillating in Yaw with Particular Reference to High Angle-of-Attack Conditions. NACA RM L55H05, 1955.
8. Hodapp, A. E., Jr.: Free-Oscillation Dynamic Stability Tests of a 0.05-Scale Apollo Command Module and a 0.059-Scale Apollo Launch Escape Vehicle at Supersonic Speeds. AEDC-TDR-63-186, Sept. 1963.
9. Redd, Bass; Olsen, Dennis M.; and Barton, Richard L.: Relationship Between the Aerodynamic Damping Derivatives Measured as a Function of Instantaneous Angular Displacement and the Aerodynamic Damping Derivatives Measured as a Function of Oscillation Amplitude. NASA TN D-2855, 1965.
10. Jones, Jerry H.; Jenke, L. M.; and Lucas, E. J.: Force Tests on Apollo Configurations at Mach Numbers 1.5 through 6. AEDC-TDR-64-206, Oct. 1964.
11. Hodapp, A. E., Jr.; and Uselton, B. L.: Dynamic Stability Tests of a 0.045-Scale Apollo Command Module at Mach Numbers 2.5 through 6 and Mach Number 10. AEDC-TDR-63-52, Mar. 1963.

12. Kilgore, Robert A.; and Averett, Benjamin T.: Wind-Tunnel Measurements of Some Dynamic Stability Characteristics of 0.055-Scale Models of Proposed Apollo Command Module and Launch-Escape Configurations at Mach Numbers from 2.40 to 4.65. NASA TM X-769, 1963.
13. Averett, Benjamin T.; and Kilgore, Robert A.: Dynamic-Stability Characteristics of Proposed Apollo Configurations at Mach Numbers from 0.30 to 1.20. NASA TM X-912, 1964.
14. Averett, Benjamin T.; and Wright, Bruce R.: Some Dynamic-Stability Characteristics of Models of Proposed Apollo Configurations at Mach Numbers from 1.60 to 2.75. NASA TM X-971, 1964.
15. Averett, Benjamin T.: Dynamic-Stability Characteristics in Pitch of Models of Proposed Apollo Configurations at Mach Numbers from 0.30 to 4.63. NASA TM X-1127, 1965.
16. Sammonds, Robert I.: Forces and Moments on an Apollo Model in Air at Mach Numbers to 35 and Effects of Changing Face and Corner Radii. NASA TM X-1086, 1965.
17. Malcolm, Gerald N.; and Kirk, Donn B.: Comparison of Free-Flight and Conventional Wind-Tunnel Stability Tests for Apollo Command Module and Abort Configurations. NASA TM X-1137, 1965.

TABLE I. - TEST FACILITIES AND CAPABILITIES

Test facility	Size of test section	Mach number range	Reynolds number range $\times 10^{-6}$ /ft
Continuous tunnels			
Ames Unitary Plan Wind Tunnel (Ames UPWT)	8 by 7 ft 9 by 7 ft 11 by 11 ft	2.4 to 3.5 1.5 to 2.6 0.7 to 1.4	0.5 to 5 1 to 7 1 to 10
Ames 12-Foot Pressure Tunnel (Ames 12 ft)	12-ft diameter	0.0 to 0.95	0.5 to 9.0
Arnold Engineering Development Center			
Tunnel A (AEDC-A)	40 by 40 in.	1.5 to 6.0	0.3 to 9
Tunnel B (AEDC-B)	50-in. diameter	8.0	0.25 to 3.3
Tunnel C (AEDC-C)	50-in. diameter	10.0	0.29 to 2.5
Jet Propulsion Laboratory 20-Inch Supersonic Wind Tunnel (JPL-20SWT)	18 by 20 in.	1.3 to 5.0	0.4 to 6
21-Inch Hypersonic Wind Tunnel (JPL-21HWT)	21 by 15 to 28 in.	5.0 to 9.5	0.25 to 3.6
Langley Research Center 12-Foot Low-Speed Tunnel (LRC-12LST)	12 ft (octagonal)		
Langley Unitary Plan Wind Tunnel (LRC-UPWT)	Two 4- by 4-ft test sections	1.47 to 4.65	0.56 to 7.83
Lewis Research Center Supersonic Wind Tunnel (LeRC-SWT)	8 by 6 ft	0.8 to 2.1	4.15 to 8.5
North American Aviation, North American Aerodynamics Laboratory (NAA-NAAL)	7.75 by 11 ft	0.2	1.44
Impulse tunnels			
Arnold Engineering Development Corporation 50-Inch Hot Shot II (AEDC-H)	50-in. diameter	16.0 to 21.0	0.062 to 0.3
Cornell Aeronautical Laboratory 48-Inch Shock Tunnel (CAL-48ST)	48-in. diameter	5.0 to 18.0	0.03 to 10
Intermittent tunnel			
North American Aviation Trisonic Wind Tunnel (NAA-TWT)	7 by 7 ft	0.2 to 3.5	5 to 14

TABLE II. - MODELS AND TEST RANGES

Model	Scale	Facility	Mach number range	Reynolds number range $\times 10^{-6}$ (a)	α range, deg	Description	Test objective
Force, dynamic models							
FD-2	0.055	LRC-UPWT	1.5 to 2.8	0.628 to 3.98	134 to 158	CM with oscillation axis as near as possible to c.g. of full-scale vehicle	Determine dynamic stability characteristics of CM. Forced oscillations $\pm 2^\circ$ amplitude
FD-3	.045	AEDC-A AEDC-C	1.5 to 6.0 10.0	1.00 to 6.00 1.00	-15 to 164 -15 to 164	CM with oscillation center on the design c.g. and a model with oscillation center on model axis of symmetry	Determine dynamic stability characteristics of CM using forced-oscillation techniques
FD-5	.05	AEDC-A	1.5 to 6.0	0.31 to 3.56	147 \pm 18	CM with oscillation centers located at several c.g. positions	Define the dynamic stability characteristics of the CM
FD-6	.10	Ames 12-ft	0.03 to 0.8	2.2 to 7.6	0 to 360	CM with umbilical fairing, vent, and surviving antenna	Define the dynamic stability characteristics of the CM
FD-9	.059	NAA-TWT LeRC-SWT	0.5, 0.7, 0.8 1.59, 1.98	3.14 to 4.86 3.6	0 to 360	CM with all external protuberances including vent and umbilical fairing	Define the dynamic stability characteristics of the CM
Force, static models							
FS-1	0.02	JPL-20SWT	0.7	1.17	0 to 168	CM with sting cavity axis in several positions to allow changes in angle of attack	Determine static stability characteristics of the CM
FS-2	.105	Ames UPWT NAA-NAAL NAA-TWT Ames UPWT	0.7 to 3.5 0.184 0.26 0.2 to 3.5 0.7 to 1.35	3.4 to 5.0 1.77 2.49 2.2 to 16.2 3.5 to 4.9	-15 to 195 -10 to 180 -10 to 180 -15 to 95	Clean CM. All models were identical, except balance cavities were positioned to allow for 10 different balance installations in order to vary α	Determine static stability characteristics of the CM
FS-3	.45	AEDC-A AEDC-B AEDC-C	1.5 to 6.0 6.0 to 8.0 10.0	0.7 to 4.37 0.5 to 1.6 0.6 to 1.26	-10 to 360 -20 to 190 -8 to 206	Clean CM and CM with protuberances	Determine static stability characteristics of the CM
FS-4	.04	AEDC-H	18.7	0.085	120 to 180	Clean CM	Determine hypervelocity static stability characteristics of the Apollo CM
FS-7	.02	JPL-21HWT	5.0, 7.3, 9.0	0.29 to 0.884	-19 to 195	Clean CM	Determine static stability characteristics of the Apollo CM
FS-8	.05	CAL-48ST	15.75	0.079 to 1.08	-25 to 205	Clean CM	Define static stability at hypervelocity
FS-12	.09	AEDC-B AEDC-C	6.0, 8.0 10.0	2.53 to 3.7 0.9 to 2.53	195 to 165 195 to 165	Clean CM and CM with various combinations of protuberances	Define trim characteristics and protuberances roll effects

^aBased on model diameter.

TABLE III. - TEST CONDITIONS

Facility	Mach number	Reynolds number $\times 10^{-6}$ (a)	Stagnation pressure, psia	Dynamic pressure, lb/ft^2	Stagnation temperature, $^{\circ}\text{F}$
Dynamic tests					
Ames 12-ft	0.3	7.6		385.3	91.33
	.5	4.5		405.6	103.33
	.7	2.7		320.0	95.33
	.8	2.2		277.0	178.33
AEDC-A	1.49	3.15	25.1	624.66	
	2.00	3.26		644.22	
	2.49	2.8		932.5	92.0
	2.99	.38		96.104	
	3.00	2.40		610.20	
	3.00	3.1		906.3	104.0
	4.01	3.8		773.2	96.0
	5.99	3.6		459.3	179.0
AEDC-C	10.18	1.2	1600.0	329.1	1435.33
LeRC-SWT	1.59	3.6		1185	
	1.98	3.6		1280	
LRC-UPWT	1.60 1.80	2.44		787	
		1.06		341	
		2.28		737	
		3.67		1186	
		.97		309	
		2.48		789	
		3.95		1254	
		.72		221	
		2.56		787	
NAA-TWT	.5	3.14		411	
		4.53		640	
	.8	4.03		840	
	1.6	3.39		1185	
	2.0	3.39		1280	

^aBased on model diameter.

TABLE III. - TEST CONDITIONS - Continued

Facility	Mach number	Reynolds number $\times 10^{-6}$ (a)	Stagnation pressure, psia	Dynamic pressure, lb/ft ²	Stagnation temperature, °F
Static tests					
Ames UPWT					
8 by 7	2.6	3.6			
	3.0	3.9			
	3.4	3.6			
9 by 7	1.55	3.6			
	2.0	3.6			
	2.4	3.6			
11 by 11	.7	3.9			
	.9	3.3			
	1.1	2.9			
	1.2	2.8			
	1.35	2.7			
	.7	5.0			
	.9	4.3			
	.95	4.1			
	1.0	4.0			
	1.05	3.9			
	1.10	3.8			
	1.20	3.7			
	1.35	3.6			
AEDC-A	2.0	4.37	30.00	1562	100.33
	3.0	.7	9.15	229	56.5
		2.7	3.21	642	57.0
	4.0	2.4	5.12	532	58.5
	5.0	.7	2.52	117	60.5
	5.0	2.1	8.02	352	60.5
	6.0	1.9	12.00	270	66.0
	6.0	2.98	168.00	411	160.33
AEDC-B	8.0	.5	10.05	65	132
	8.0	.76	30.04	194	132
	8.0	1.6	65.20	410	132
	10.0	.6	180.2	383	190
		1.26	90.5	194	182

^aBased on model diameter.

TABLE III. - TEST CONDITIONS - Concluded

Facility	Mach number	Reynolds number $\times 10^{-6}$ (a)	Stagnation pressure, psia	Dynamic pressure, lb/ft ²	Stagnation temperature, °F
Static tests					
AEDC-H	18.73	.085	10.455	50	5988
CAL-48ST	15.75	.37	.0035	88.9	3140
JPL-20SWT	.7 1.65 2.41 3.26 3.99 5.01	1.17 .724 .724 .924 1.078 .758			
JPL-21HWT	5.0 7.3 9.0 7.33	.625 .844 .290 .84		440	
LeRC-SWT	1.59 1.98	3.6 3.6		1185 1280	
NAA-NAAL	0.184 .26	1.77 2.49		50 100	
NAA-TWT	.2 .2 .2 .4 .4 .7 .7 .9 1.2 3.5	2.2 2.8 6.4 6.6 11.0 8.1 13.0 9.0 9.6 16.2	17.0 21.5 49.0 25.0 42.1 16.0 24.7 15.5 9.3 1.3	70 91 207 403 667 848 1311 824 1328 1597	

^aBased on model diameter.

TABLE IV. - DATA ACCURACY

Facility	Mach number	Accuracy of					
		M	deg	C _m	C _N	C _A	C _L
Ames UPWT	± 0. 001	± 0. 1		± 0. 0060 ±. 0004	± 0. 0080 ±. 001	± 0. 0080 ±. 002	± 0. 0080 ±. 003
AEDC-B and -C				±. 064	±. 092	±. 121	±. 114
AEDC-H	18. 7	± .05		±. 055	±. 007	±. 0046	±. 10
CAL-48ST				±. 0001	±. 0060	±. 0050	
JPL-21HWT	7. 33		± .1	±. 0027	±. 003	±. 0050	±. 010
NAA-NAAL	. 185			±. 0014	±. 002	±. 003	±. 003
NAA-NAAL	. 26					±. 002	±. 002
NAA-TWT							
Reynolds number:							
2. 2	. 2	± .005	±. 035	±. 025	±. 047	±. 039	±. 011
2. 8	. 2			±. 023	±. 023	±. 031	±. 097
6. 4	. 2			±. 010	±. 014	±. 016	±. 013
6. 6	. 4			±. 005	±. 007	±. 008	±. 007
6. 6	. 4			±. 004	±. 005	±. 004	±. 010
8. 1	. 7			±. 002	±. 003	±. 003	±. 003
9. 0	. 9			±. 002	±. 003	±. 002	±. 004
9. 6	1. 2			±. 002	±. 003	±. 002	±. 004
16. 2	3. 5			±. 002	±. 003	±. 002	±. 005

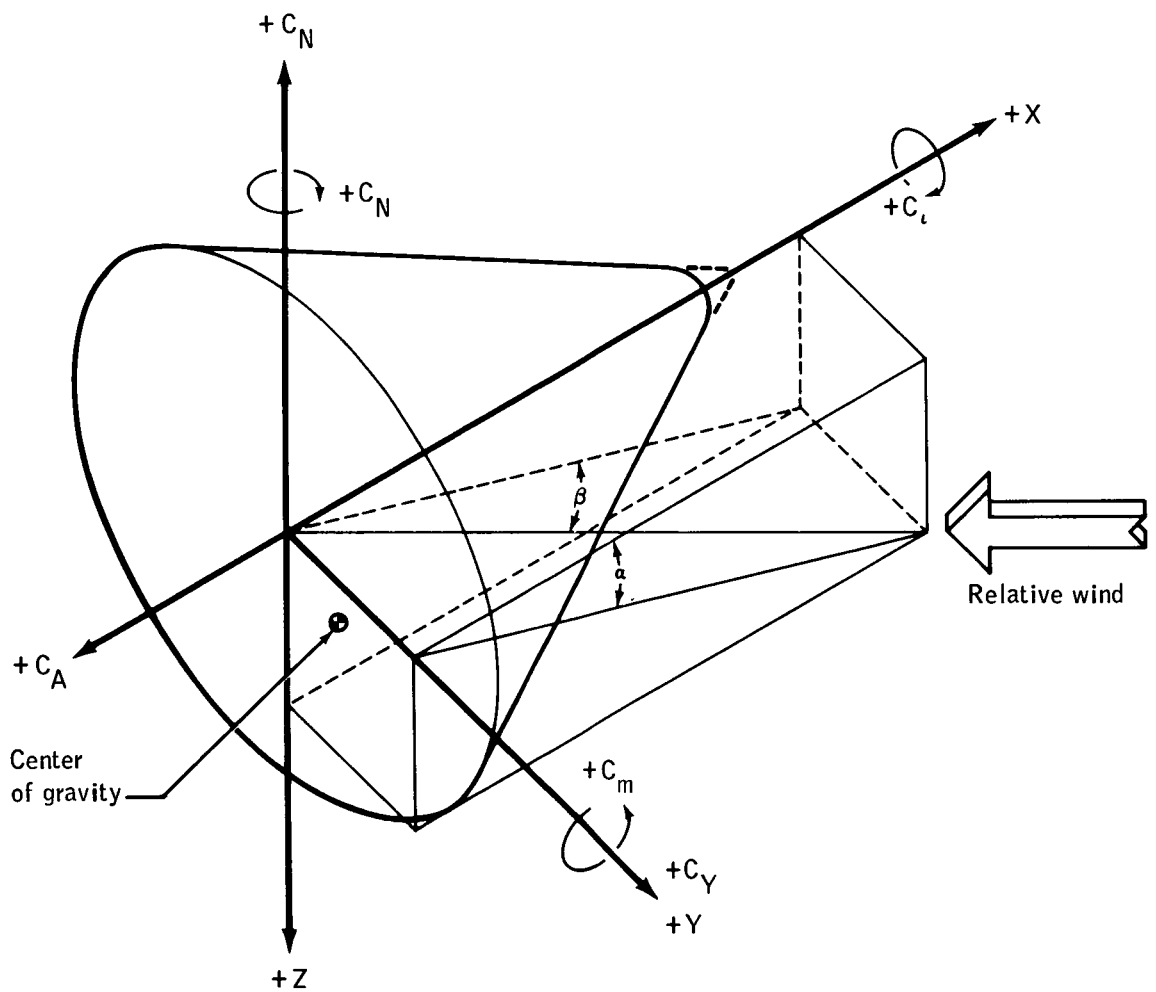
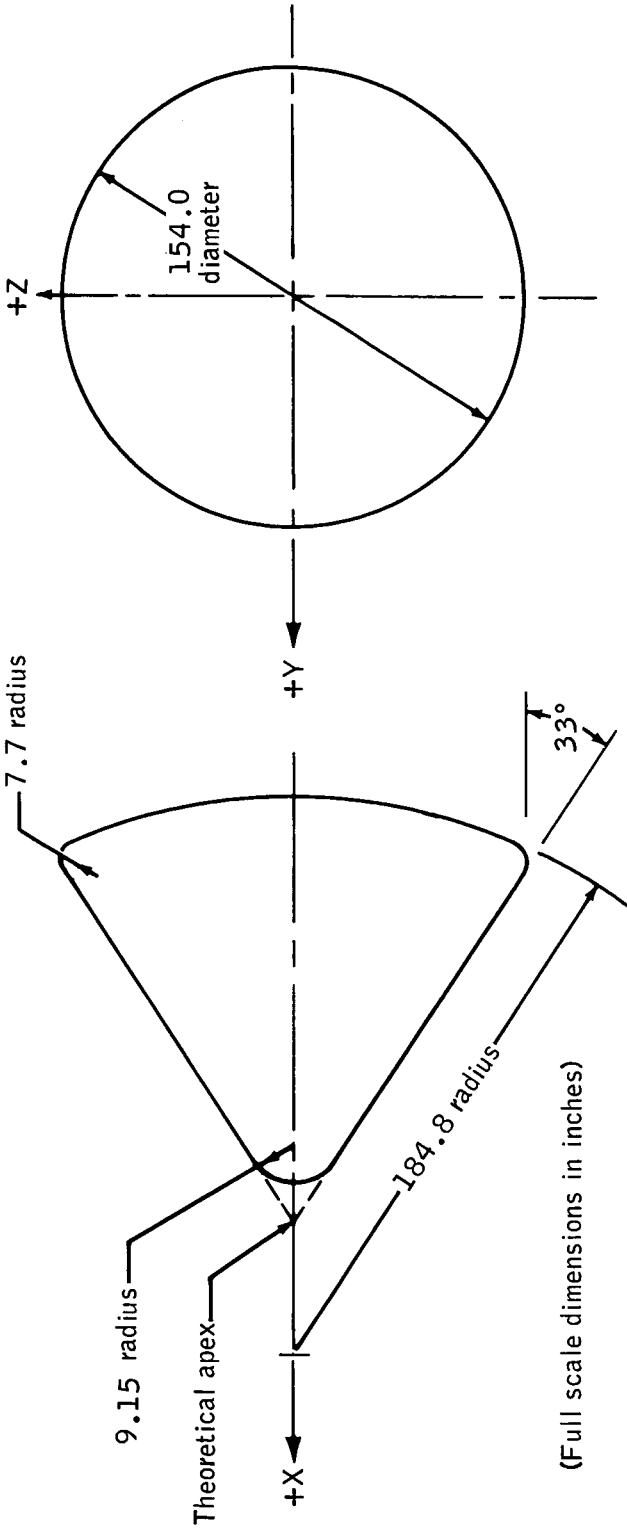
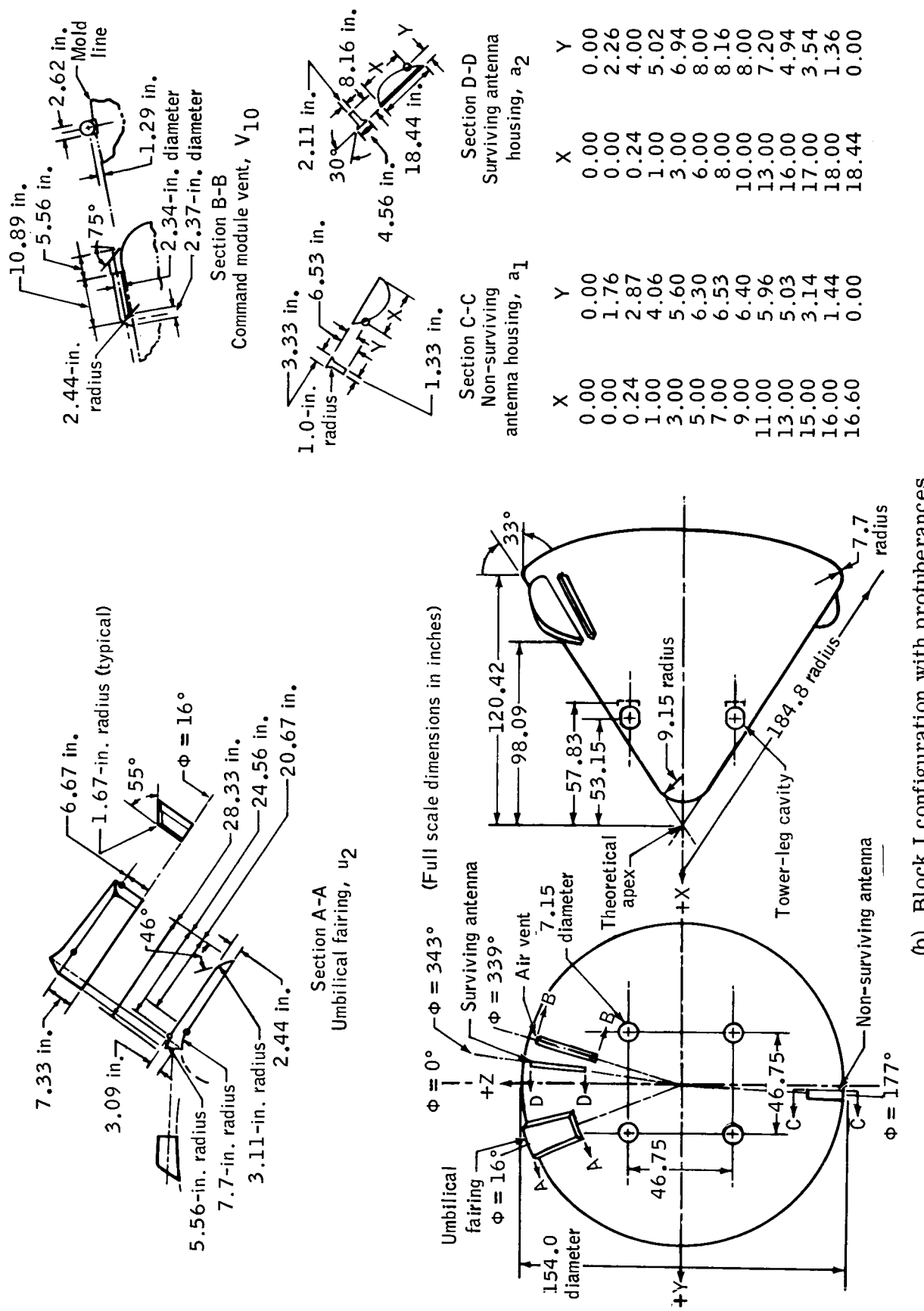


Figure 1. - Sketch showing body system of axes.



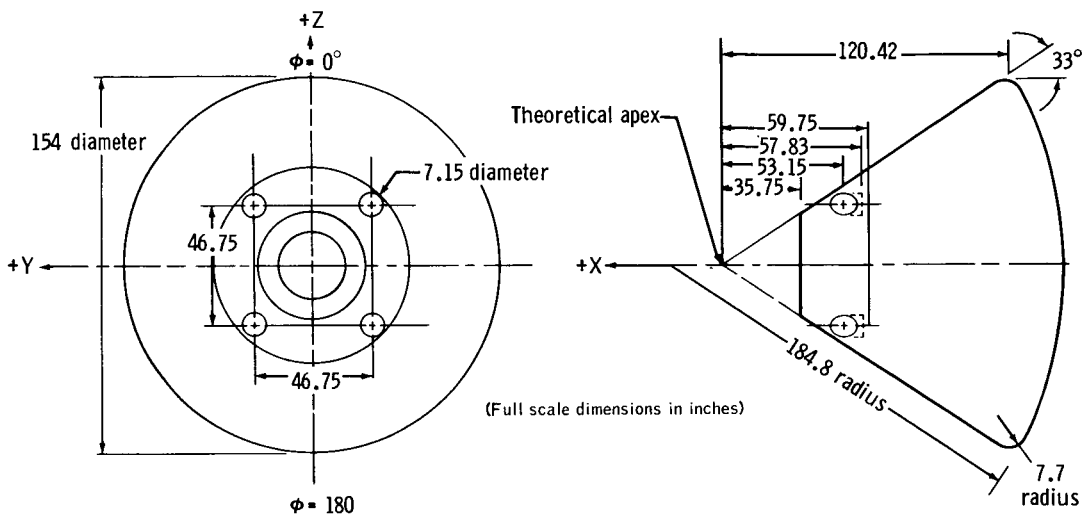
(a) Block I configuration without protuberances.

Figure 2. - Sketch of Apollo CM.

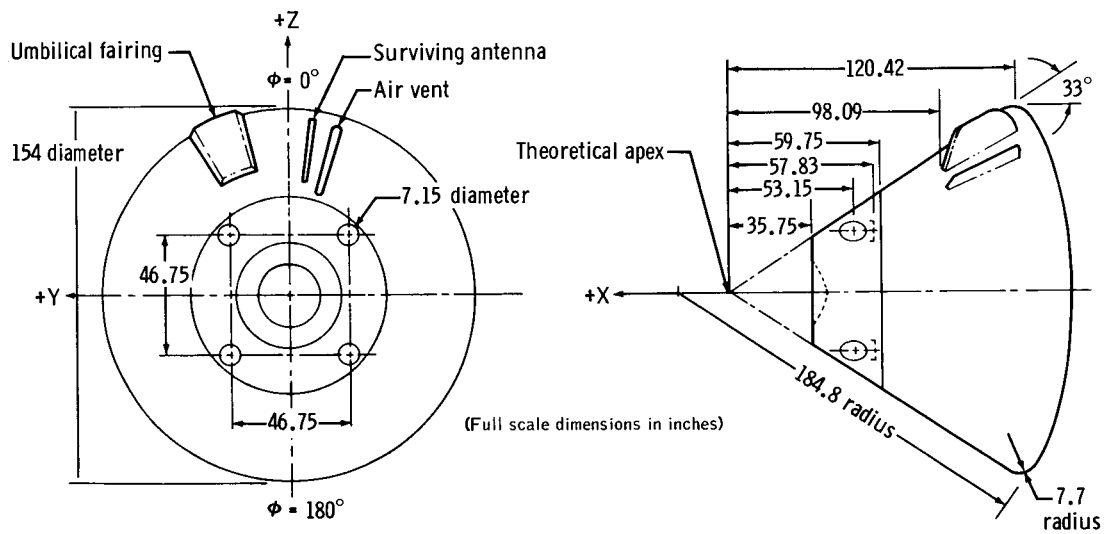


(b) Block I configuration with protuberances.

Figure 2. - Continued.

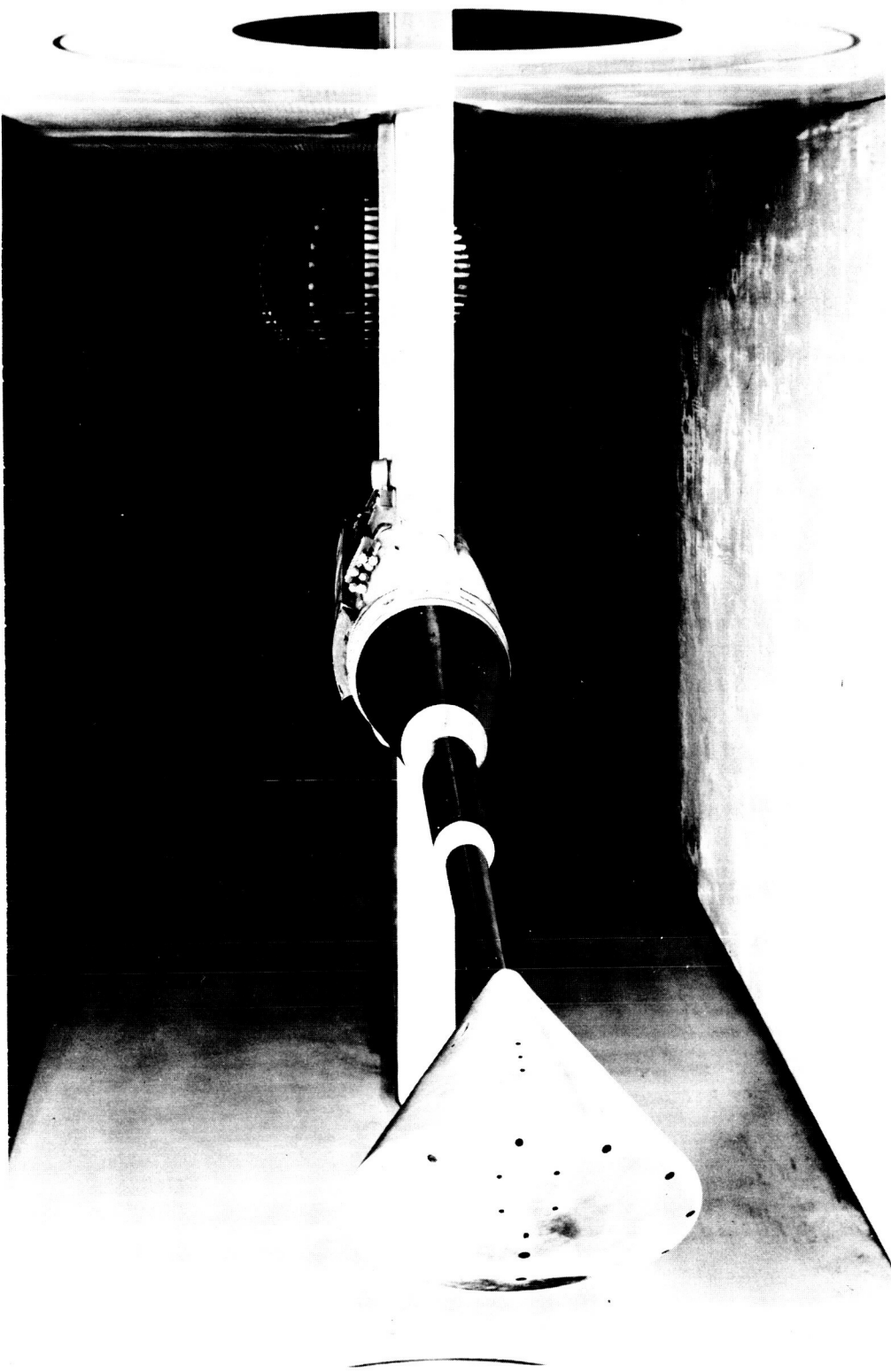


(c) Block II configuration without protuberances.



(d) Block II configuration with protuberances.

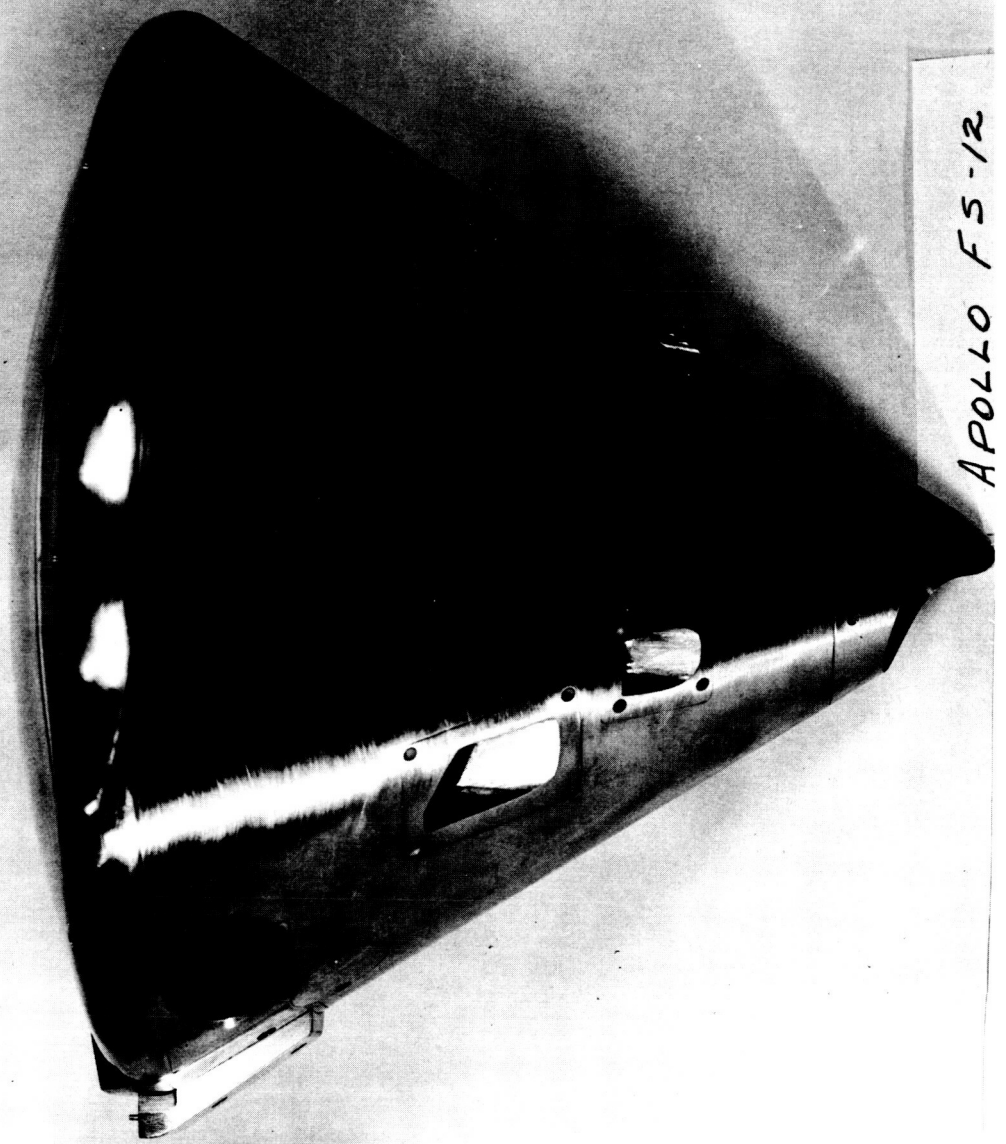
Figure 2. - Concluded.



(a) Photograph of 0.105-scale model of the clean Apollo CM in the
9- by 7-foot test section of the Ames UPWT.

Figure 3. - Typical photographs of Apollo CM test models.

APOLLO F5-12



(b) Photograph of 0.90-scale model of the Apollo CM.

Figure 3. - Continued.



(c) Photograph of 0.059-scale model of Apollo CM (with protuberances) mounted on transverse rod in NAA-TWT facility.

Figure 3. - Concluded.

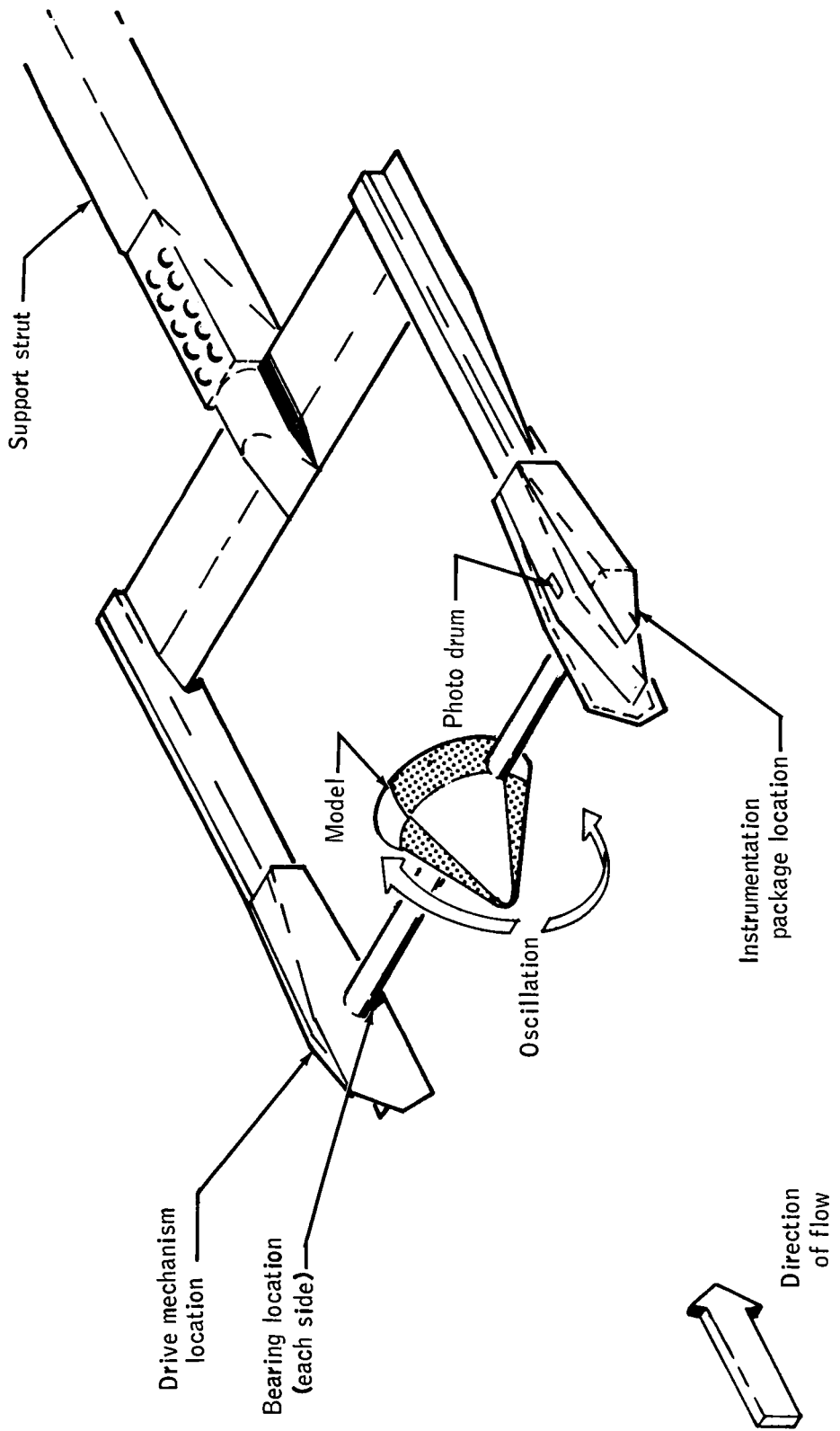
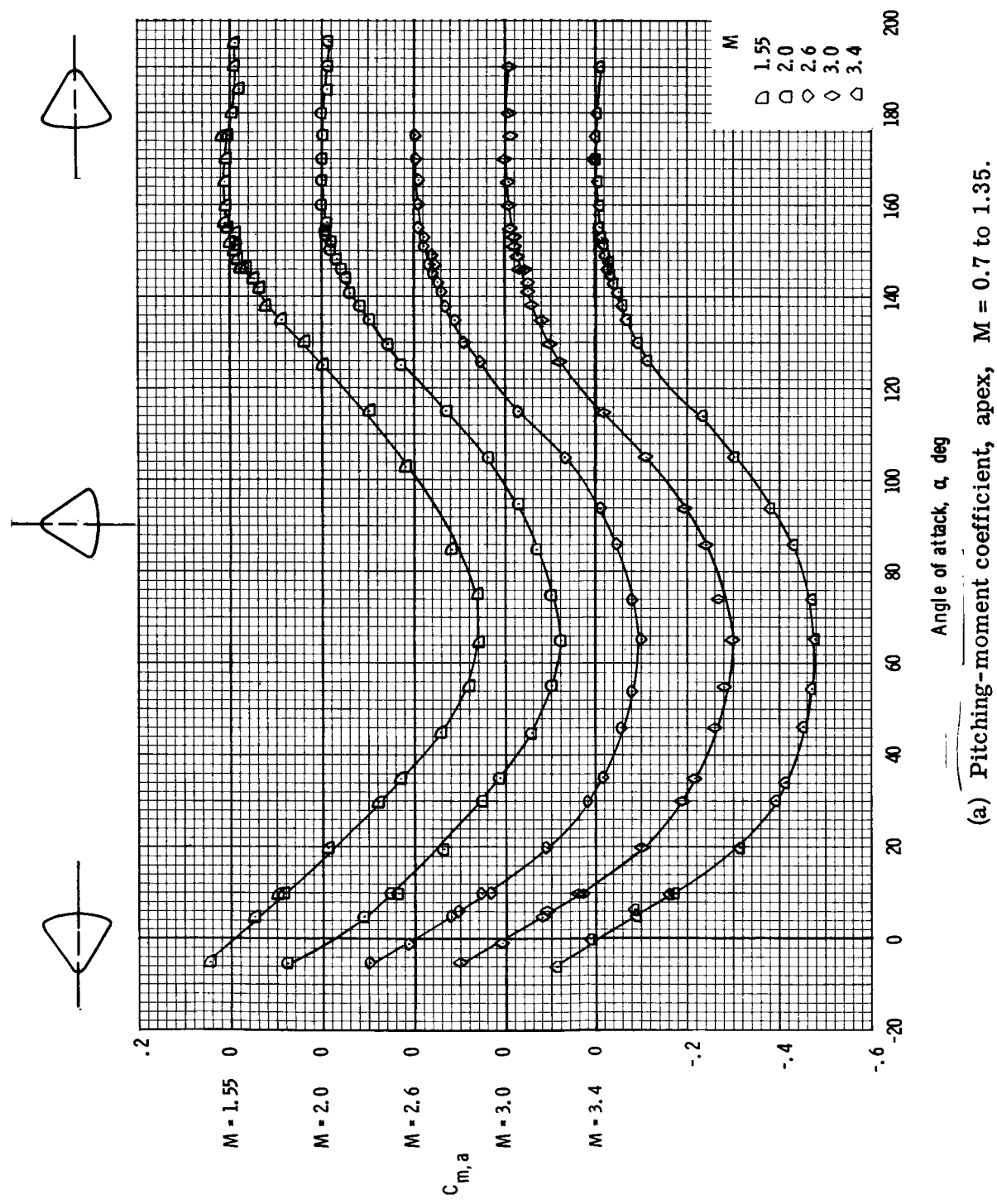
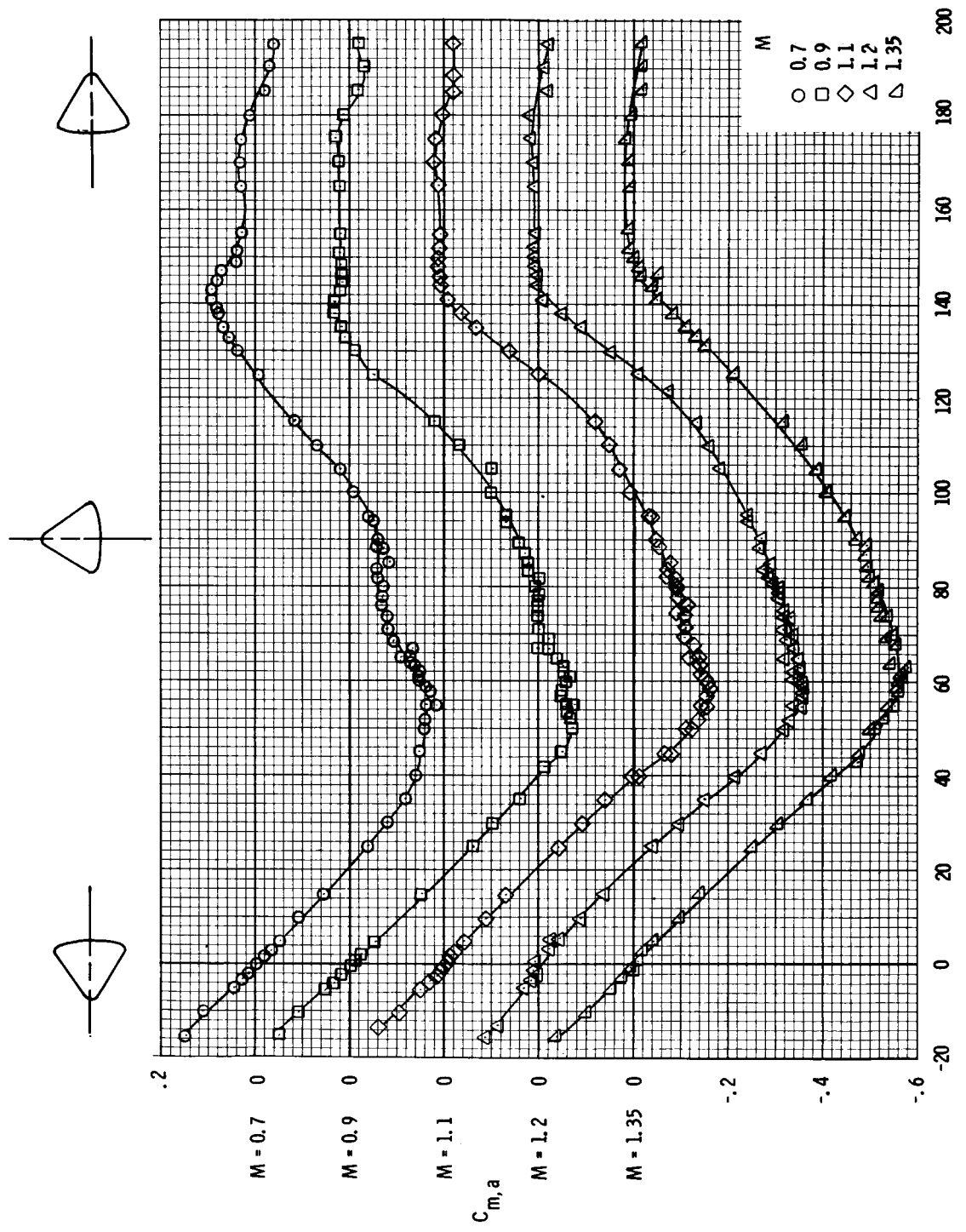


Figure 4. - Sketch showing model installation for free-to-tumble dynamic tests.



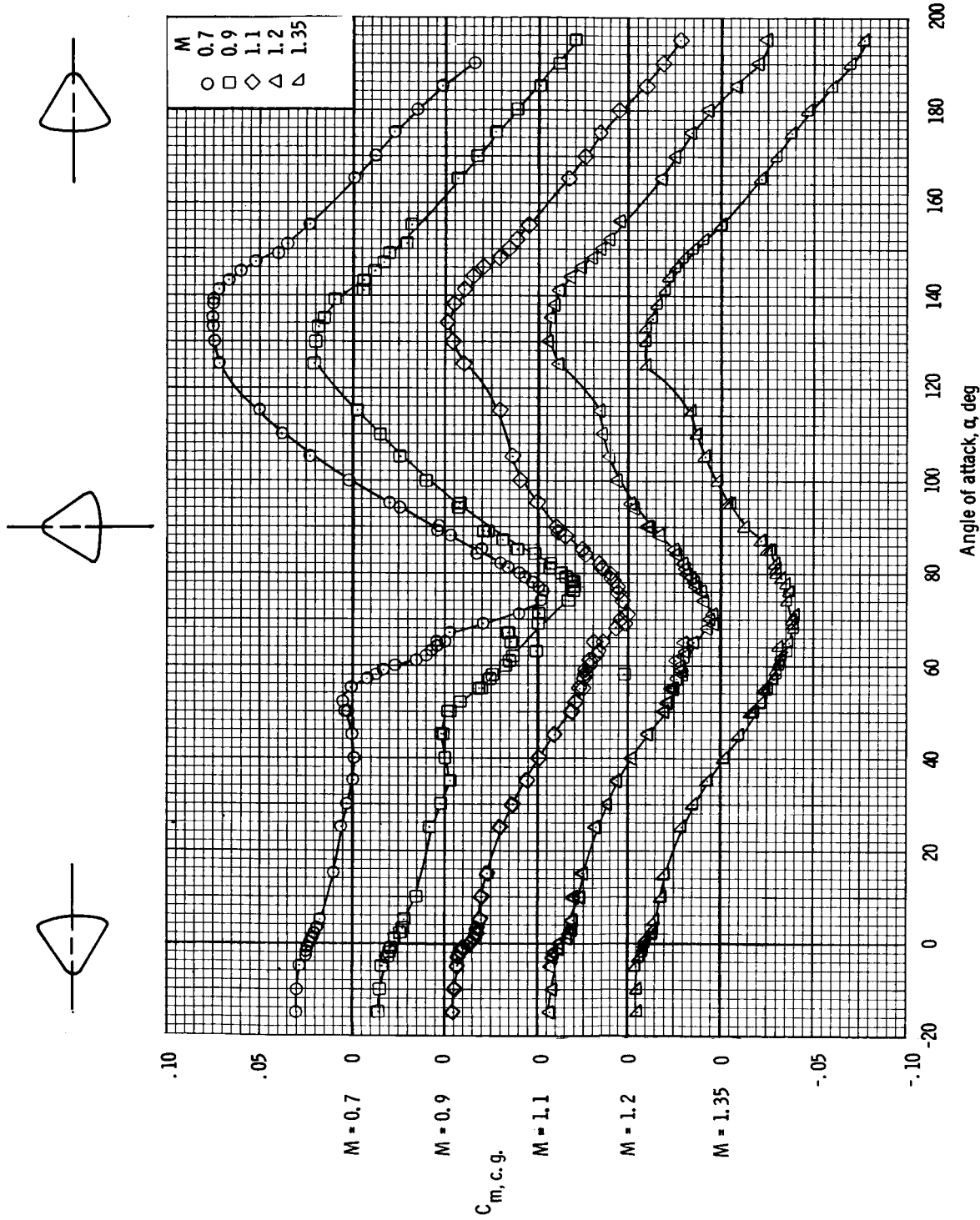
(a) Pitching-moment coefficient, apex, $M = 0.7$ to 1.35 .

Figure 5. - Aerodynamic characteristics of the Apollo CM (without protuberances) obtained at Ames UPWT at $M = 0.7$ to 3.40 .



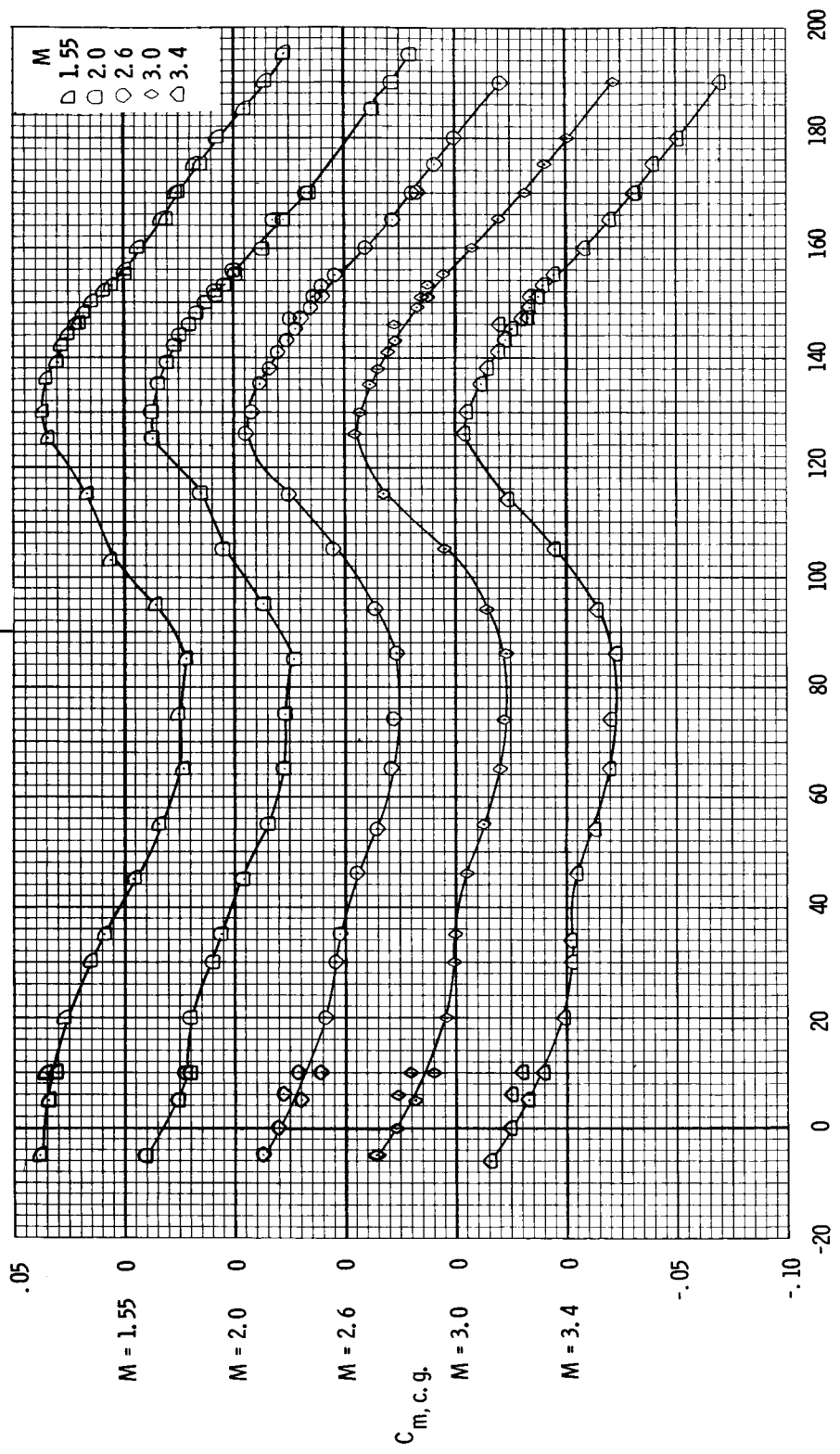
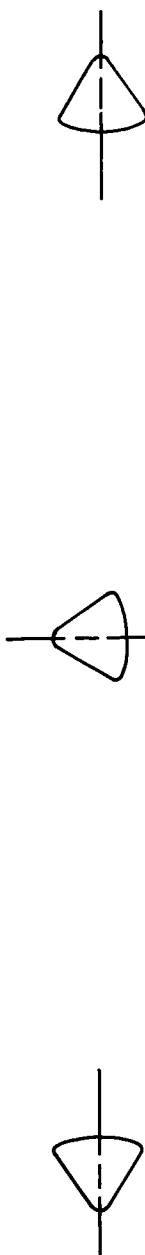
(b) Pitching-moment coefficient, apex, $M = 1.55$ to 3.40 .

Figure 5. - Continued.



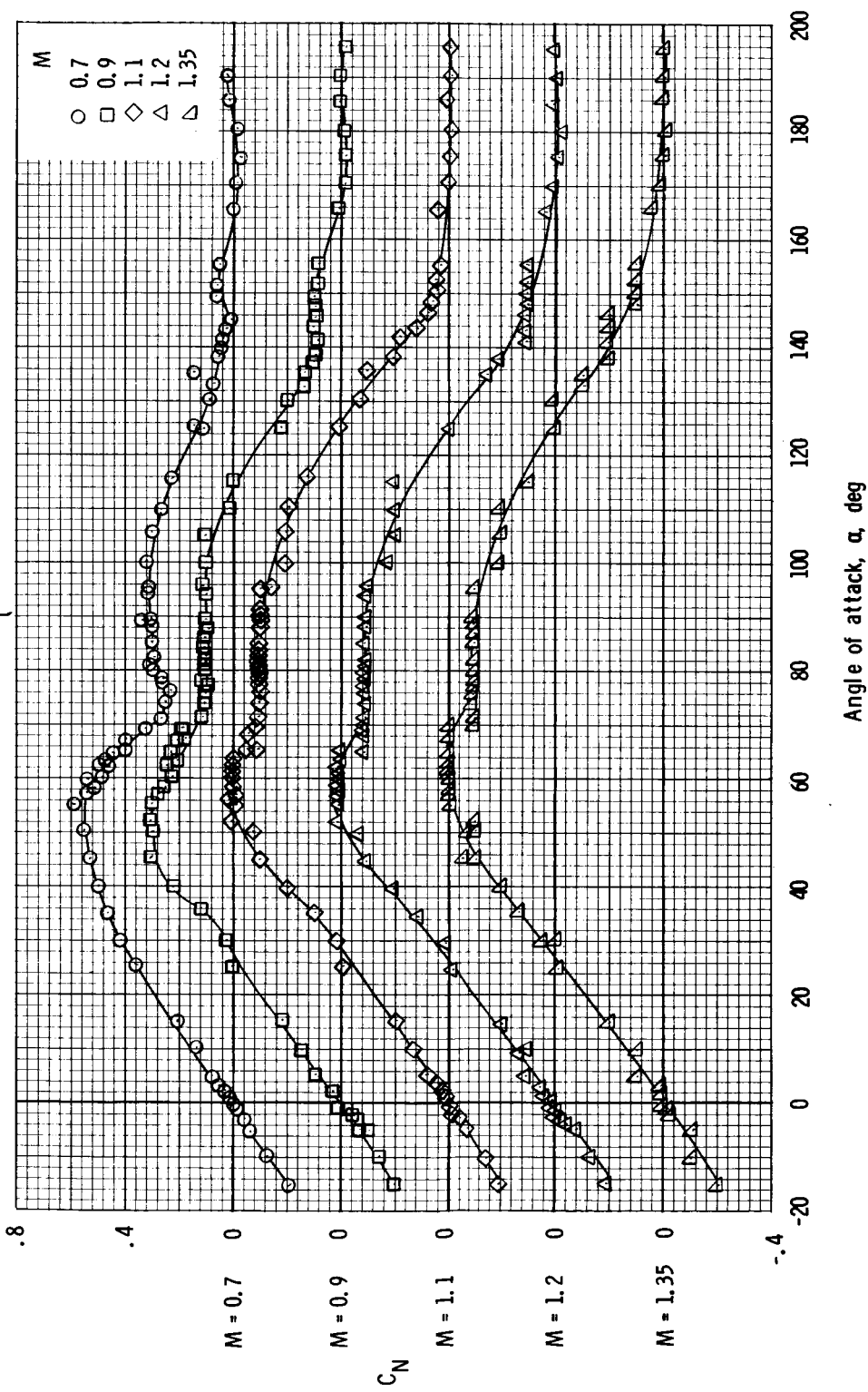
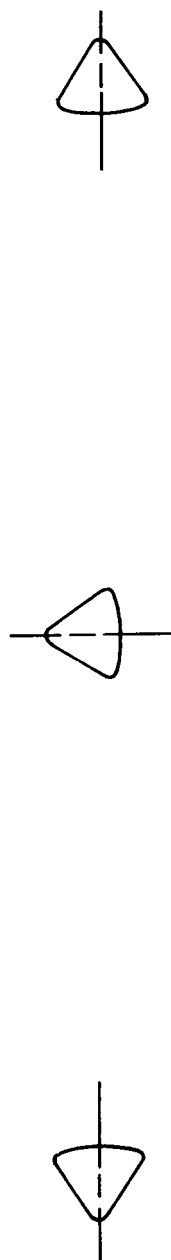
(c) Pitching-moment coefficient, c.g. $\left(\frac{x}{d} = -0.657, \frac{z}{d} = 0.035 \right)$, $M = 0.7$ to 1.35 .

Figure 5. - Continued.



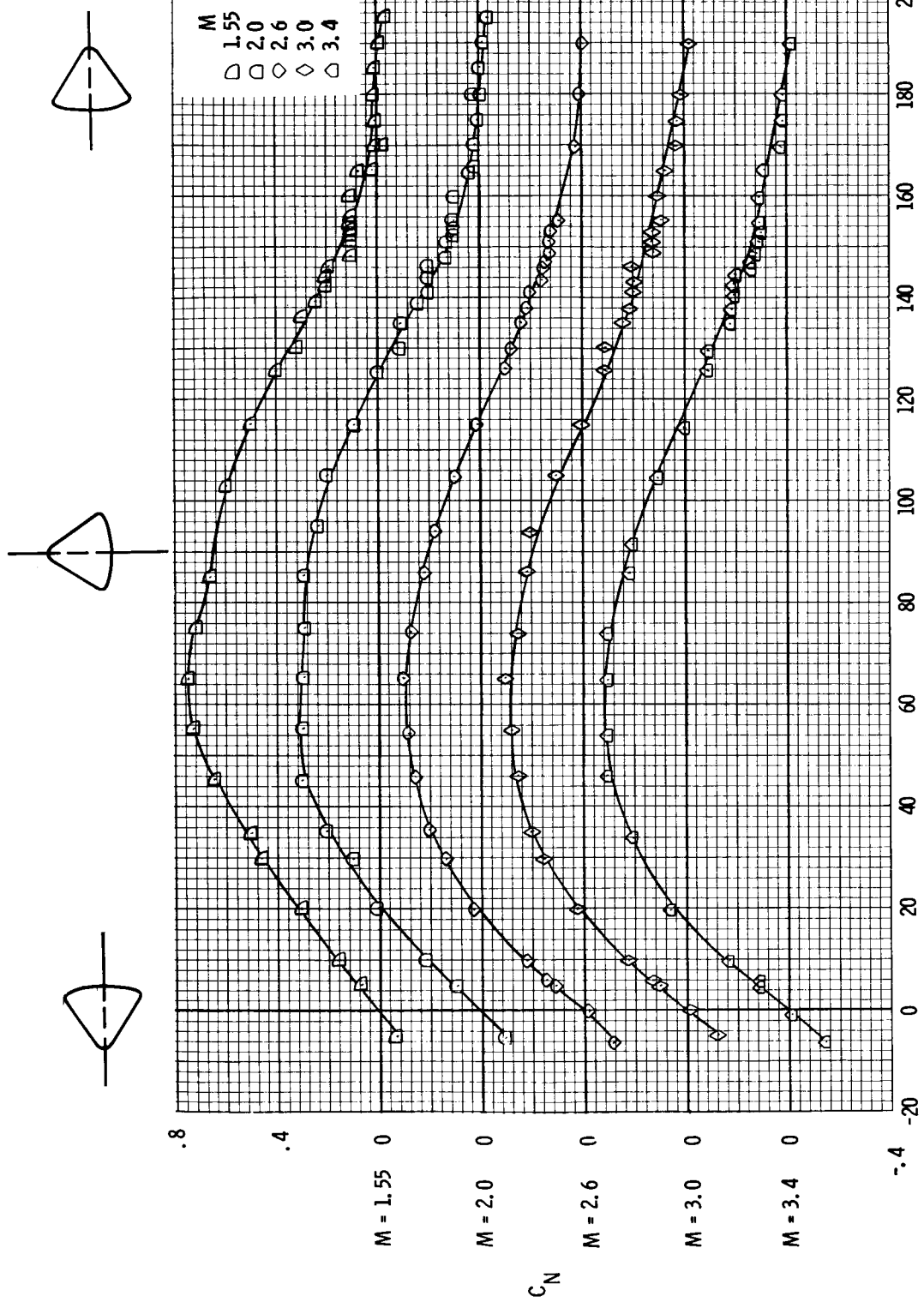
(d) Pitching-moment coefficient, c.g. $\left(\frac{x}{d} = -0.657, \frac{z}{d} = 0.035 \right)$, $M = 1.55$ to 3.40 .

Figure 5. - Continued.



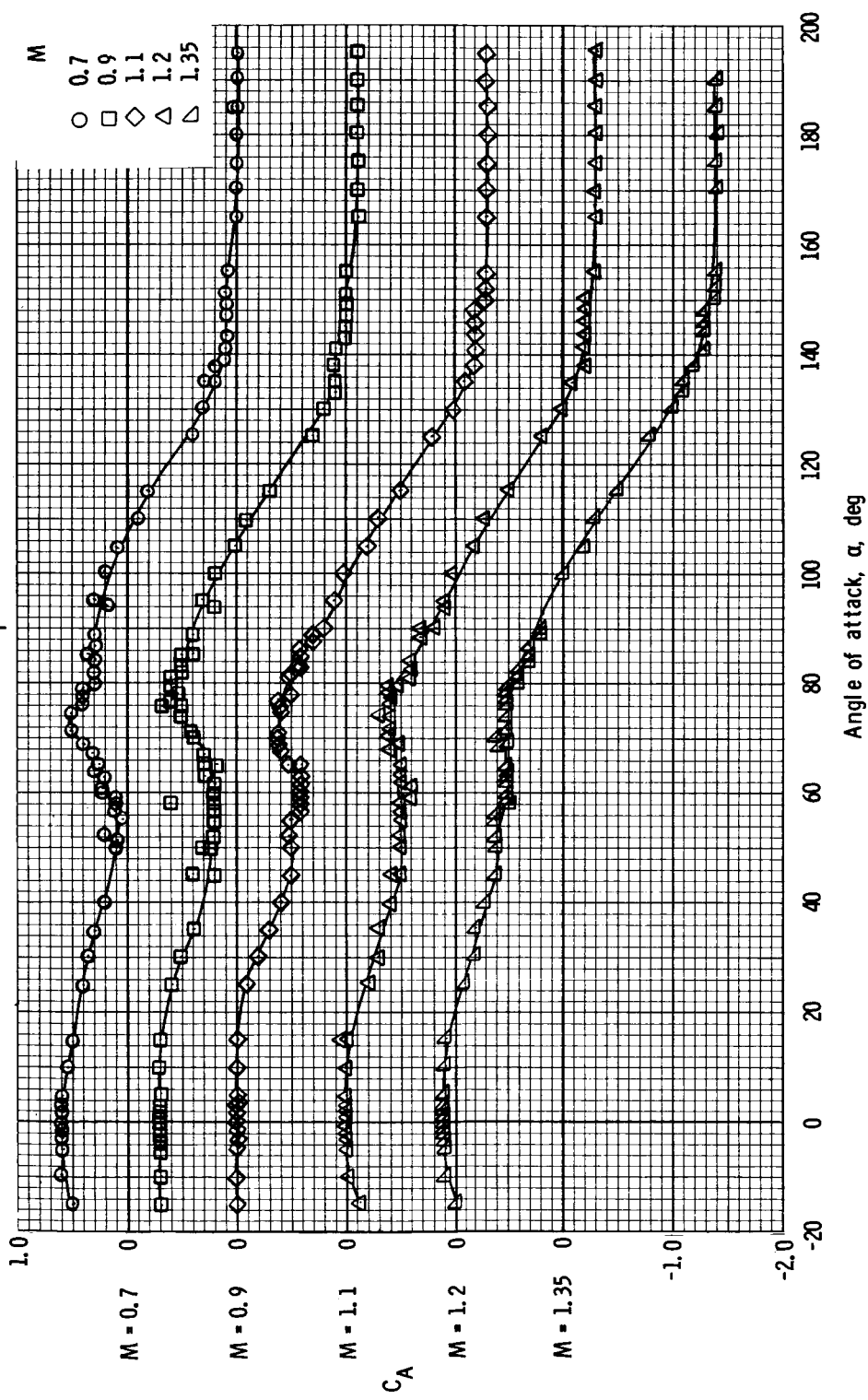
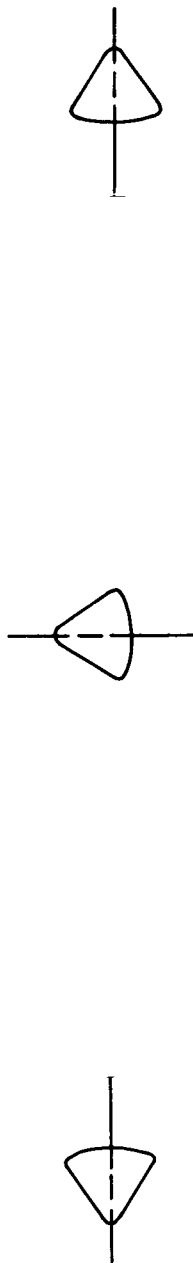
(e) Normal-force coefficient, $M = 0.7$ to 1.35.

Figure 5. – Continued.



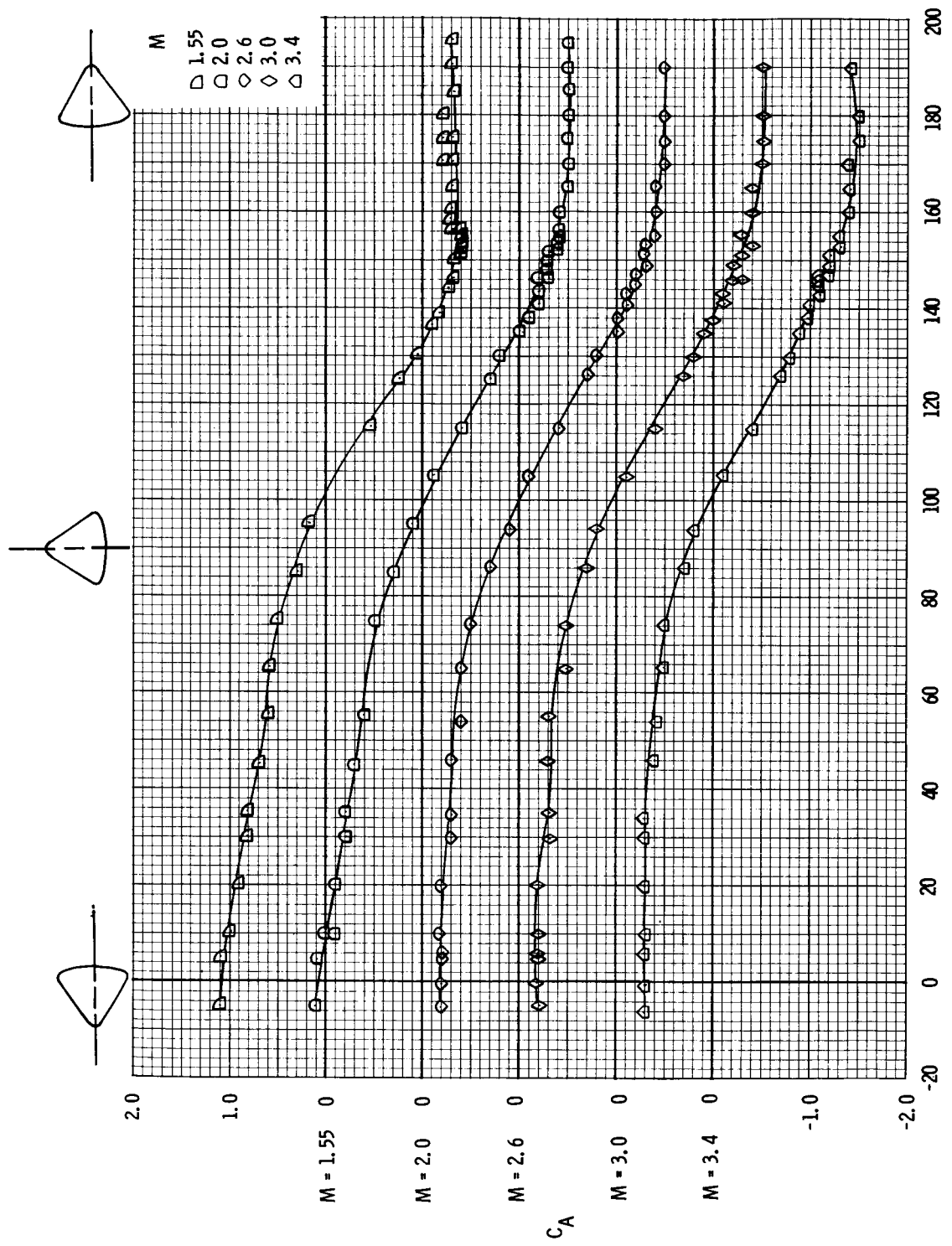
(f) Normal-force coefficient, $M = 1.55$ to 3.40 .

Figure 5. - Continued.



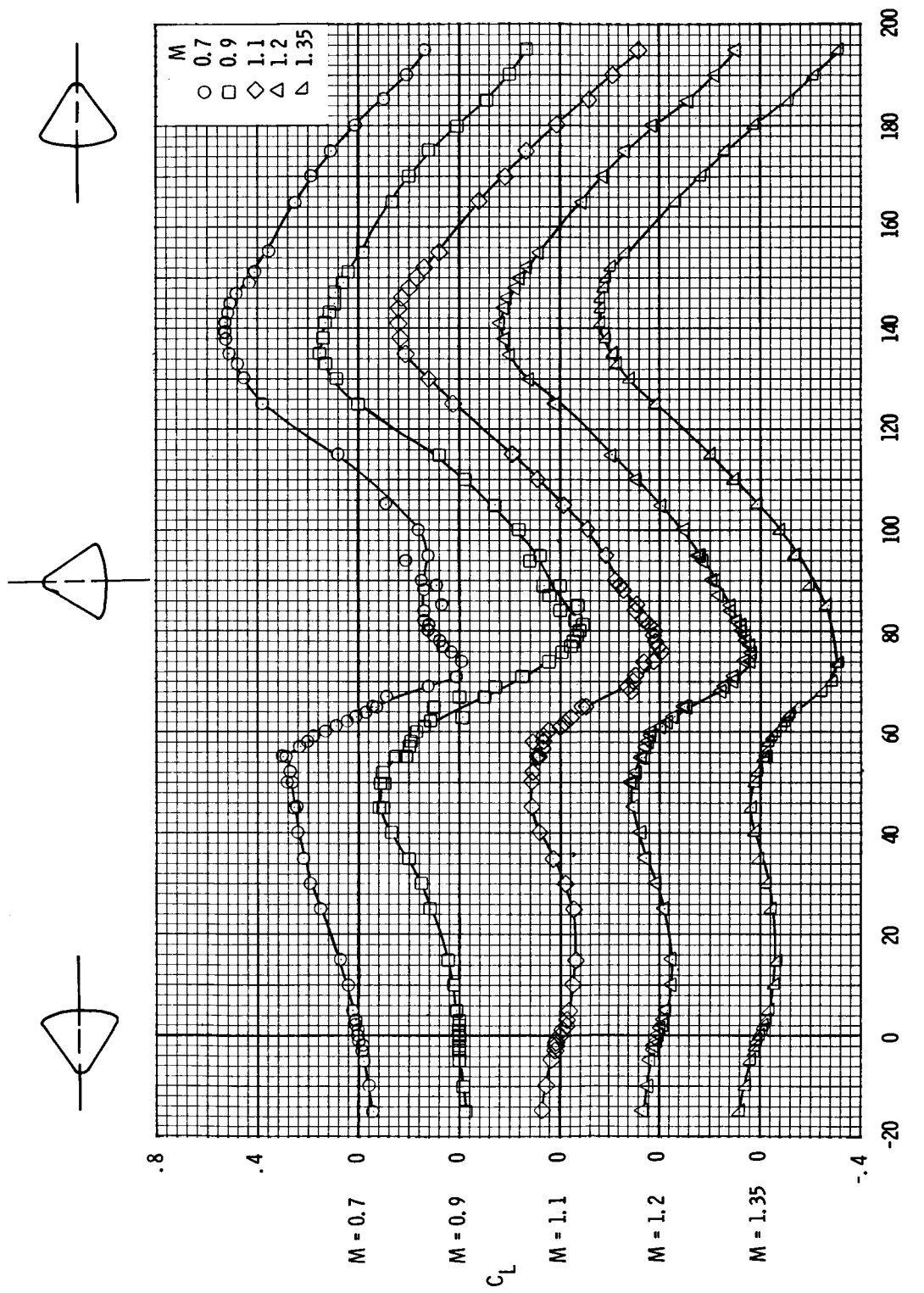
(g) Axial-force coefficient, $M = 0.7$ to 1.35 .

Figure 5. - Continued.



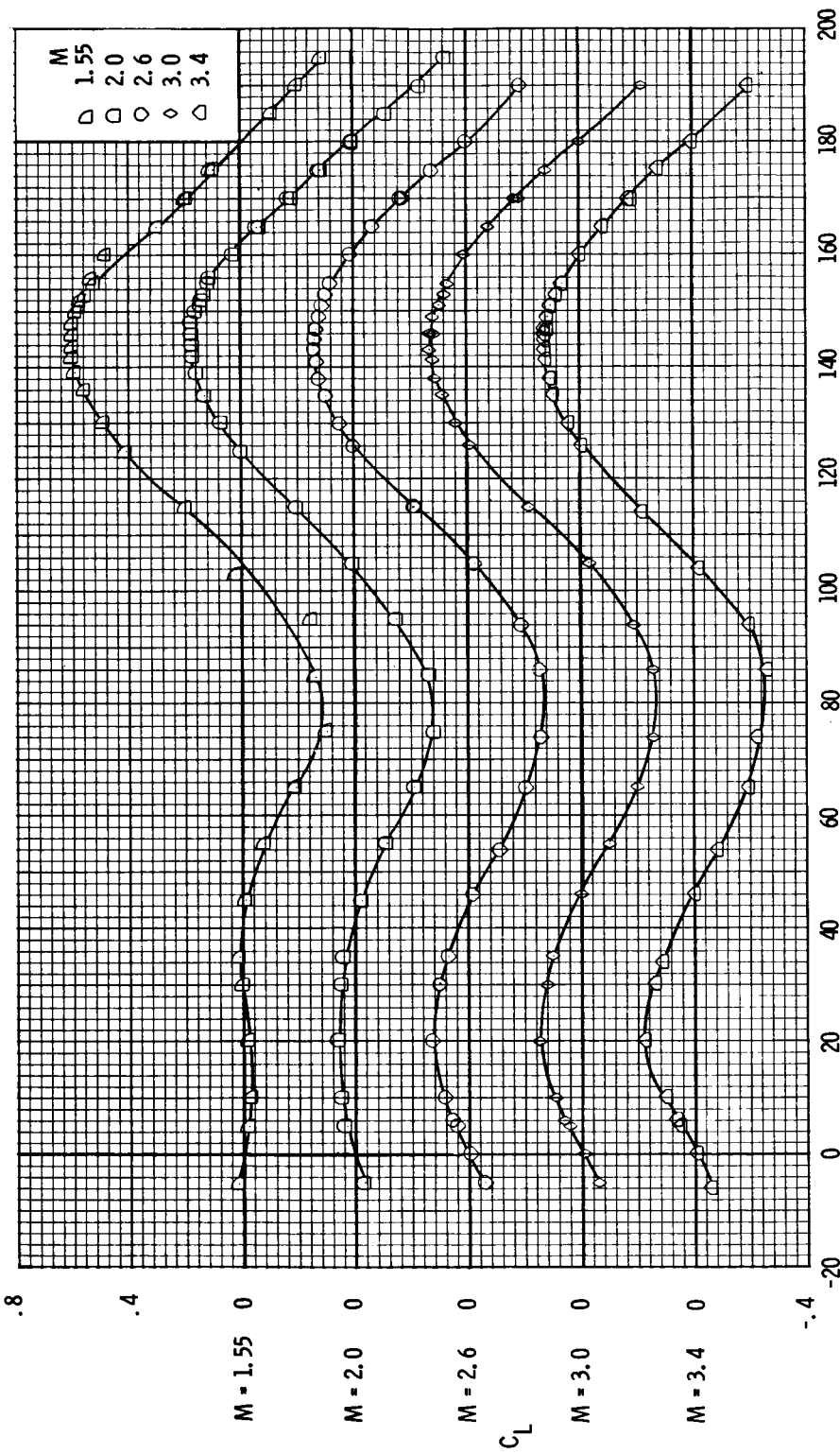
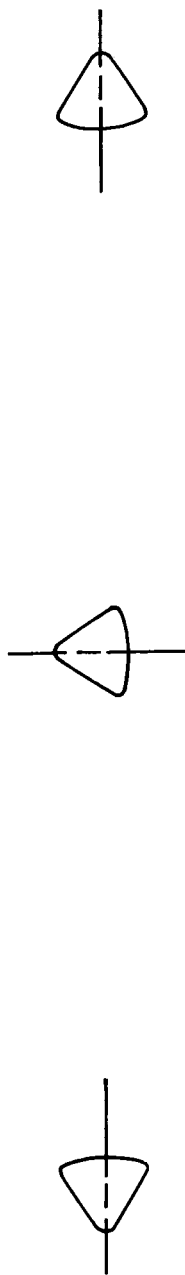
(h) Axial-force coefficient, $M = 1.55$ to 3.40 .

Figure 5. – Continued.



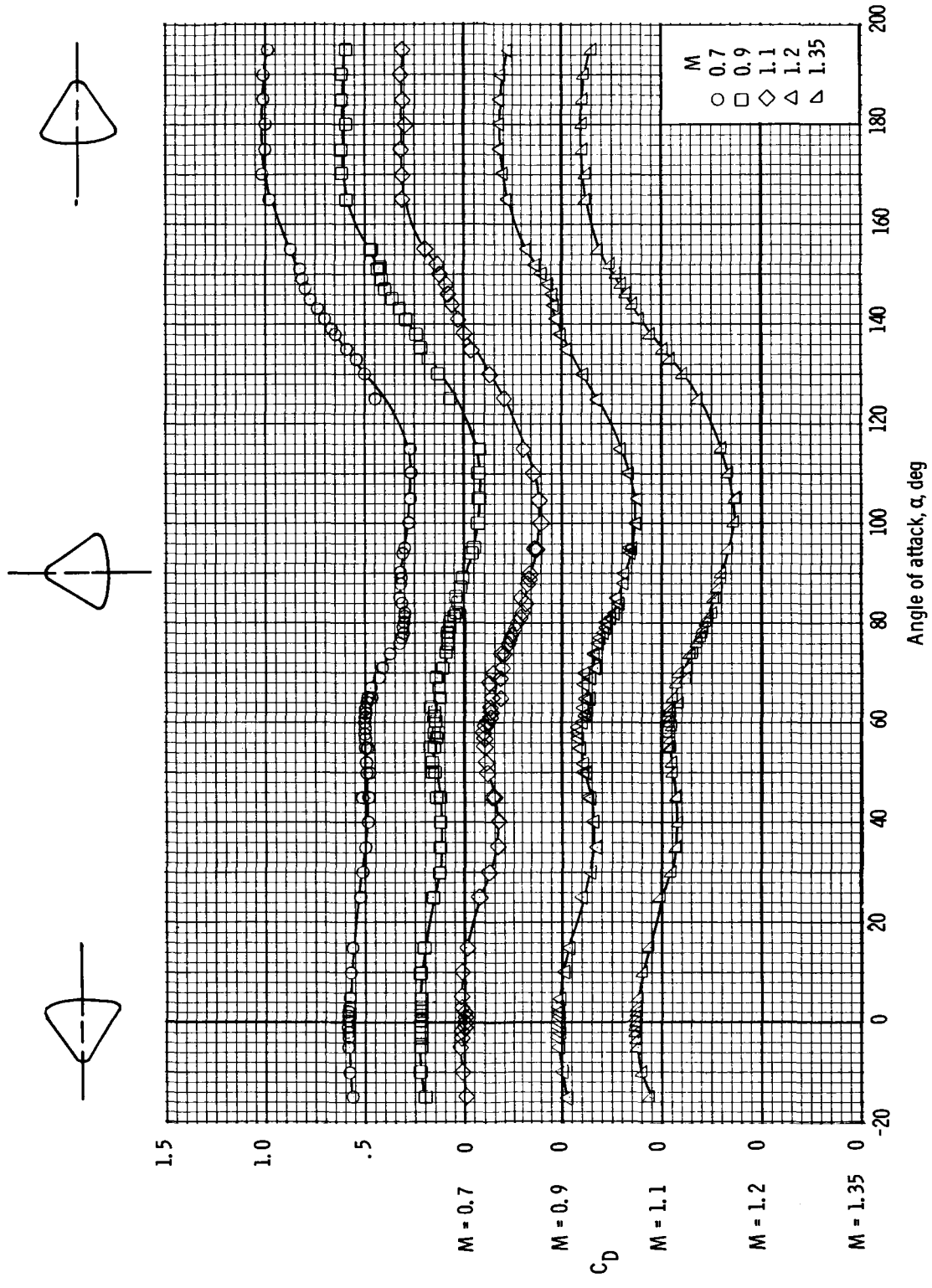
(i) Lift coefficient, $M = 0.7$ to 1.35.

Figure 5. - Continued.



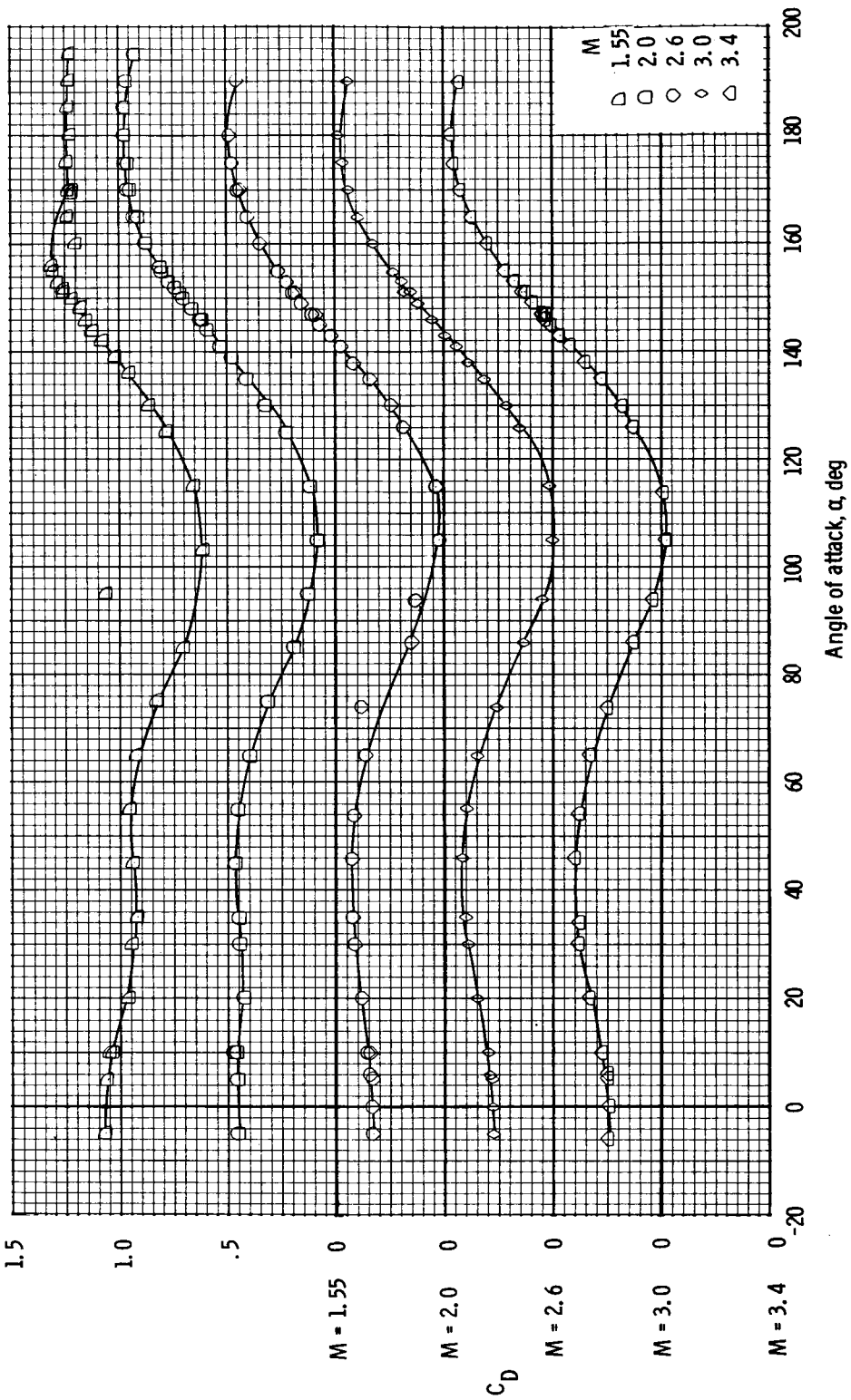
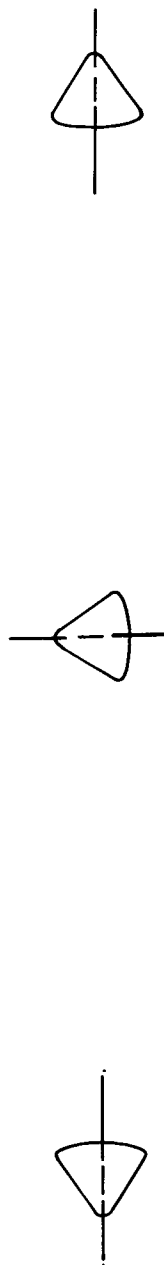
(j) Lift coefficient, $M = 1.55$ to 3.40.

Figure 5.- Continued.



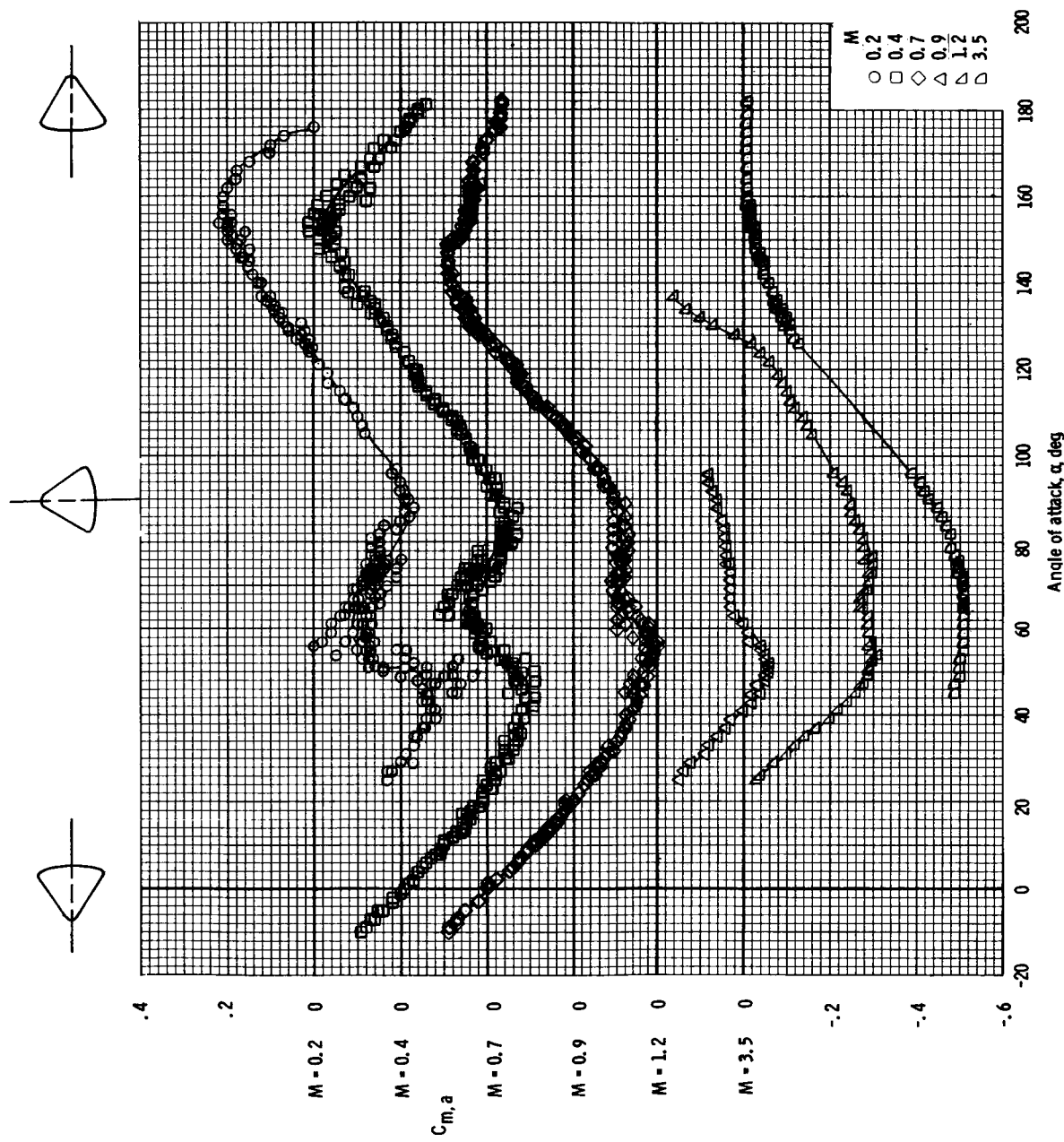
(k) Drag coefficient, $M = 0.7$ to 1.35.

Figure 5. - Continued.



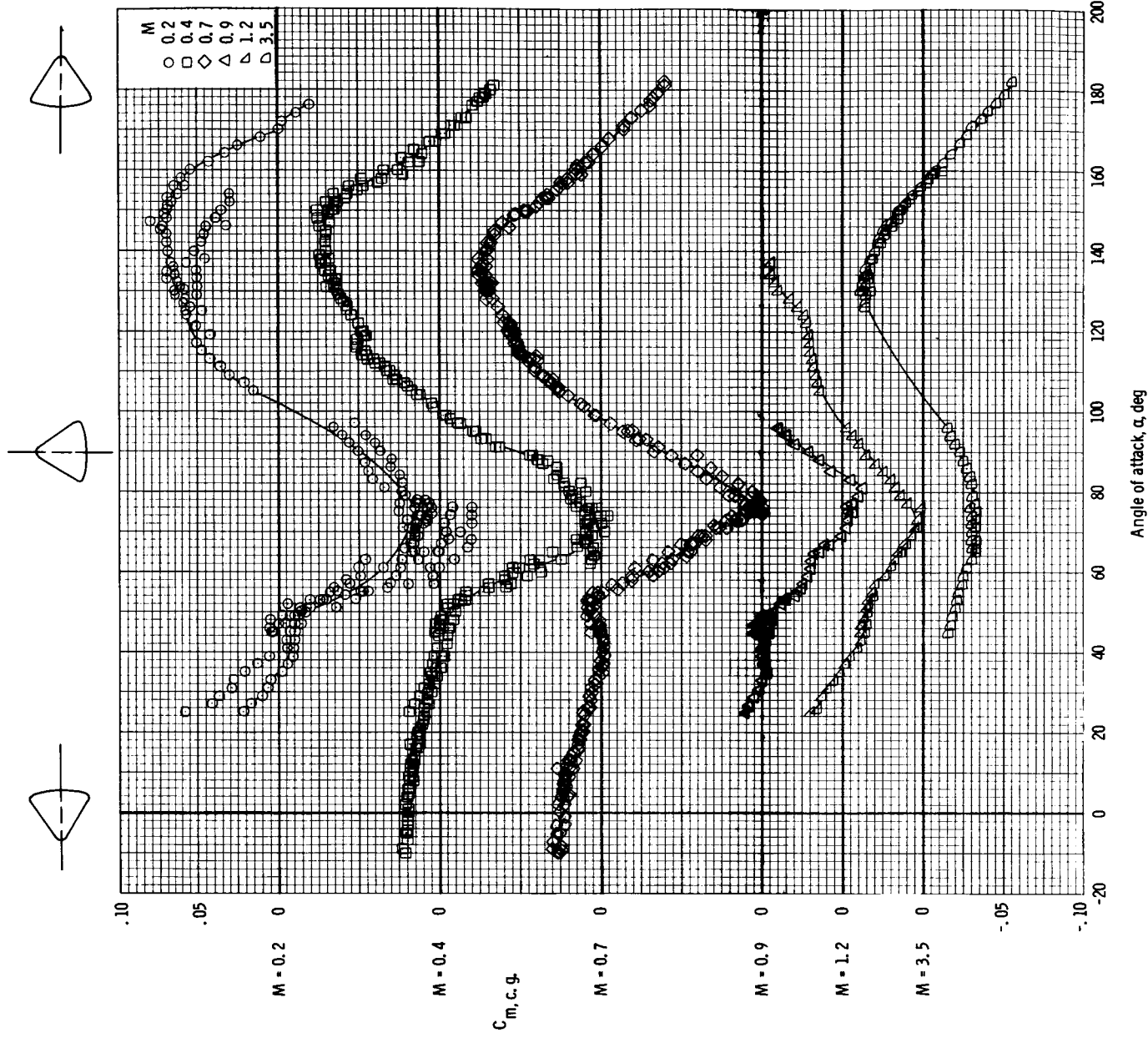
(1) Drag coefficient, $M = 1.55$ to 3.40 .

Figure 5. - Concluded.



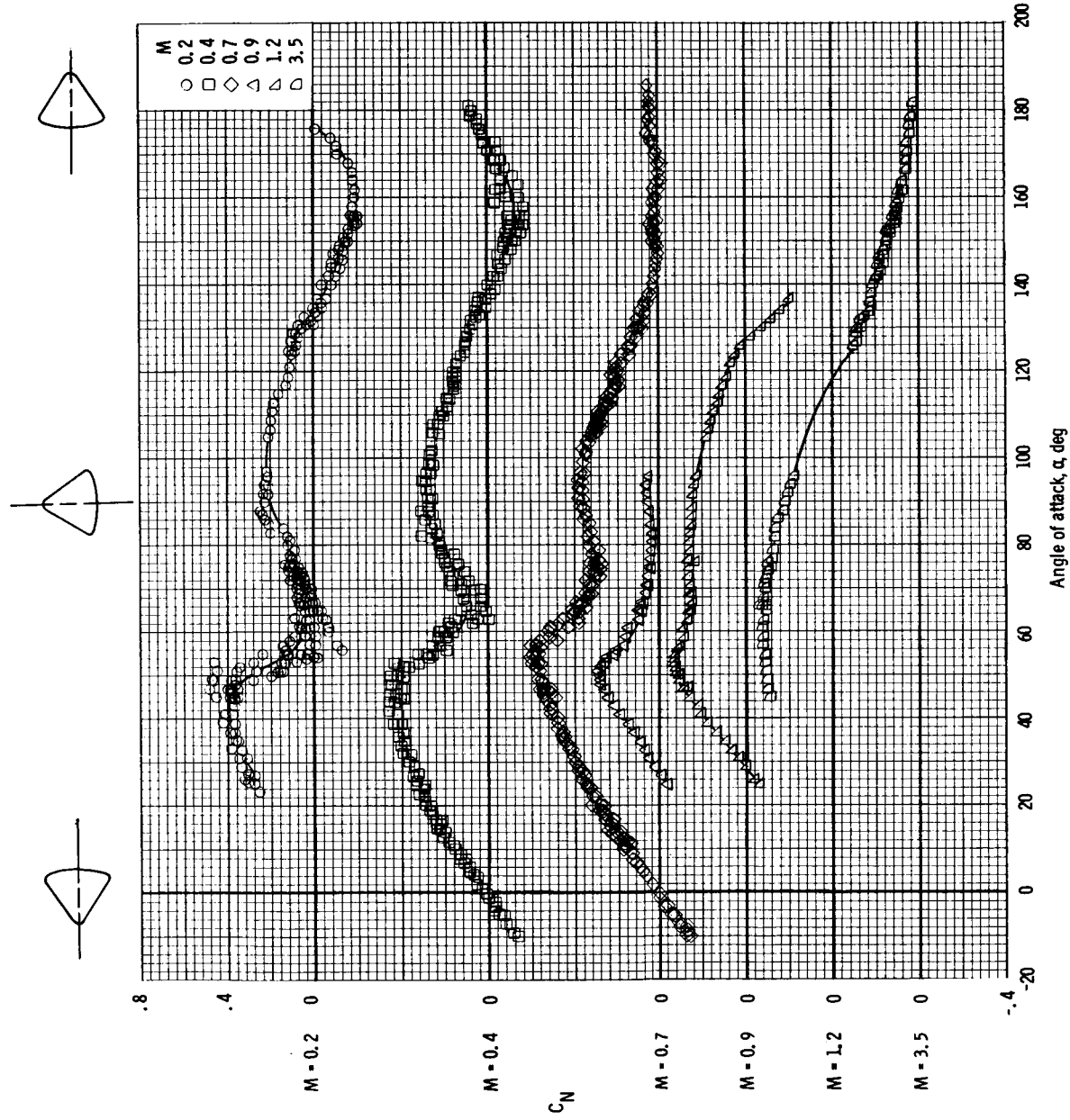
(a) Pitching-moment coefficient, apex.

Figure 6. - Aerodynamic characteristics of the Apollo CM (without protuberances) obtained at NAA-TWT at $M = 0.2$ to 3.5 .



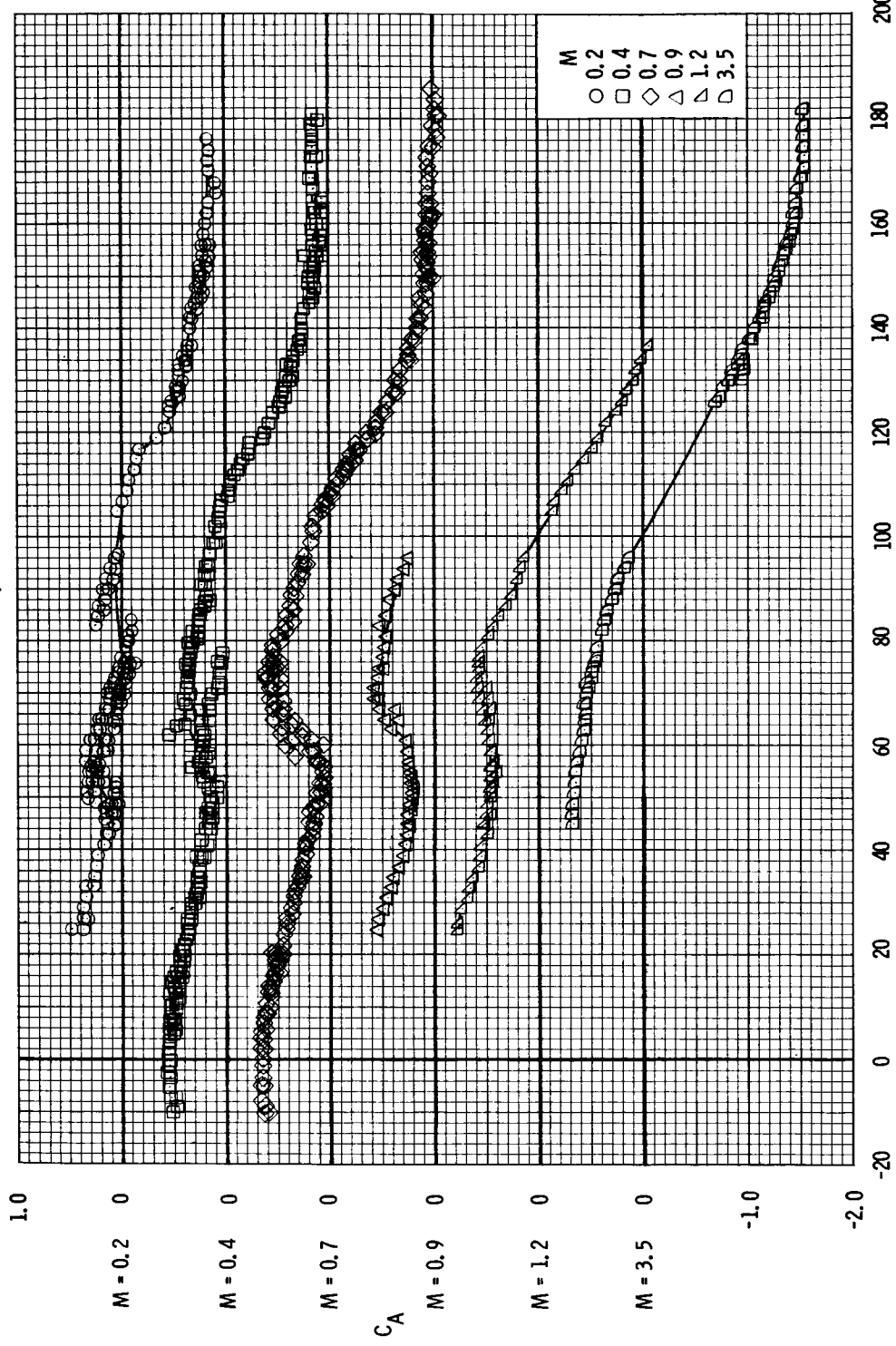
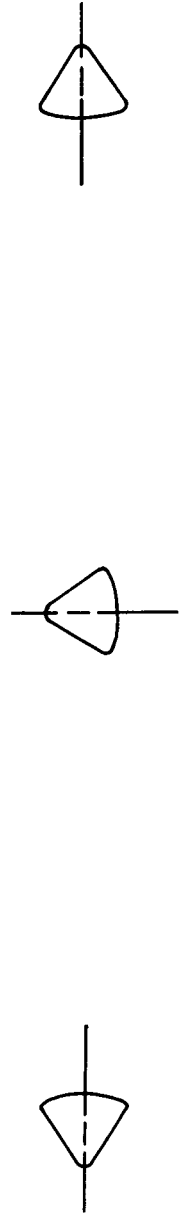
(b) Pitching-moment coefficient, c.g. $\left(\frac{x}{d} = -0.657, \frac{z}{d} = 0.035 \right)$.

Figure 6. - Continued.



(c) Normal-force coefficient.

Figure 6. - Continued.



(d) Axial-force coefficient.
Figure 6. – Continued.

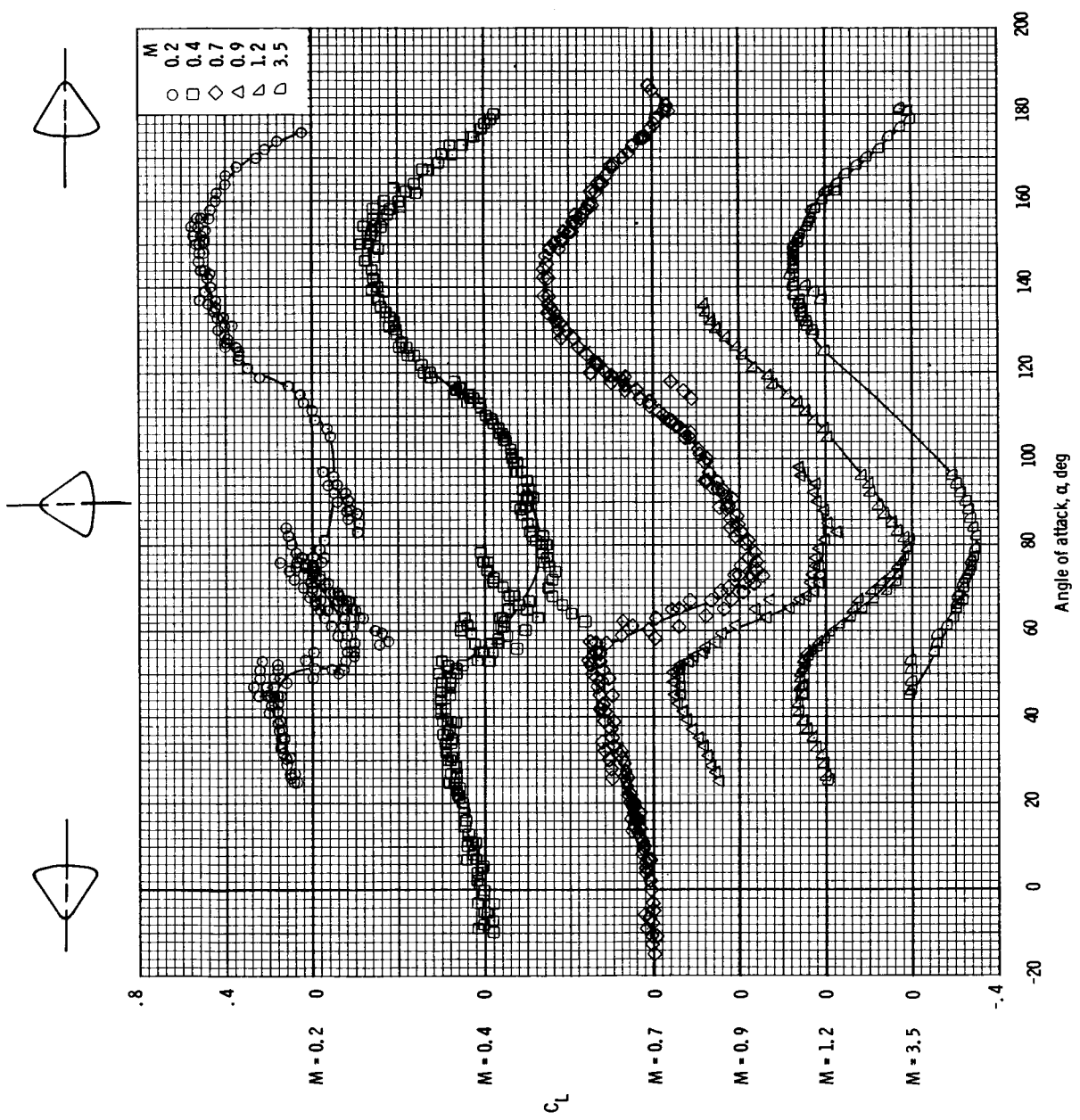
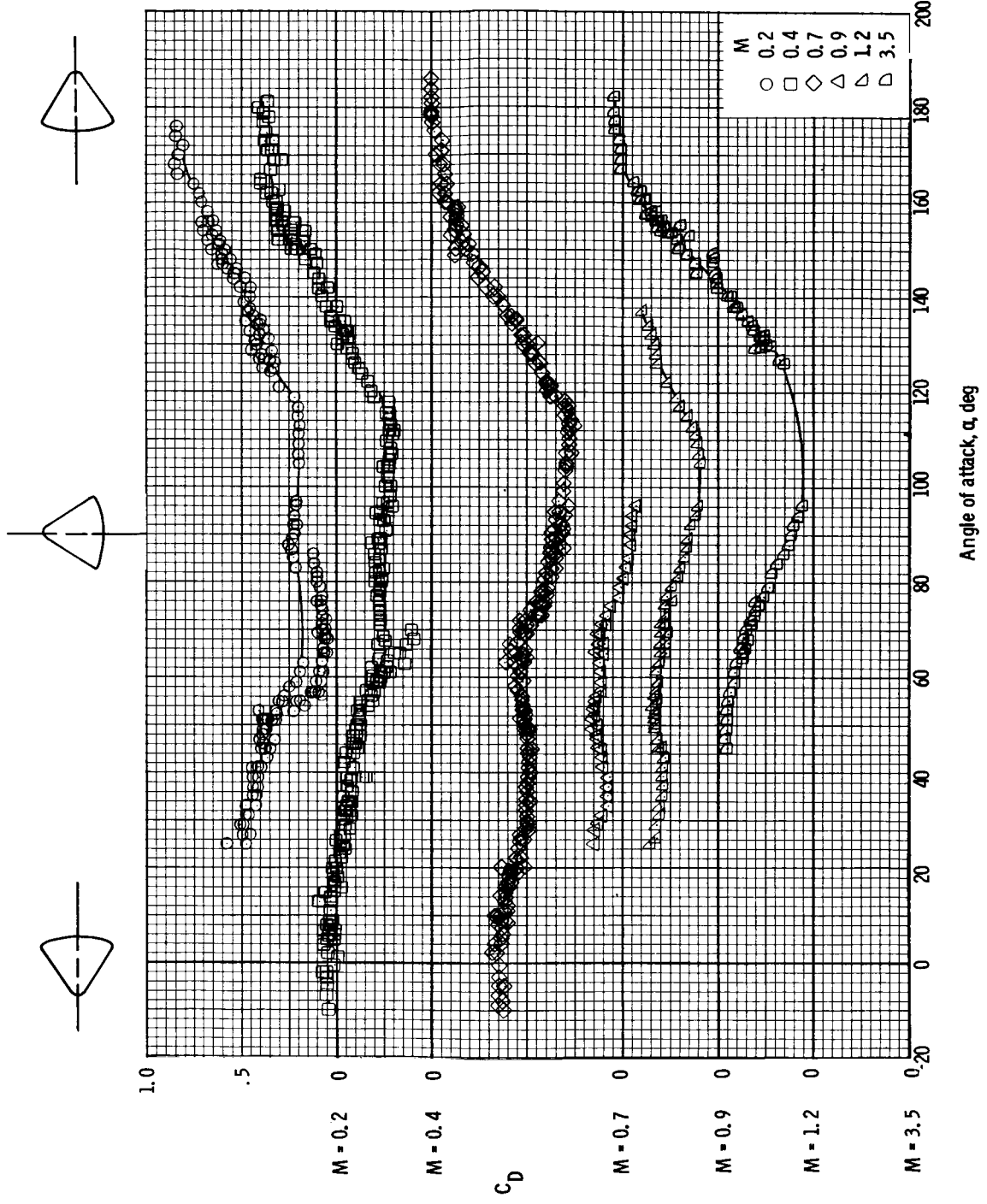
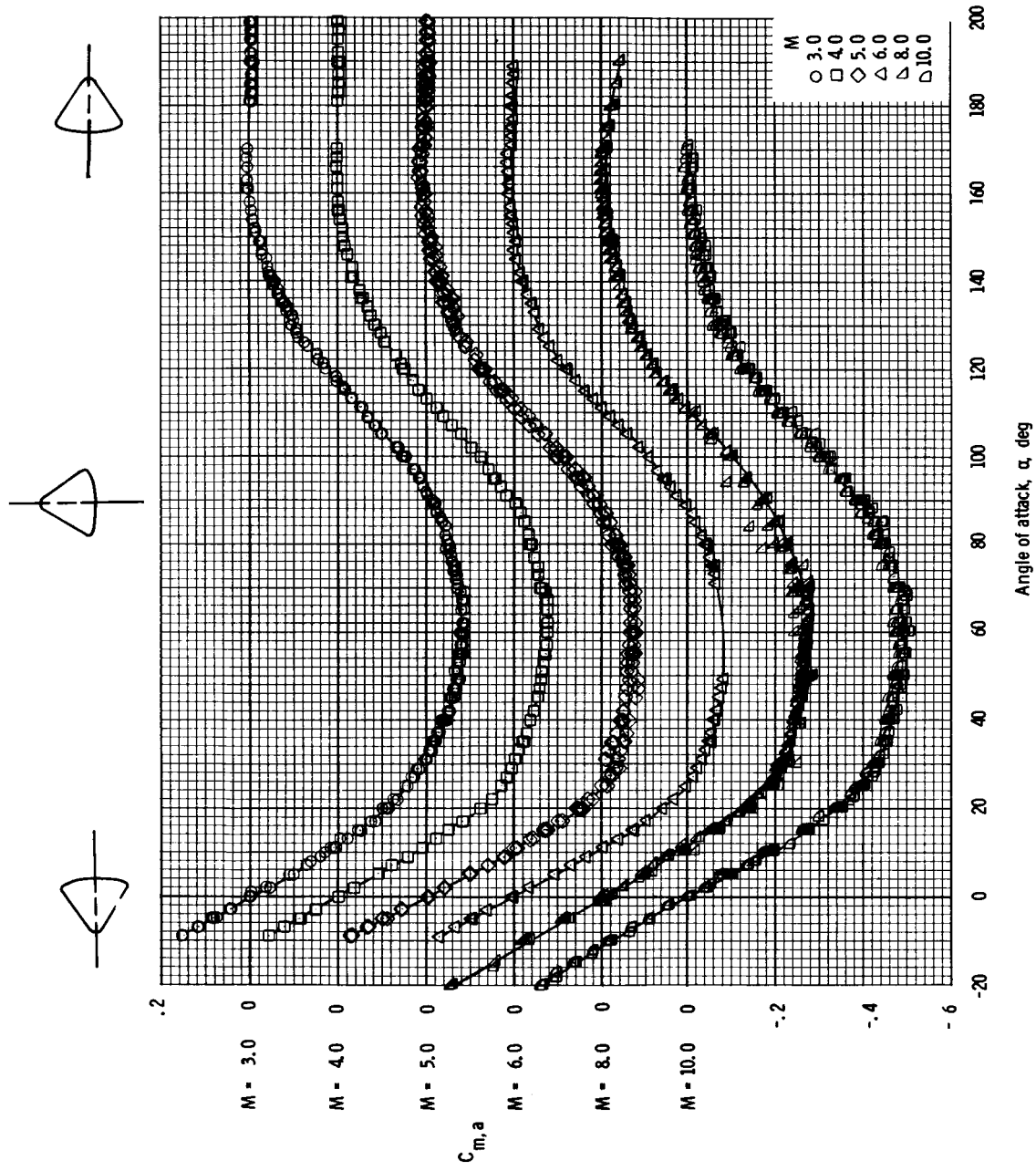


Figure 6. - Continued.
(e) Lift coefficient.



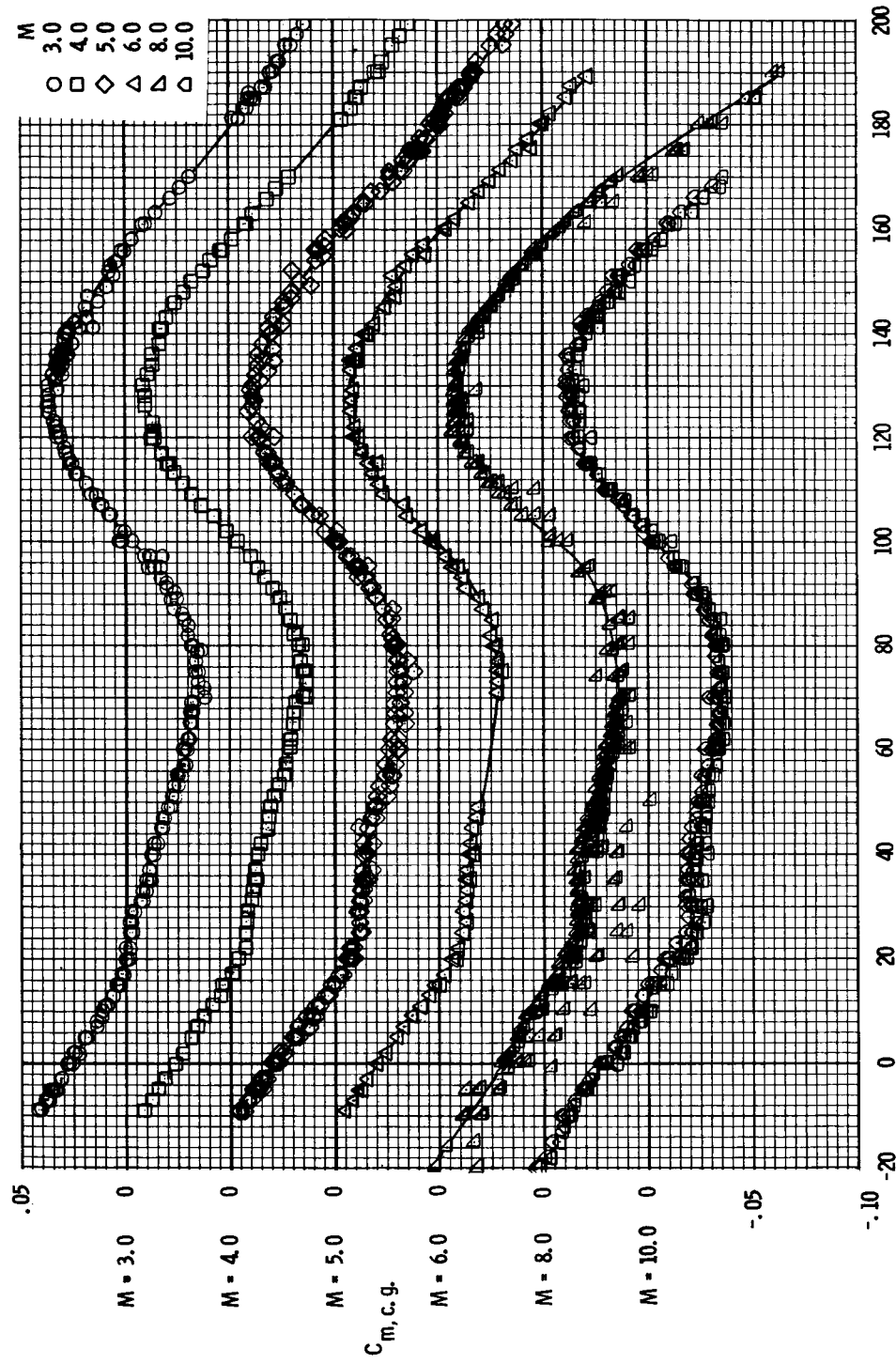
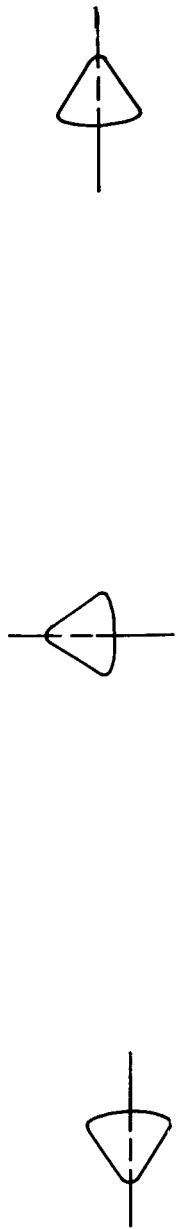
(f) Drag coefficient.

Figure 6. - Concluded.



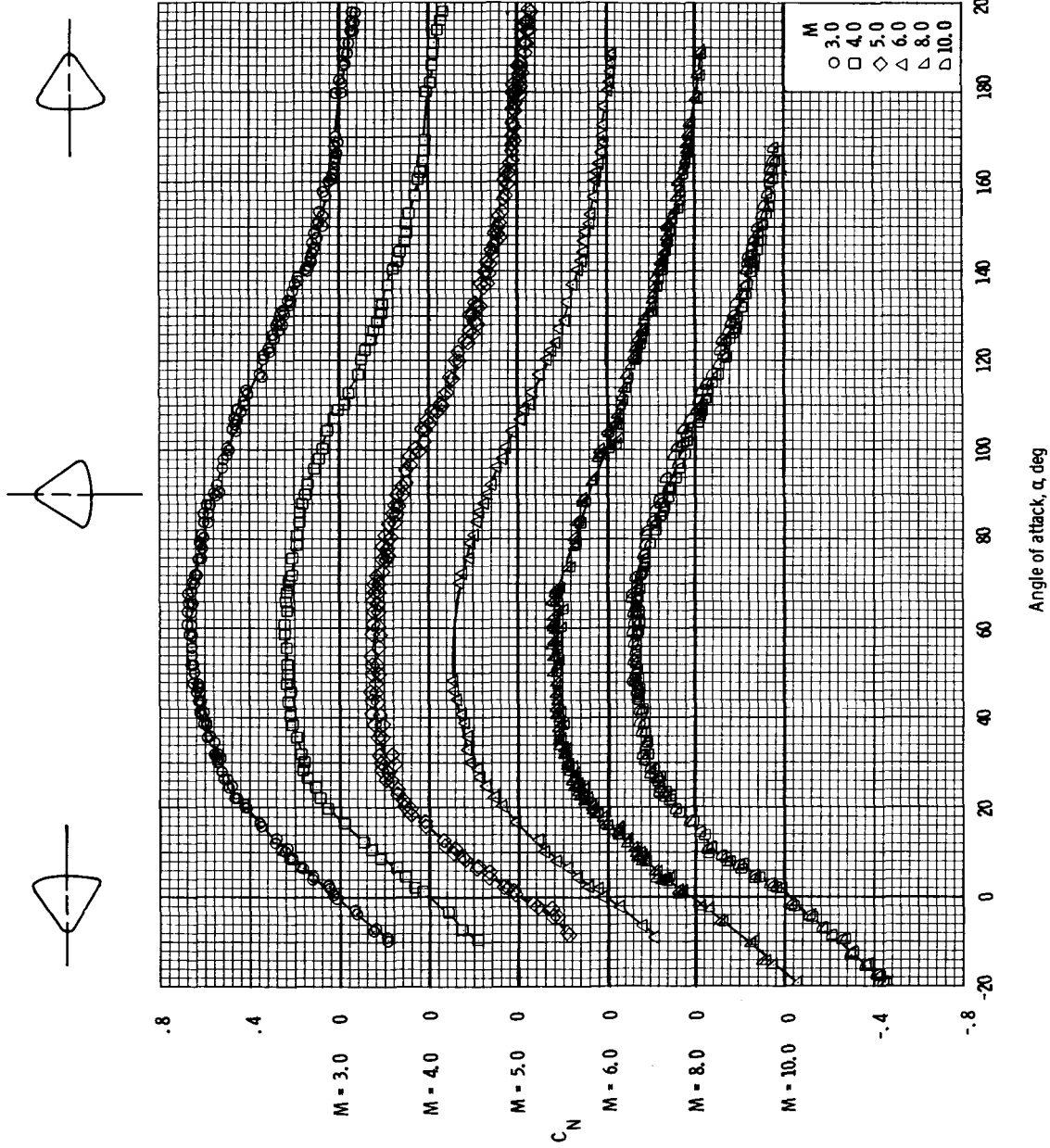
(a) Pitching-moment coefficient, apex.

Figure 7.- Aerodynamic characteristics of the Apollo CM (without protuberances) obtained at AEDC-A, -B, and -C facilities at $M = 3.0$ to 10.0 .



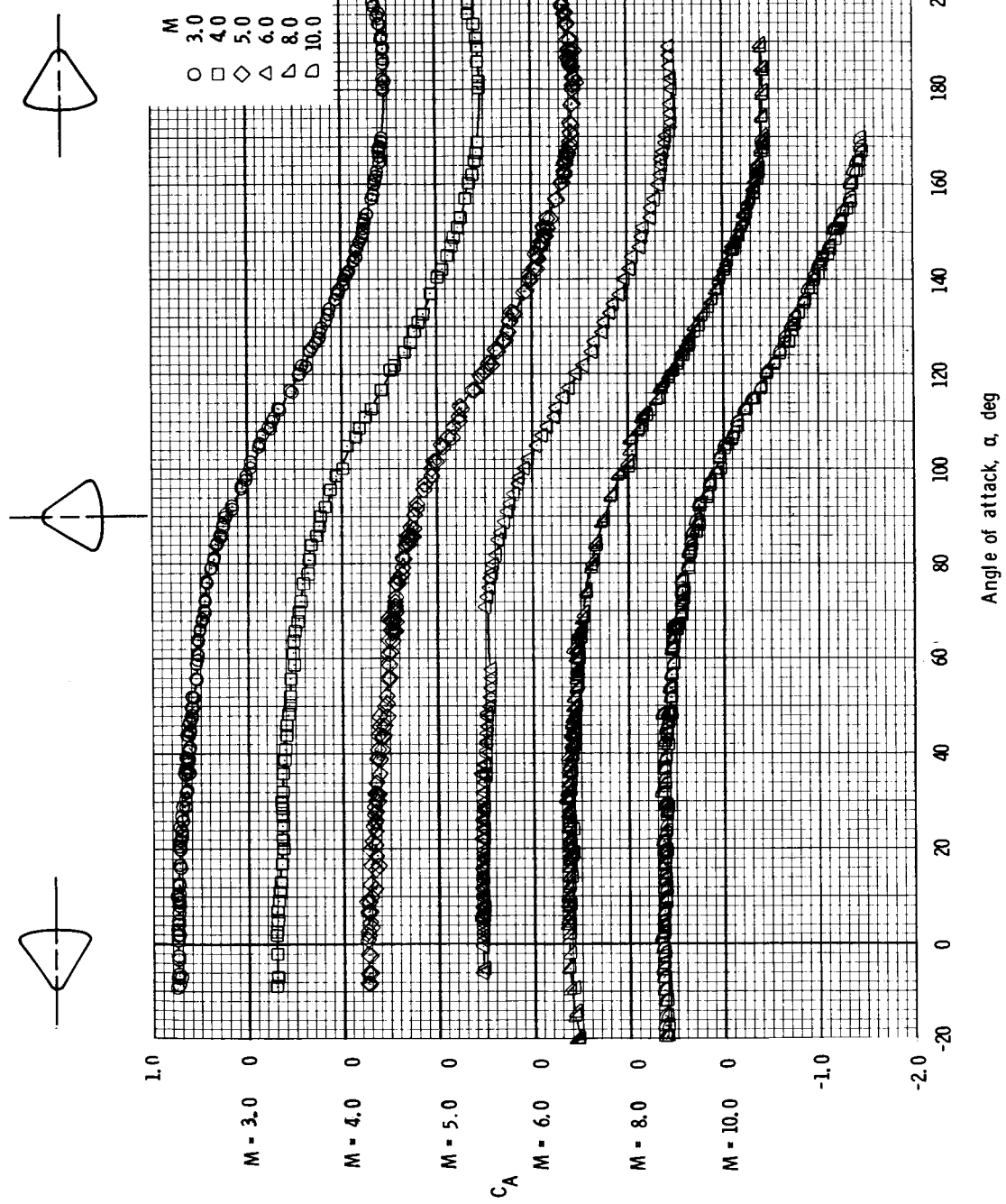
(b) Pitching-moment coefficient, $c \cdot g.$ ($\frac{x}{d} = -0.657$, $\frac{z}{d} = 0.035$).

Figure 7. - Continued.



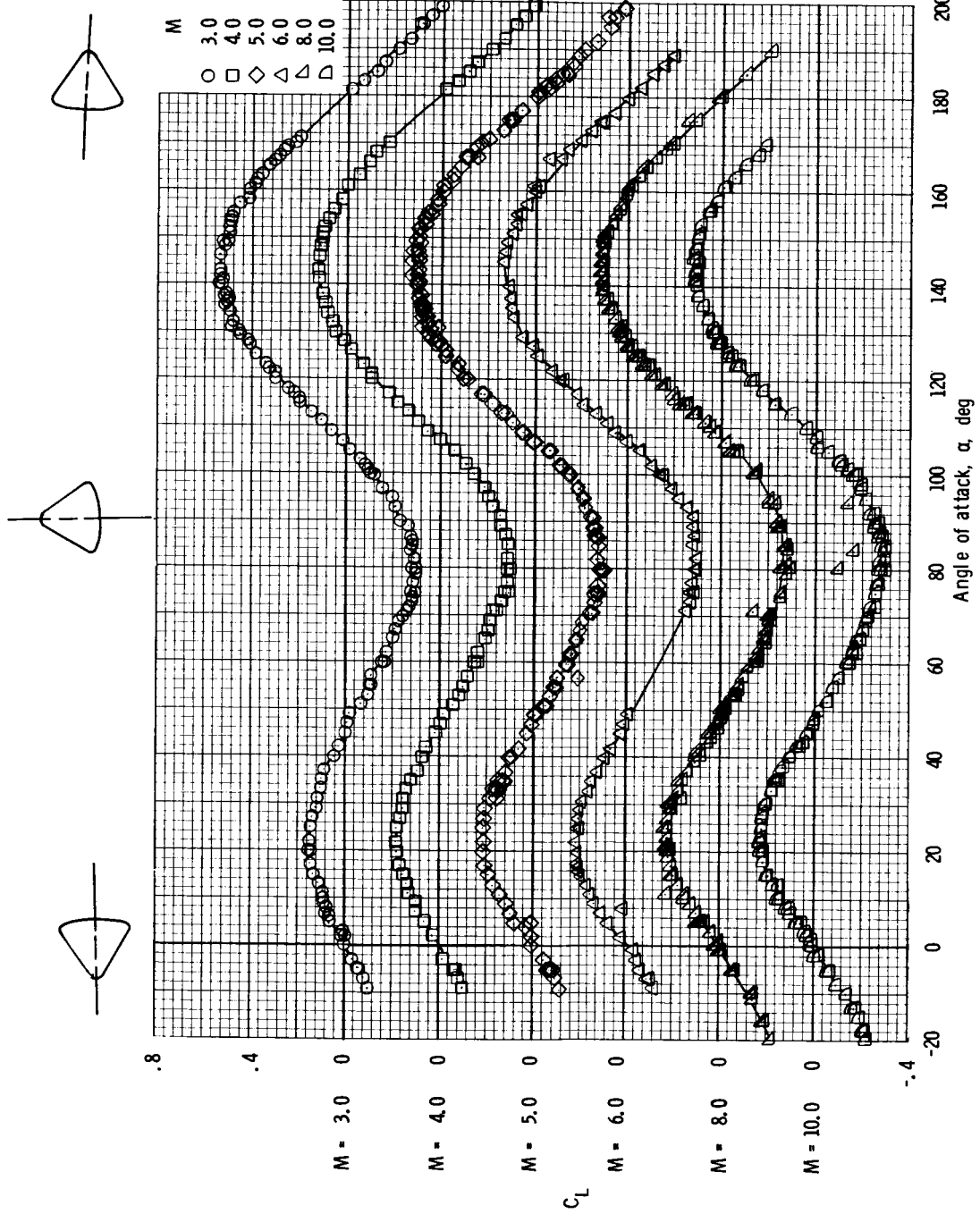
(c) Normal-force coefficient.

Figure 7.- Continued.



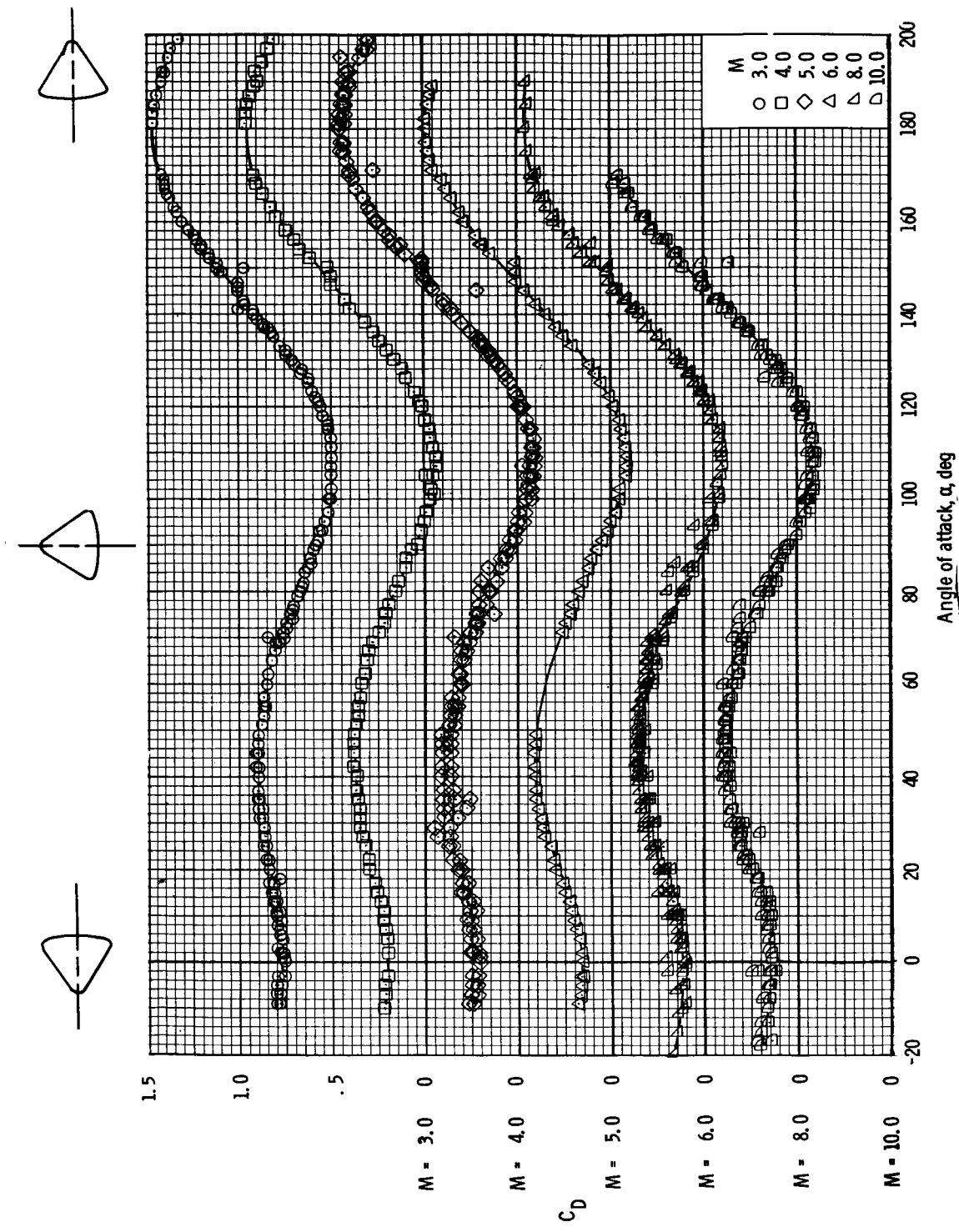
(d) Axial-force coefficient.

Figure 7. - Continued.



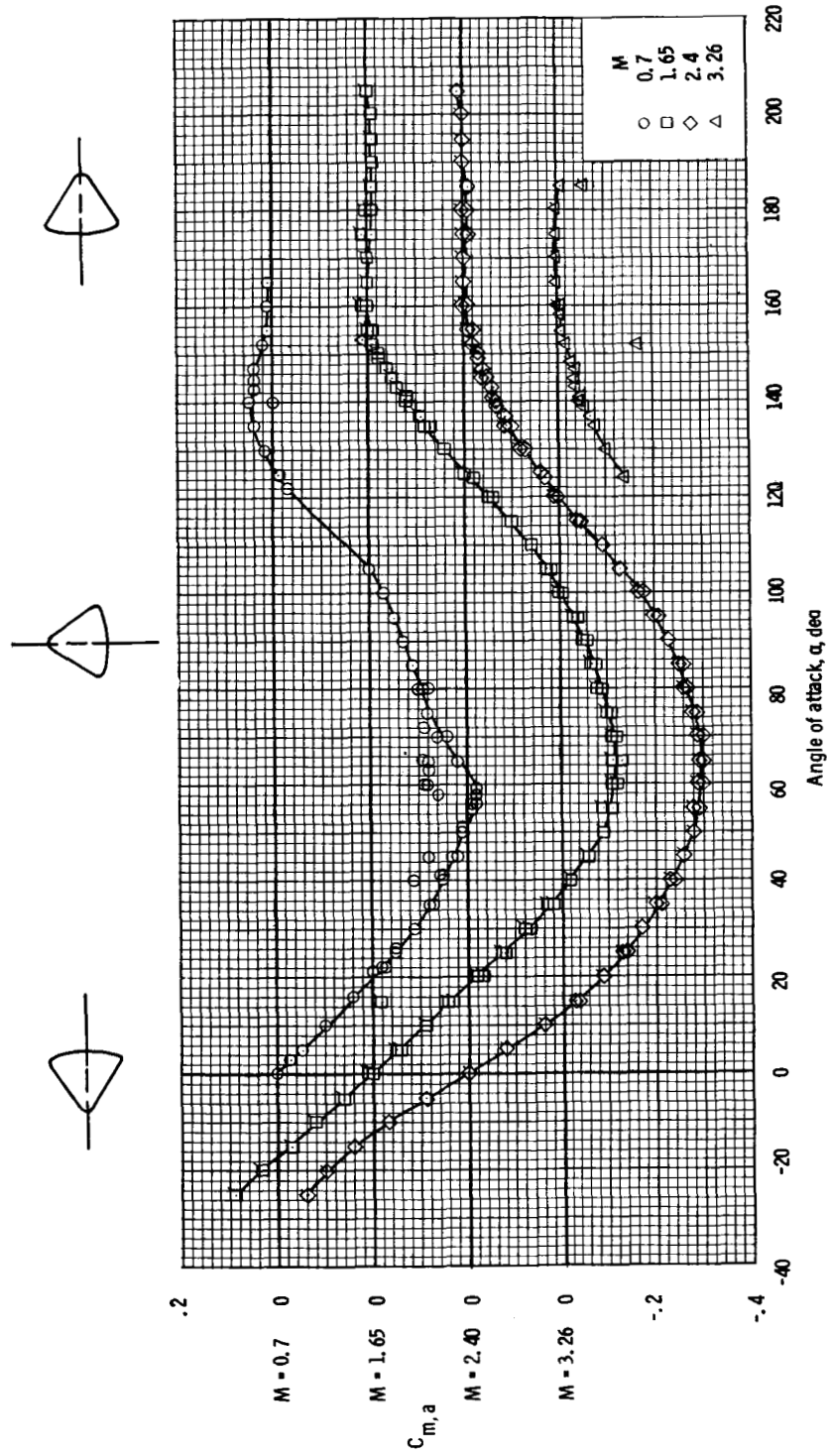
(e) Lift coefficient.

Figure 7. - Continued.



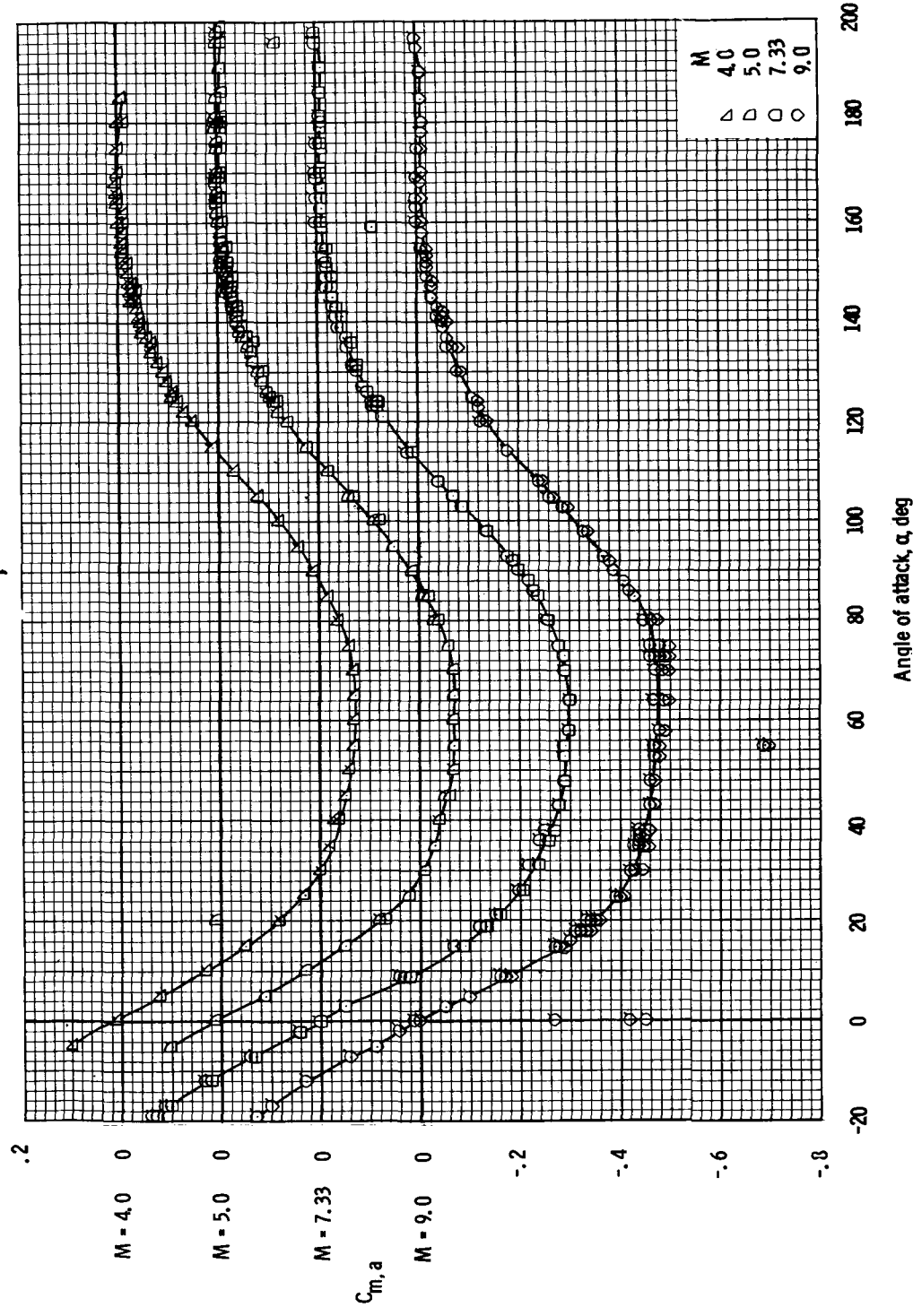
(f) Drag coefficient.

Figure 7. - Concluded.



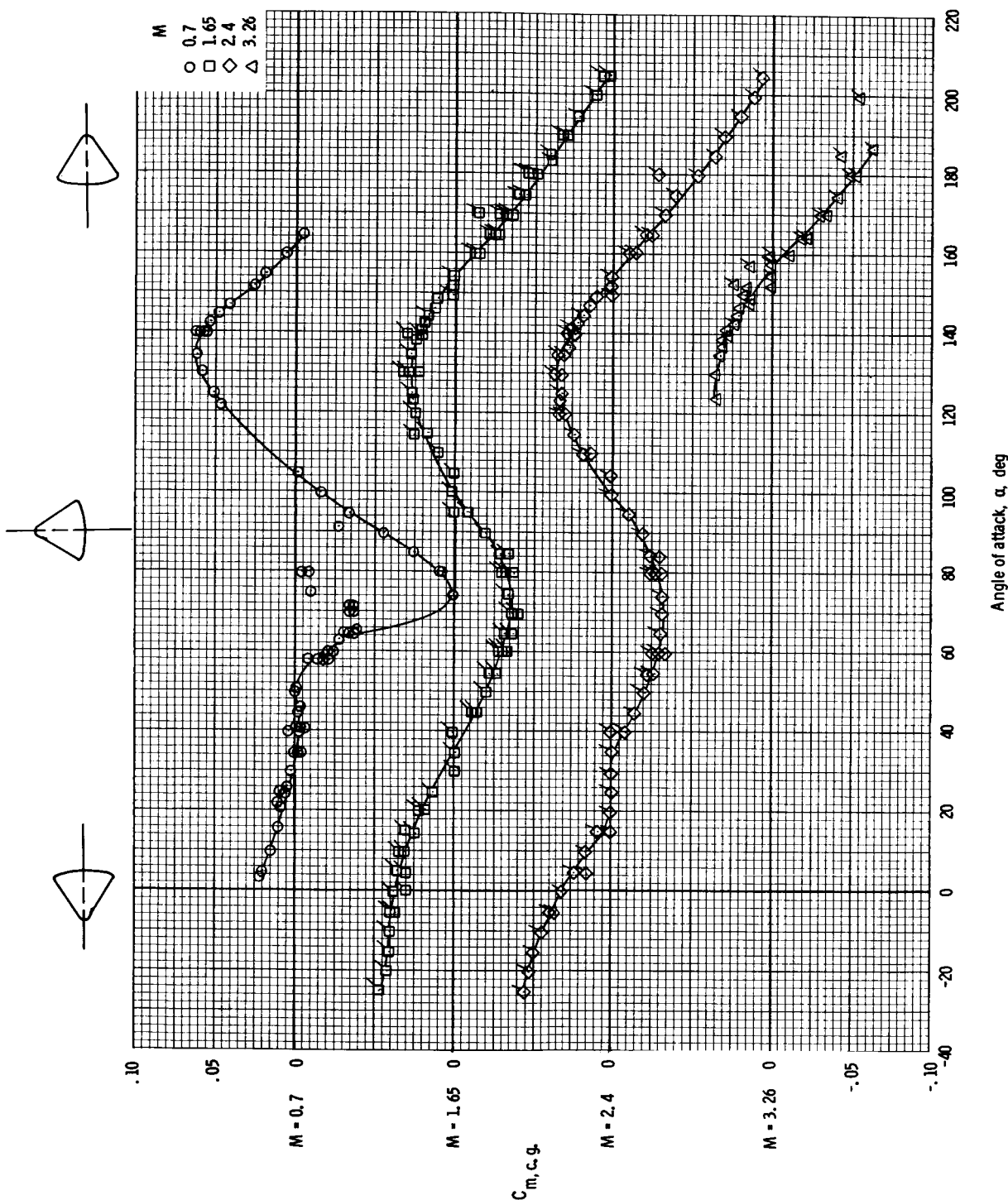
(a) Pitching-moment coefficient, apex, $M = 0.7$ to 3.26 (flagged symbols denote data for an alternate configuration).

Figure 8. - Aerodynamic characteristics of the Apollo CM (without protuberances) obtained at JPL-20SWT and JPL-21HWT at $M = 0.7$ to 9.0.

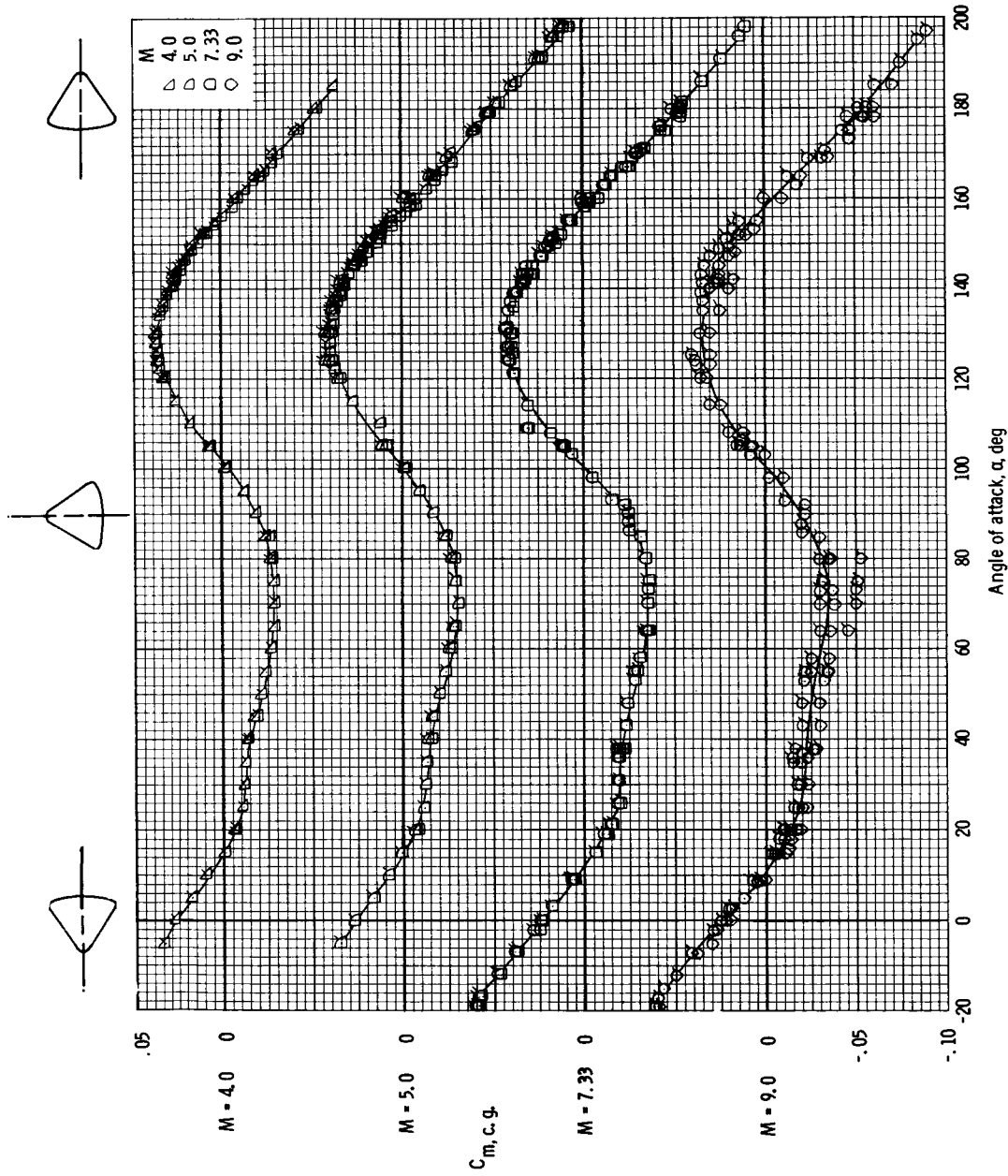


(b) Pitching-moment coefficient, apex, $M = 4.0$ to 9.0 (flagged symbols denote data for an alternate configuration).

Figure 8.- Continued.

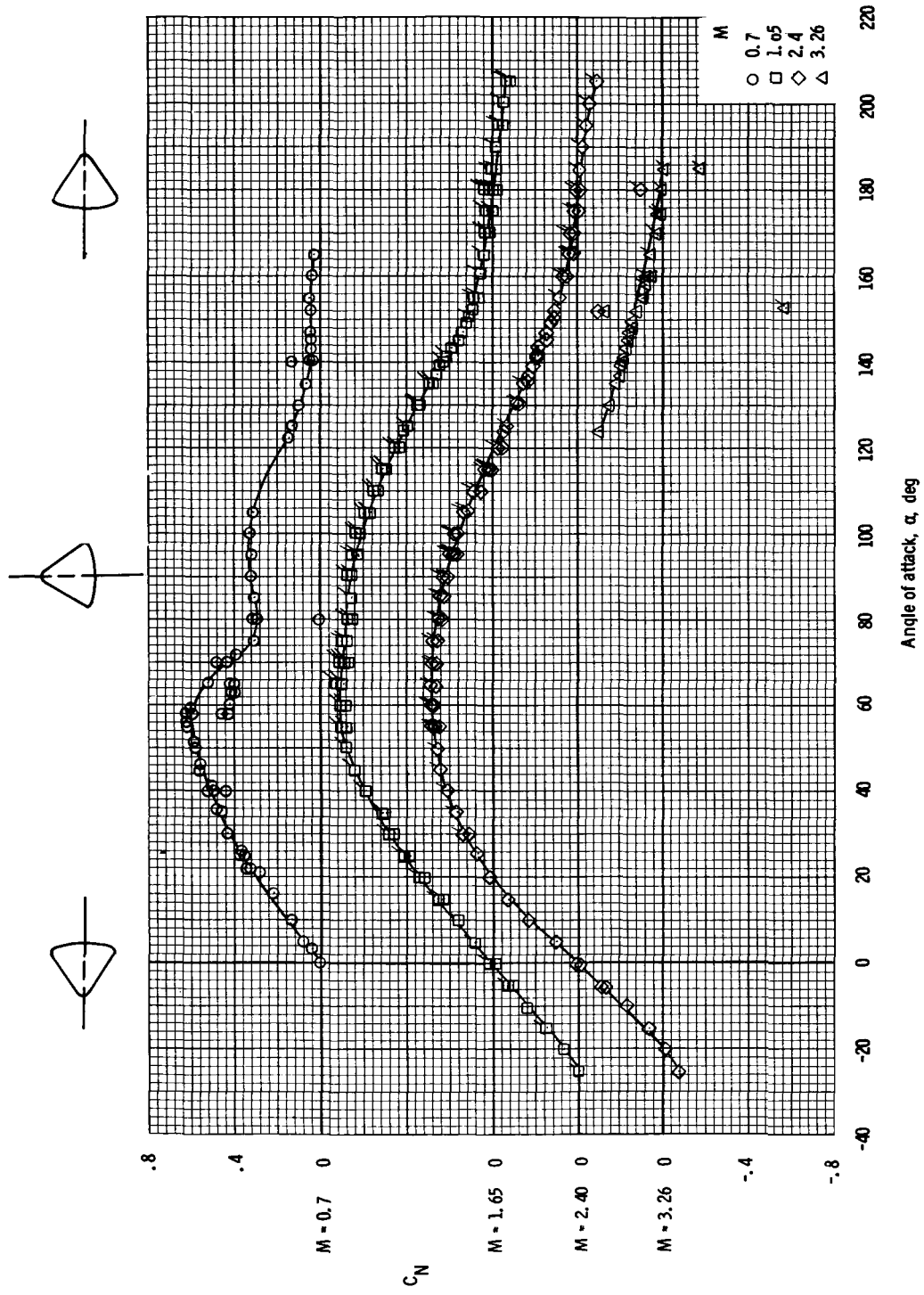


(c) Pitching-moment coefficient, c.g. $\left(\frac{x}{d} = -0.657, \frac{z}{d} = 0.035 \right)$, $M = 0.7$ to 3.26
 (flagged symbols denote data for an alternate configuration).



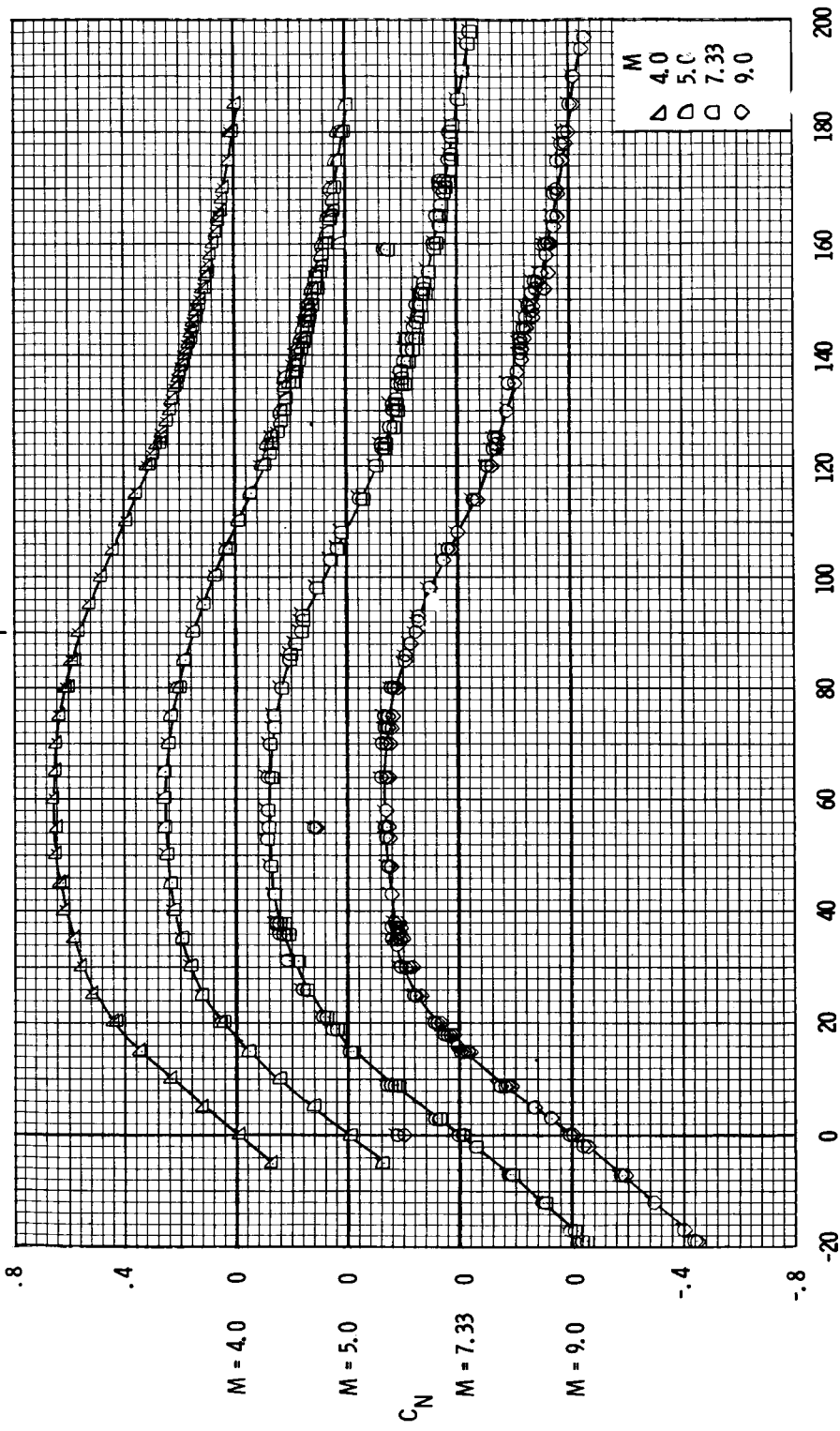
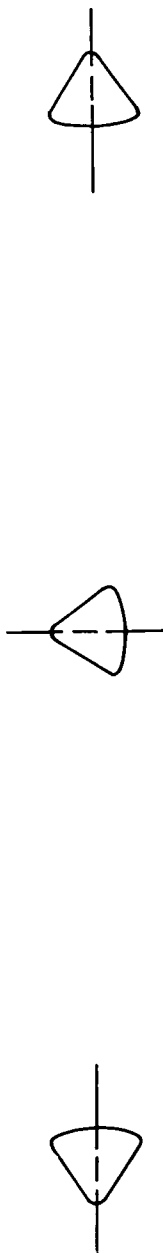
(d) Pitching-moment coefficient, c.g. $\left(\frac{x}{d} = -0.657, \frac{z}{d} = 0.035 \right)$, $M = 4.0$ to 9.0
 flagged symbols denote data for an alternate configuration).

Figure 8. - Continued.



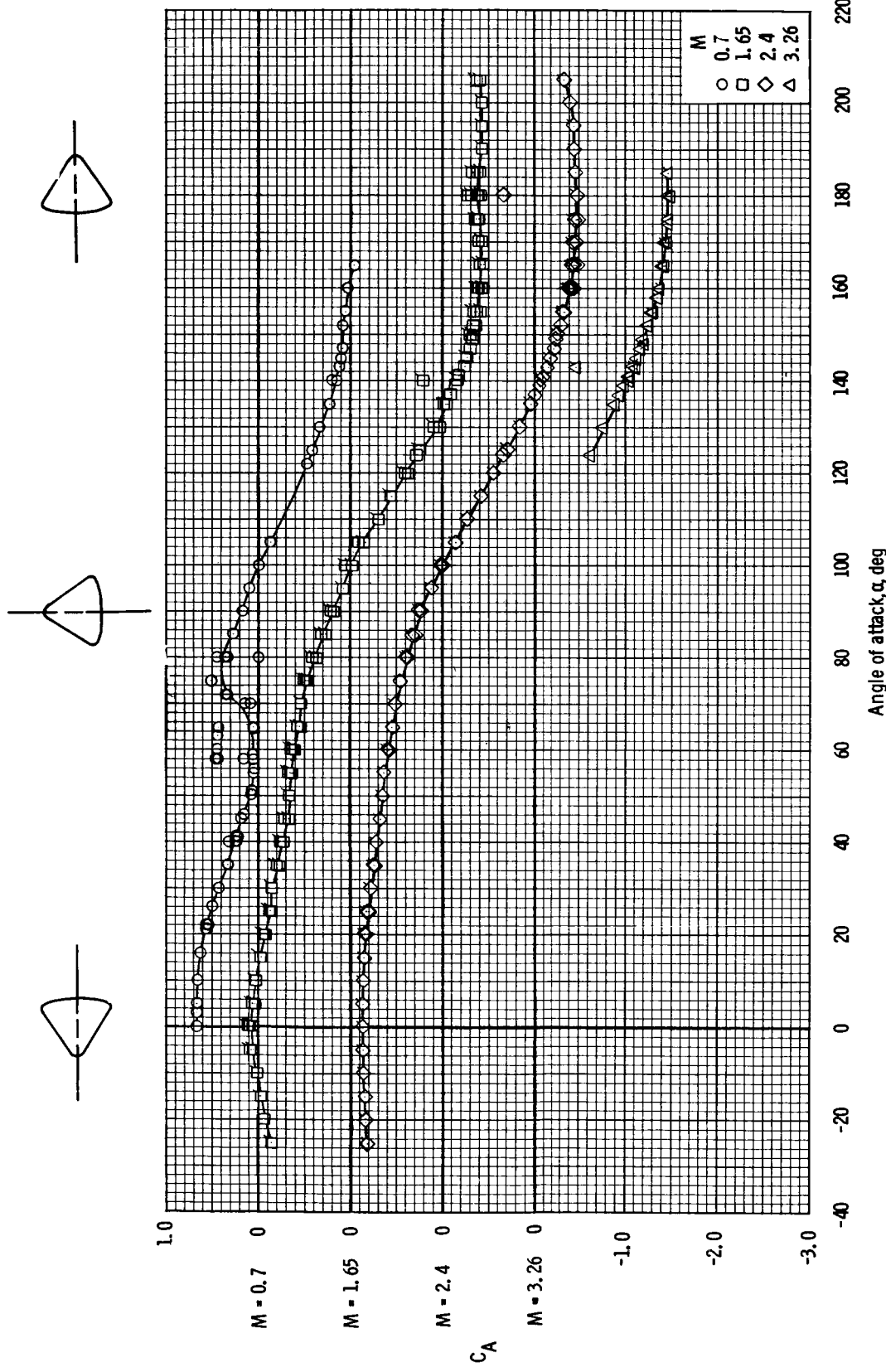
(e) Normal-force coefficient, $M = 0.7$ to 3.26 (flagged symbols denote data for an alternate configuration).

Figure 8. - Continued.



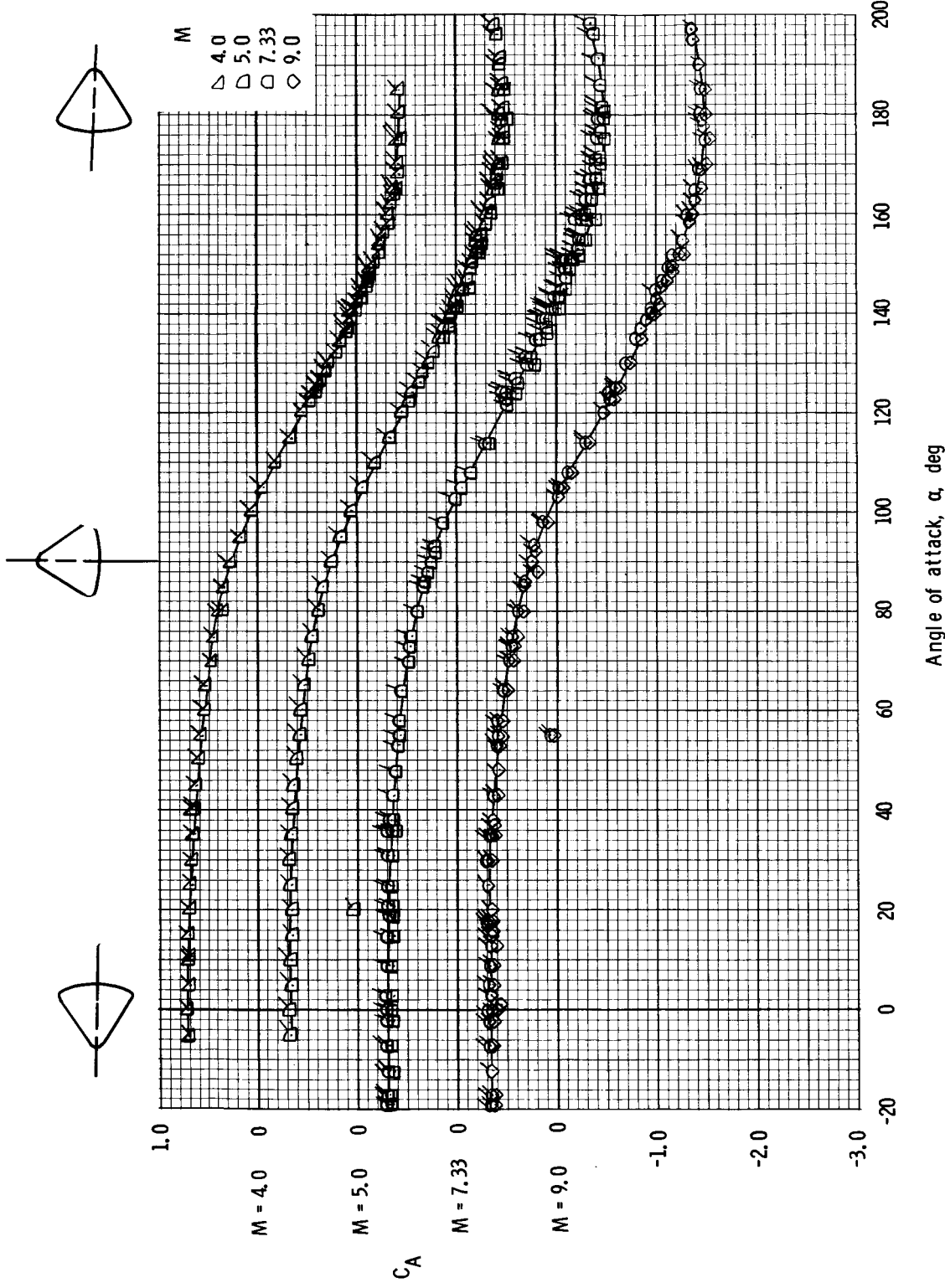
(f) Normal-force coefficient, $M = 4.0$ to 9.0 (flagged symbols denote data for an alternate configuration).

Figure 8. - Continued.



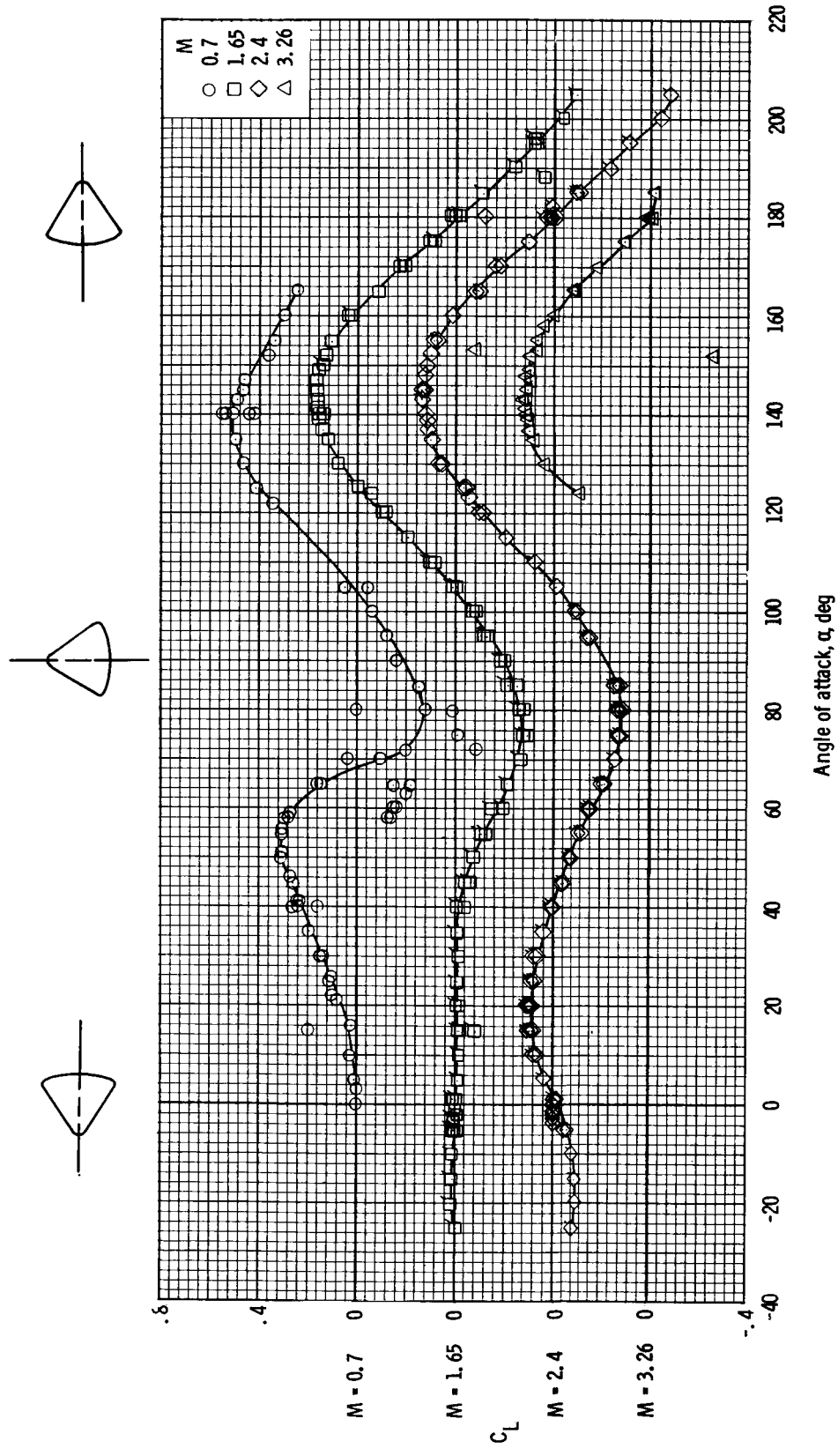
(g) Axial-force coefficient, $M = 0.7$ to 3.26 (flagged symbols denote data for an alternate configuration).

Figure 8. - Continued.



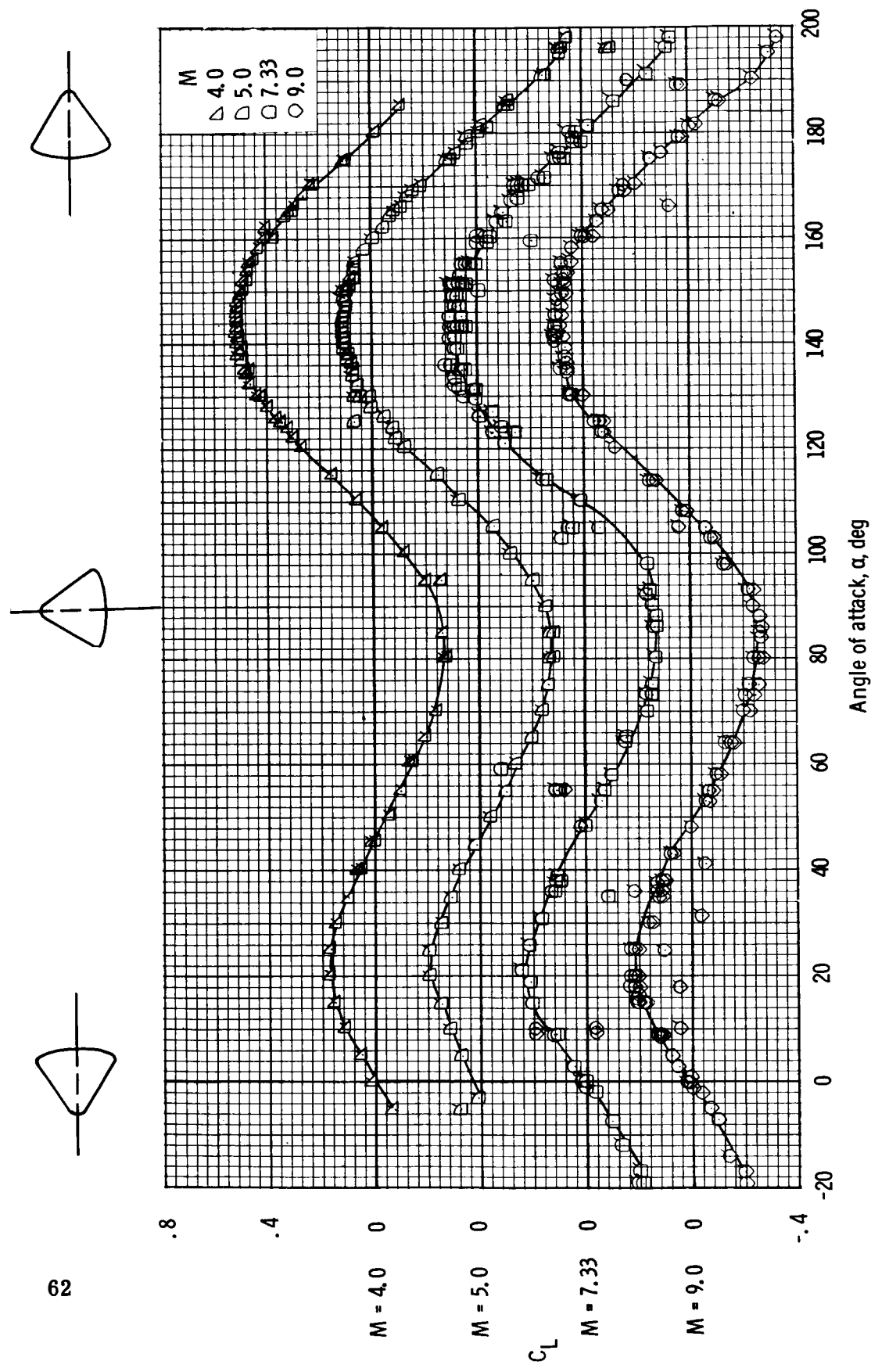
(h) Axial-force coefficient, $M = 4.0$ to 9.0 (flagged symbols denote data for an alternate configuration).

Figure 8. - Continued.



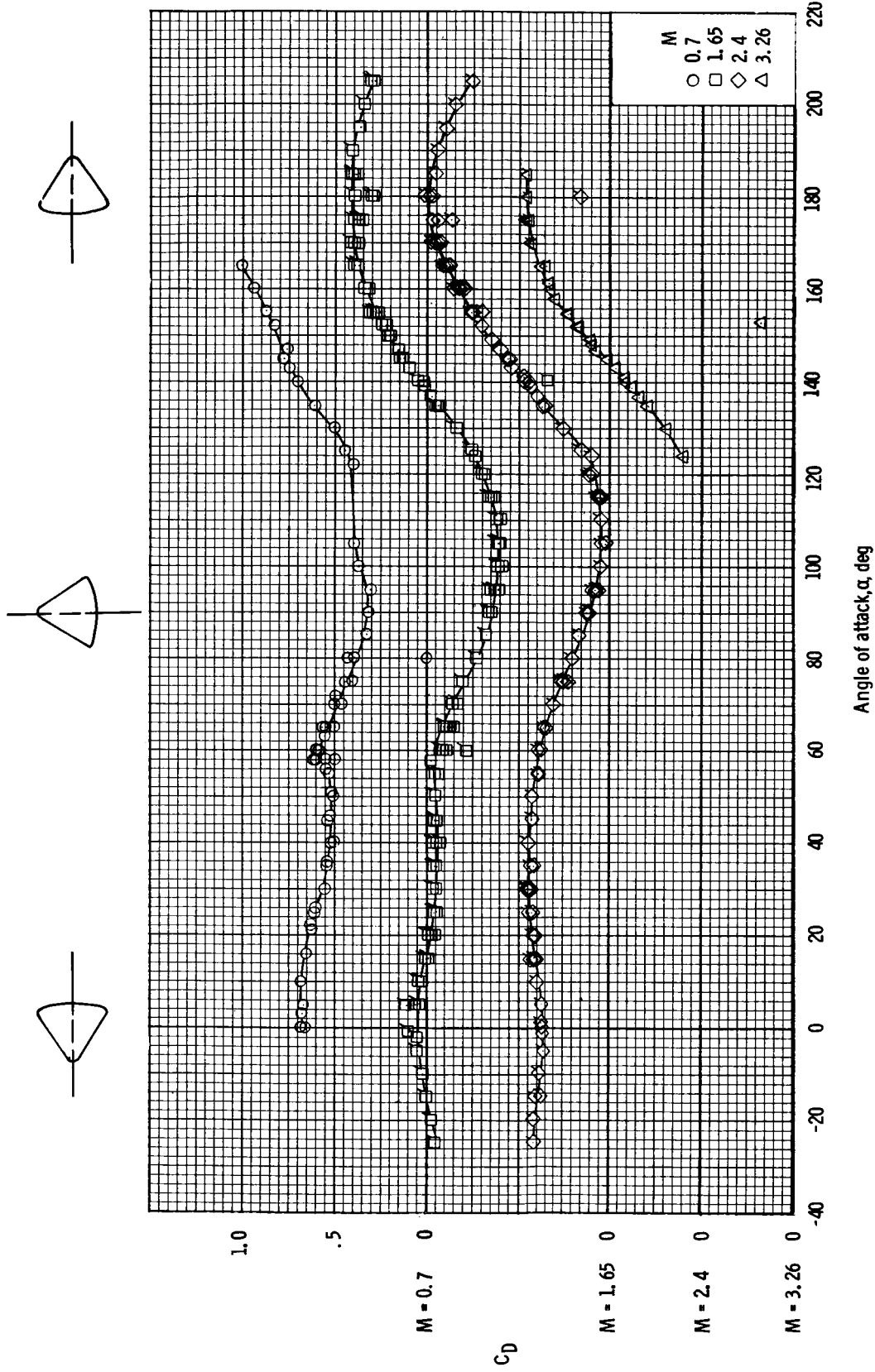
(i) Lift coefficient, $M = 0.7$ to 3.26 (flagged symbols denote data for an alternate configuration).

Figure 8. - Continued.



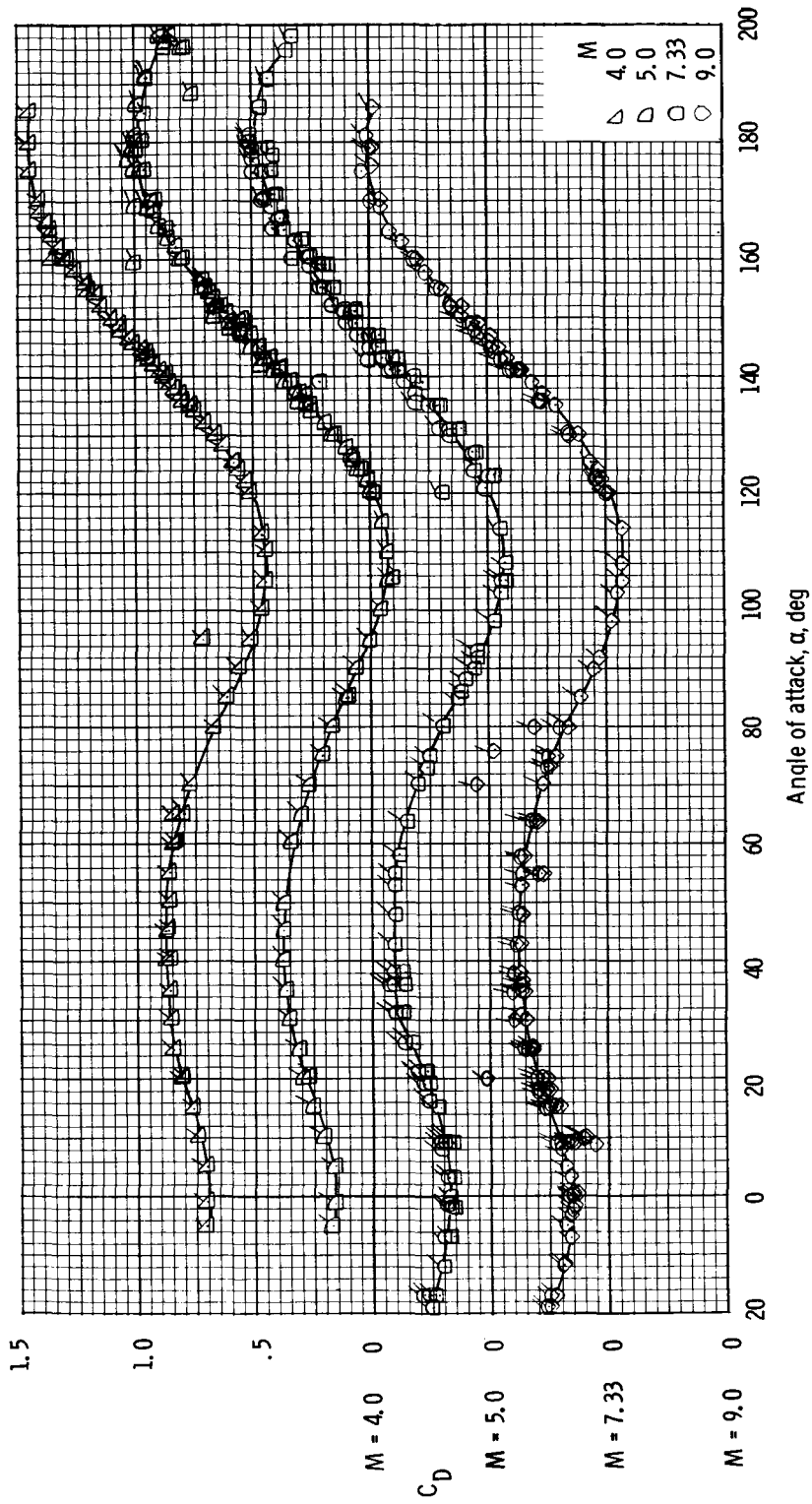
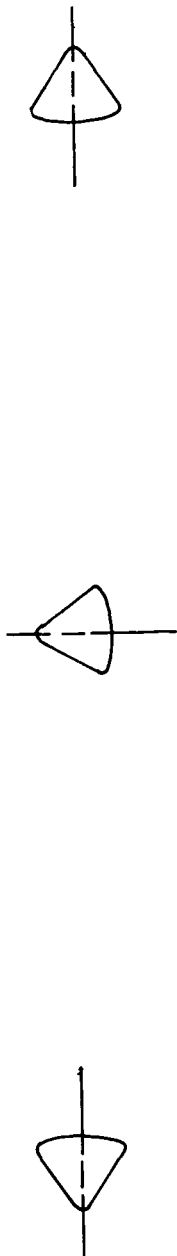
(j) Lift coefficient, $M = 4.0$ to 9.0 (flagged symbols denote data for an alternate configuration).

Figure 8. - Continued.



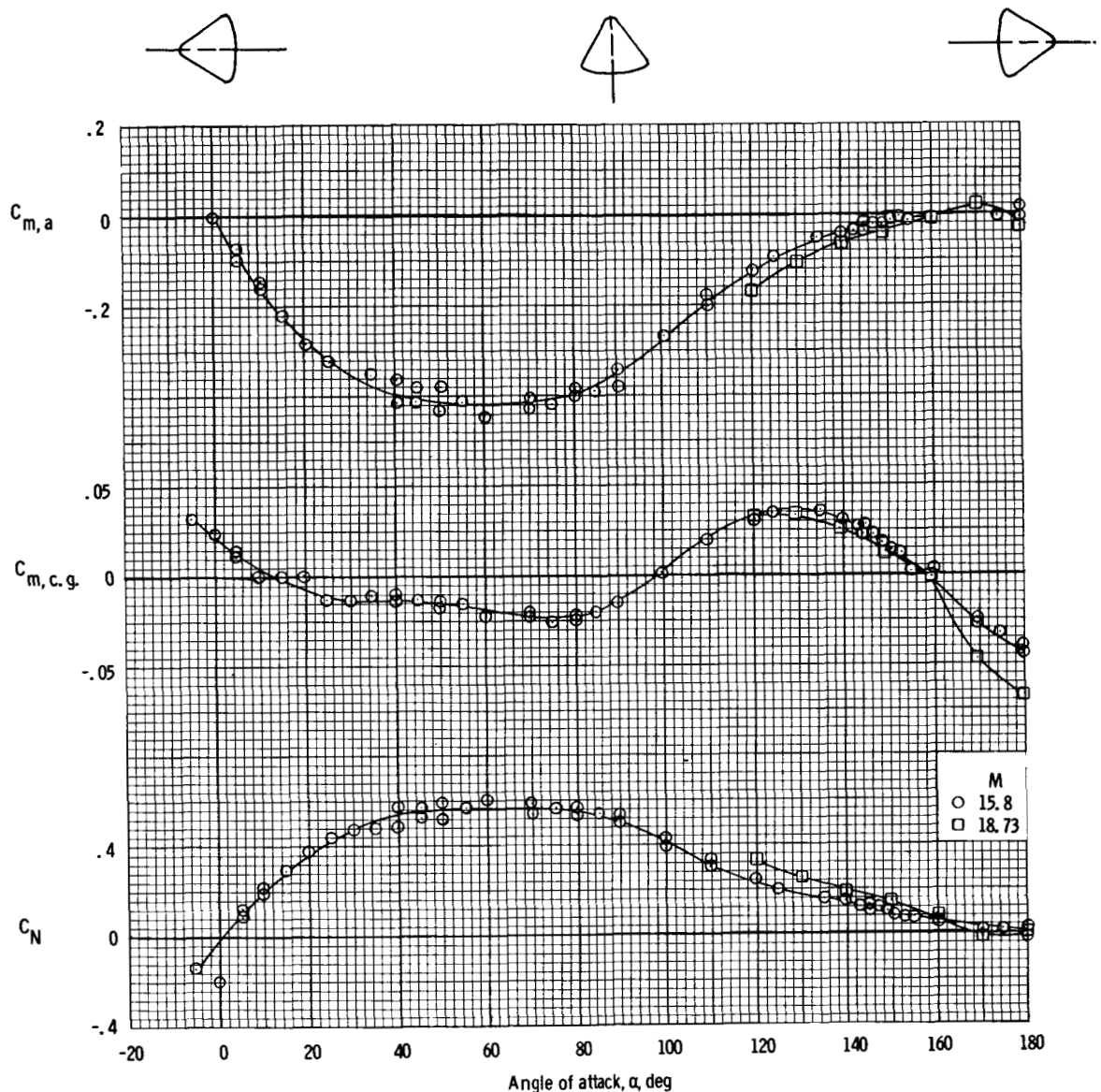
(k) Drag coefficient, $M = 0.7$ to 3.26 (flagged symbols denote data for an alternate configuration).

Figure 8. - Continued.



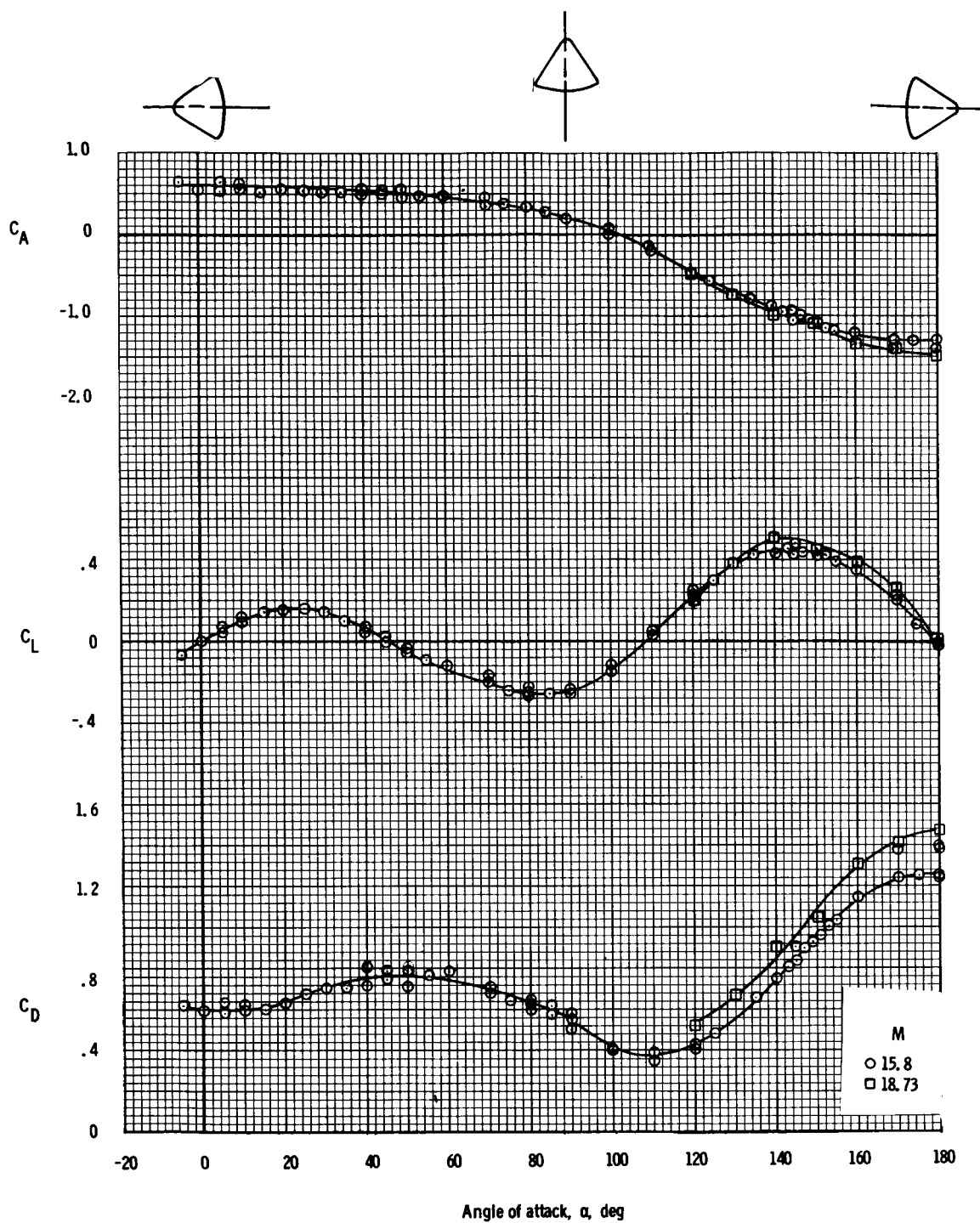
- (1) Drag coefficient, $M = 4.0$ to 9.0 (flagged symbols denote data for an alternate configuration).

Figure 8. - Concluded.



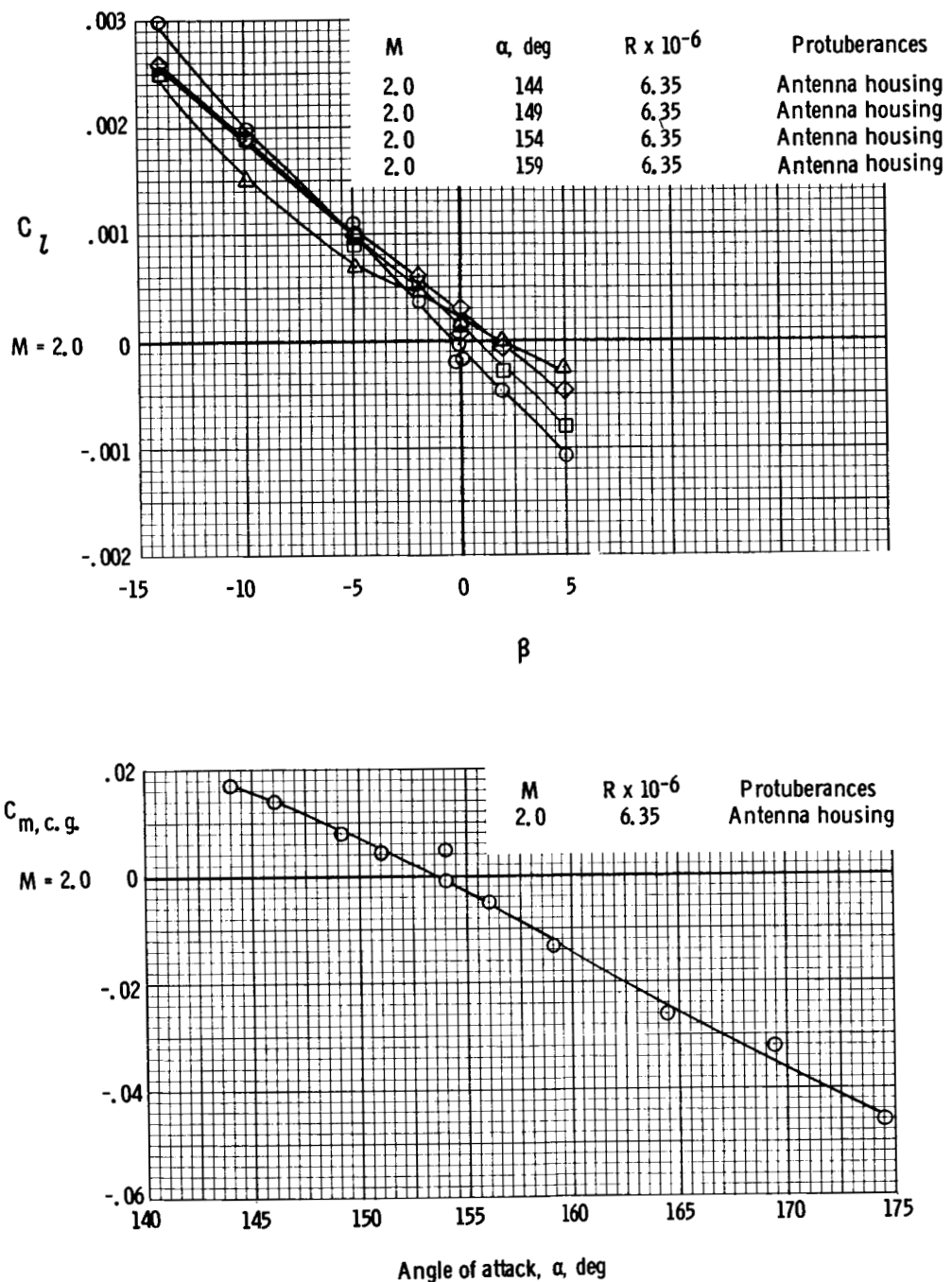
(a) Pitching-moment and normal-force coefficients.

Figure 9. - Aerodynamic characteristics of the Apollo CM (without protuberances) obtained at AEDC-H and CAL-48ST facilities at $M = 15.8$ and 18.73 ($\frac{x}{d} = -0.657$, $\frac{z}{d} = 0.035$).



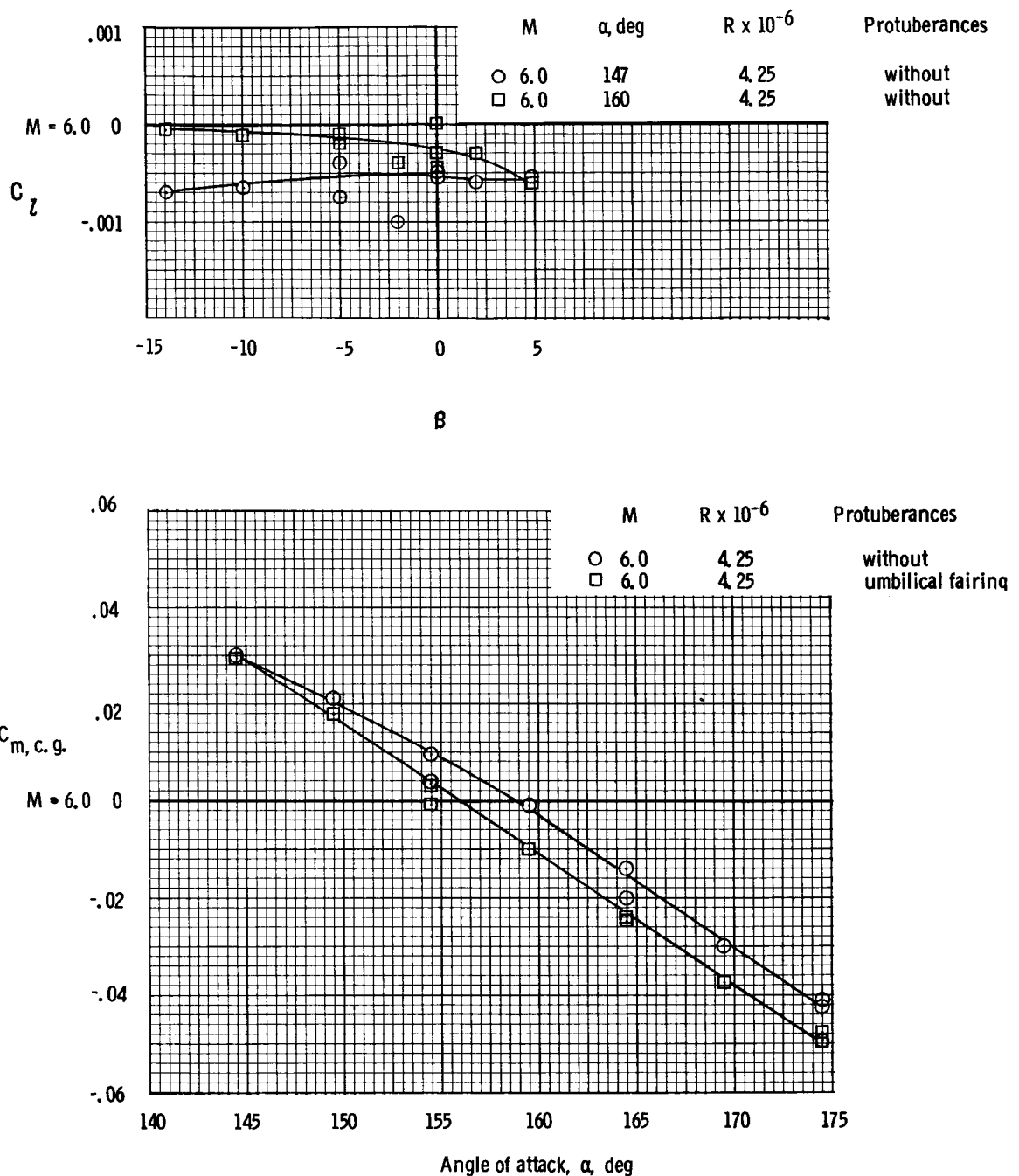
(b) Axial-force, lift, and drag coefficients.

Figure 9.- Concluded.



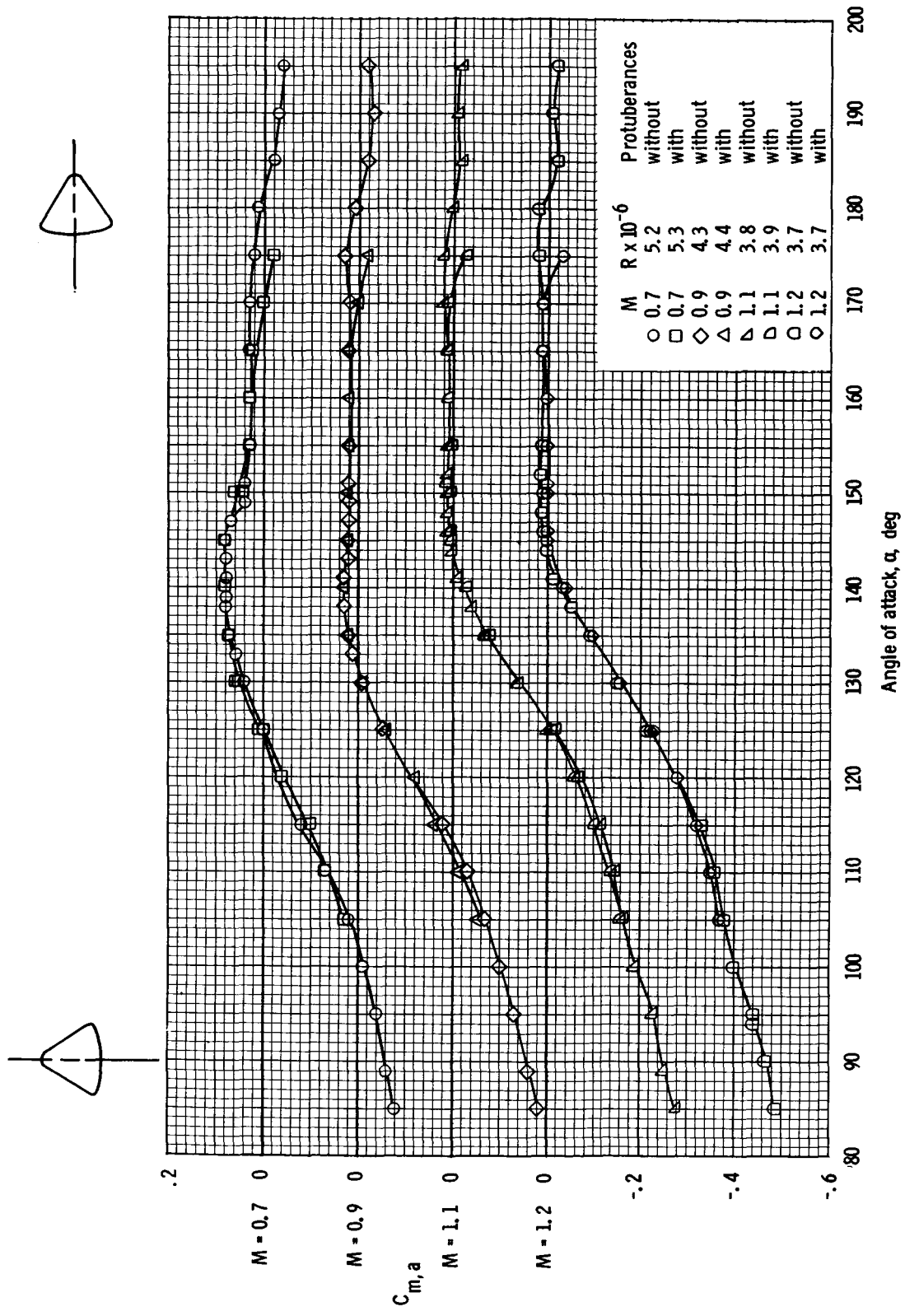
(a) Pitching- and rolling-moment coefficients, $M = 2.0$.

Figure 10. - Aerodynamic characteristics of the Apollo CM (with and without protuberances) obtained at AEDC-A at $M = 2.0$ and 6.0
 $\left(\frac{x}{d} = -0.657, \frac{z}{d} = 0.035\right)$.



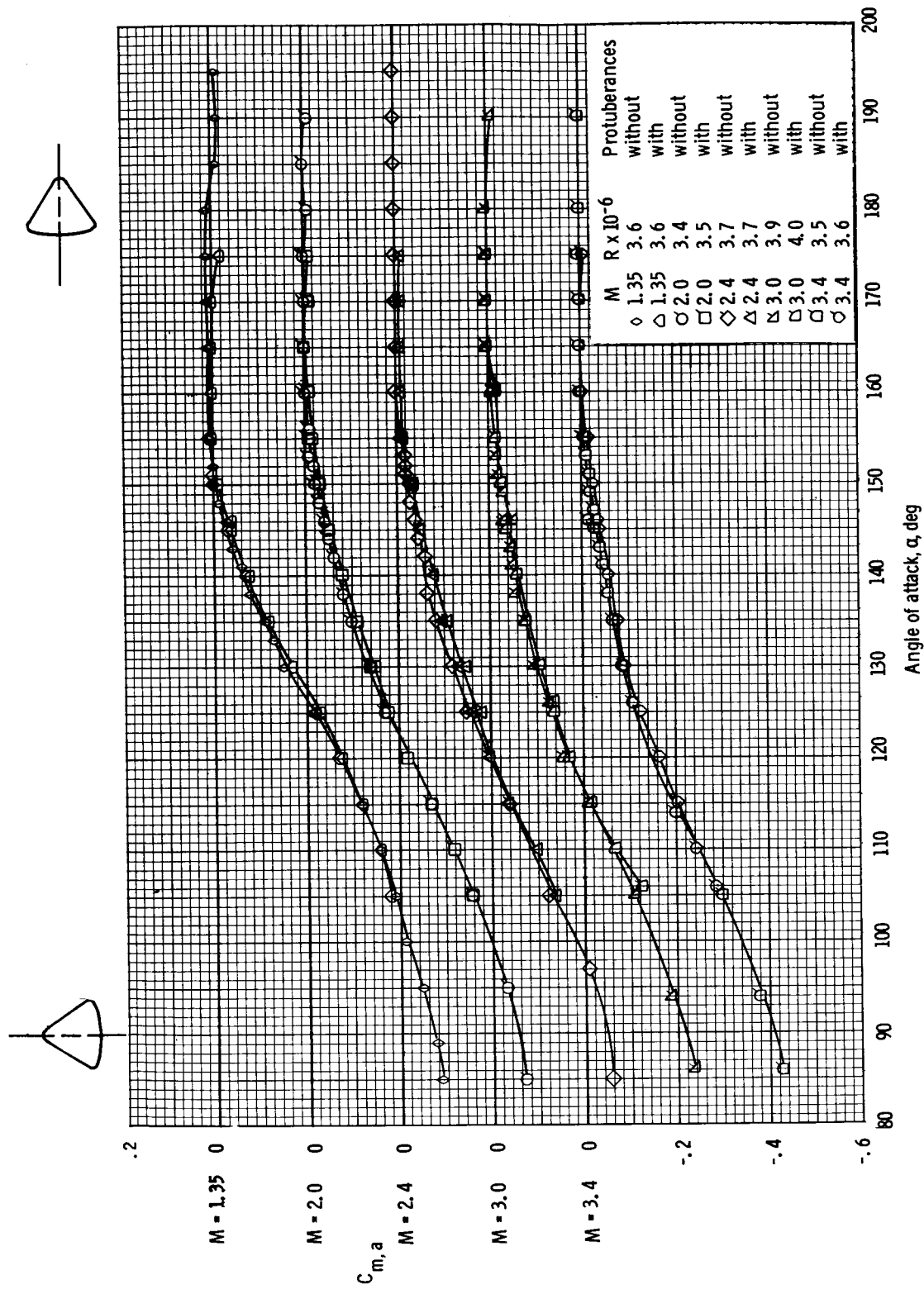
(b) Pitching- and rolling-moment coefficients, $M = 6.0$.

Figure 10. - Concluded.



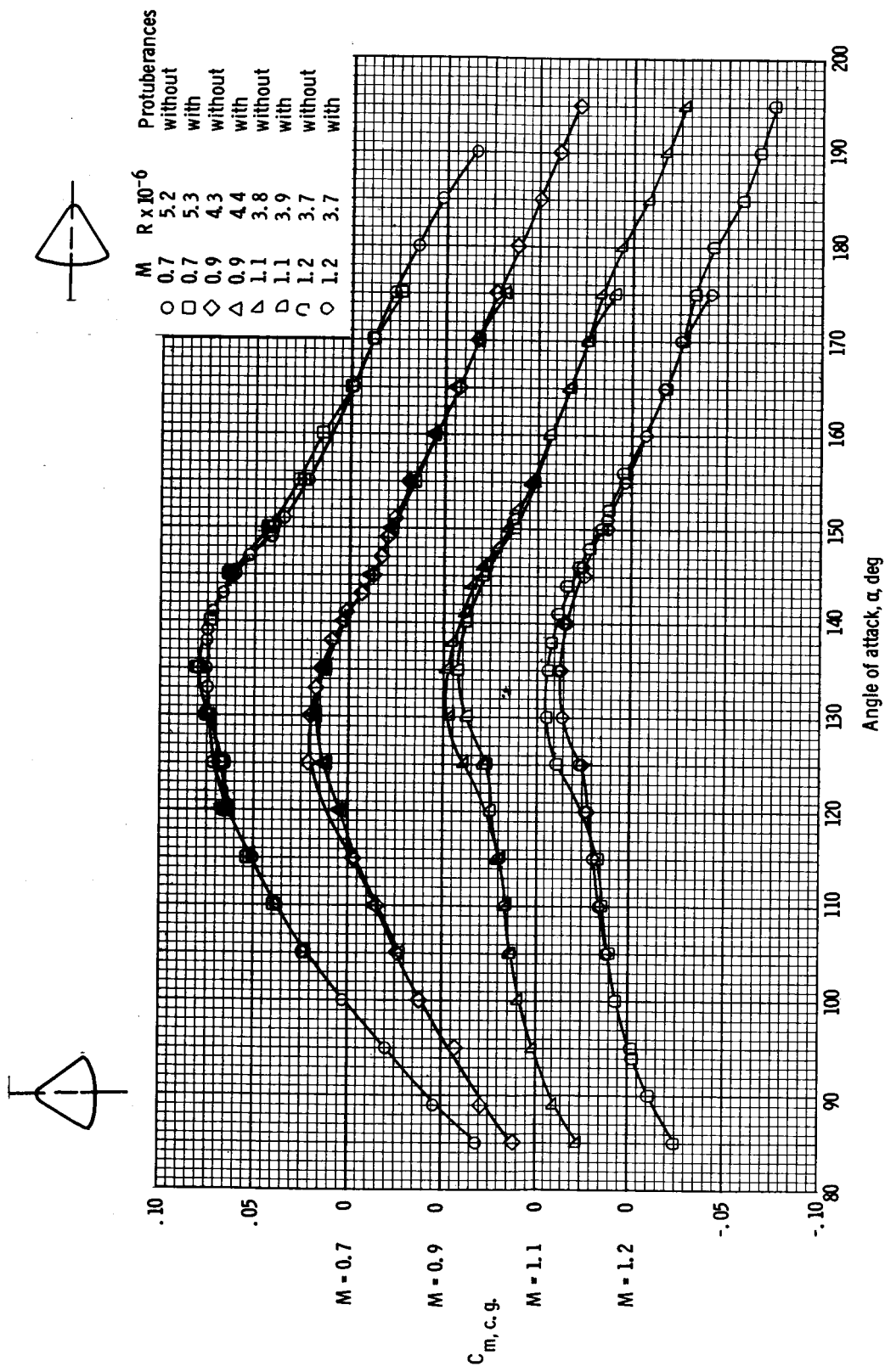
(a) Pitching-moment coefficient, apex, $M = 0.7$ to 1.2.

Figure 11. - Comparison of aerodynamic characteristics of the Apollo CM, with and without protuberances, obtained at Ames UPWT at $M = 0.7$ to 3.4.



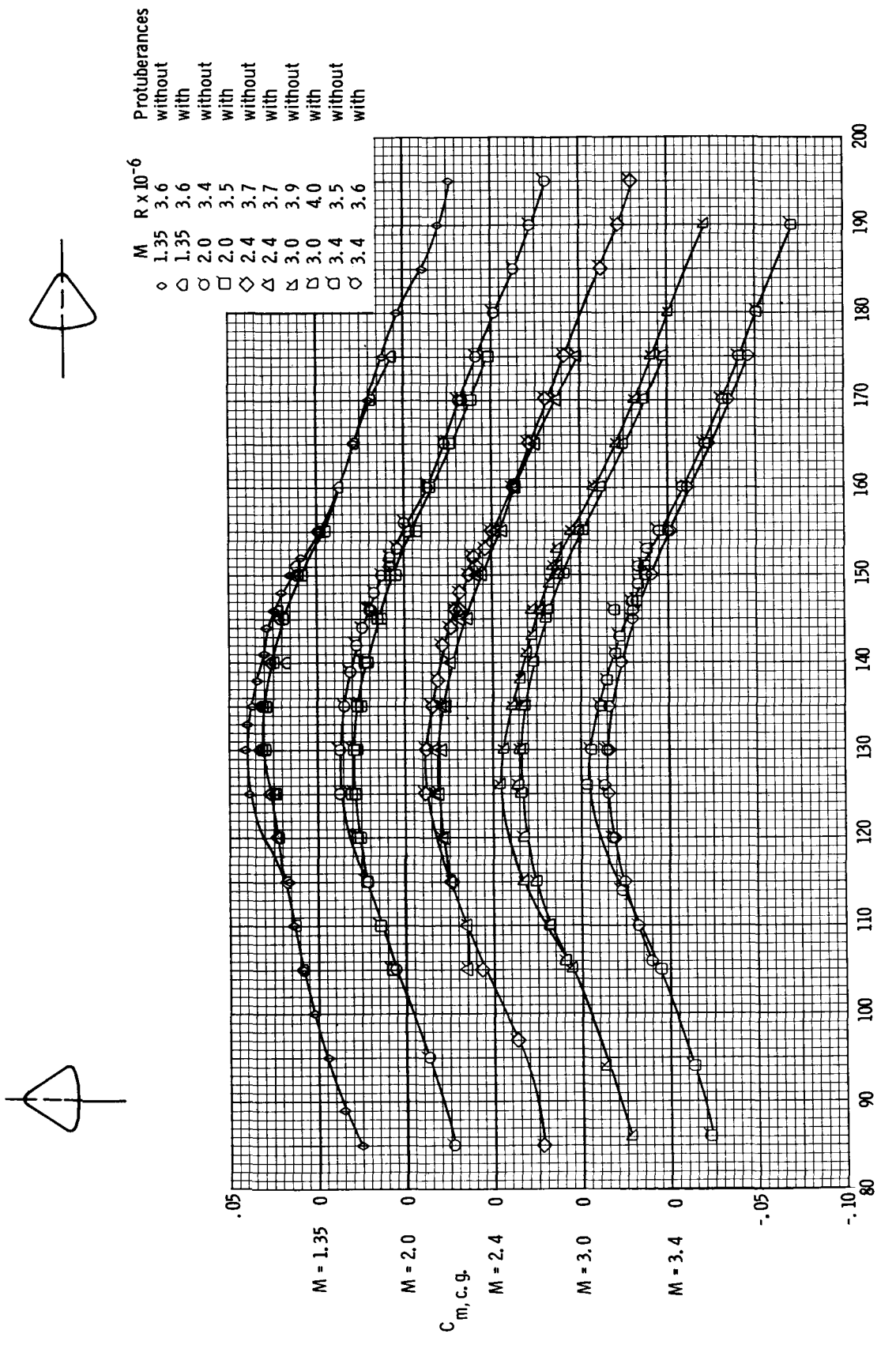
(b) Pitching-moment coefficient, apex, $M = 1.35$ to 3.4 .

Figure 11. - Continued.



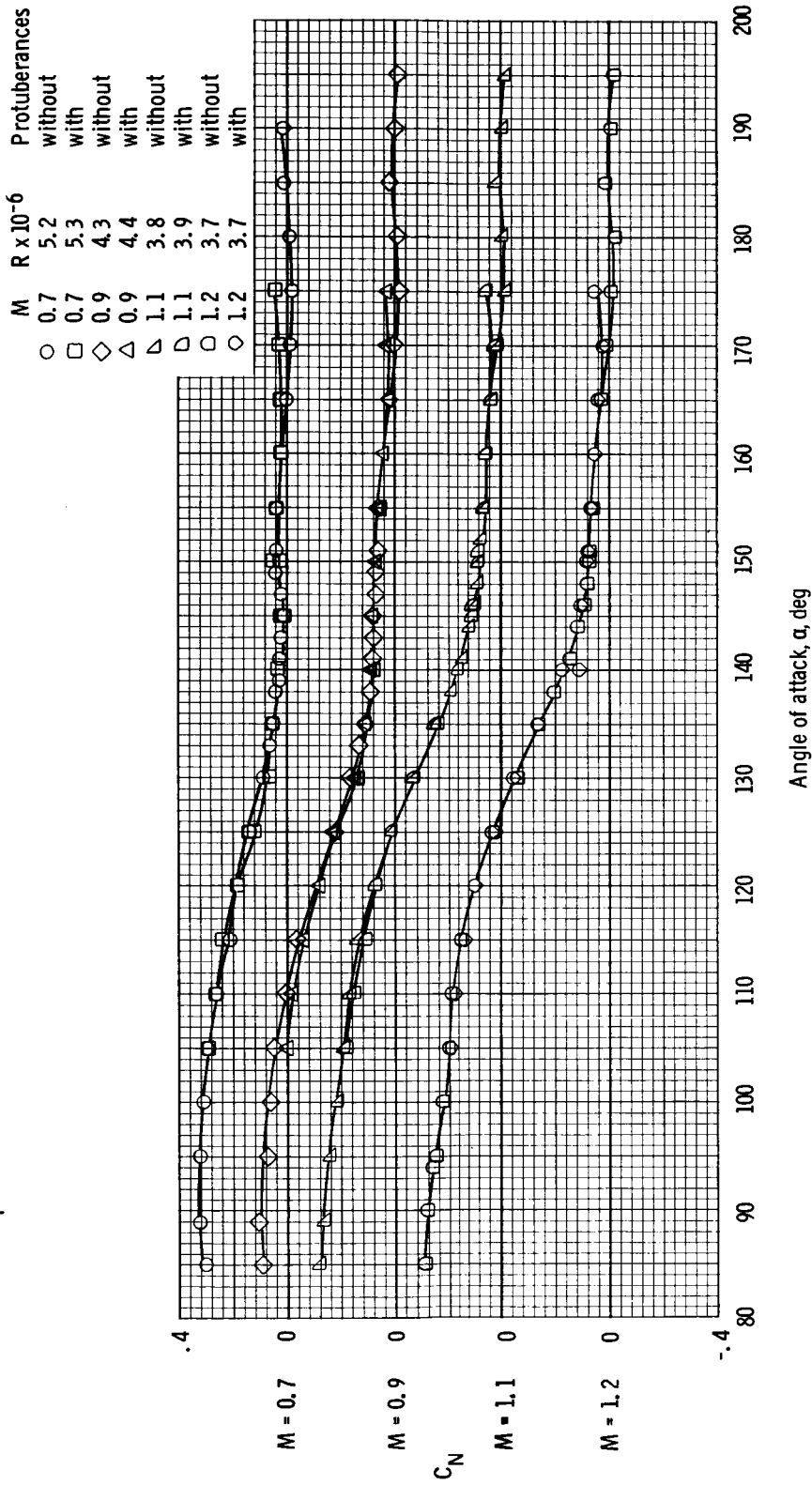
(c) Pitching-moment coefficient, c.g. $\left(\frac{x}{d} = -0.657, \frac{z}{d} = 0.035 \right)$, $M = 0.7$ to 1.2 .

Figure 11. - Continued.



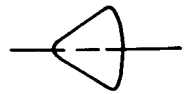
(d) Pitching-moment coefficient, c.g. $\left(\frac{x}{d} = -0.657, \frac{z}{d} = 0.035 \right)$, $M = 1.35$ to 3.4 .

Figure 11.- Continued.

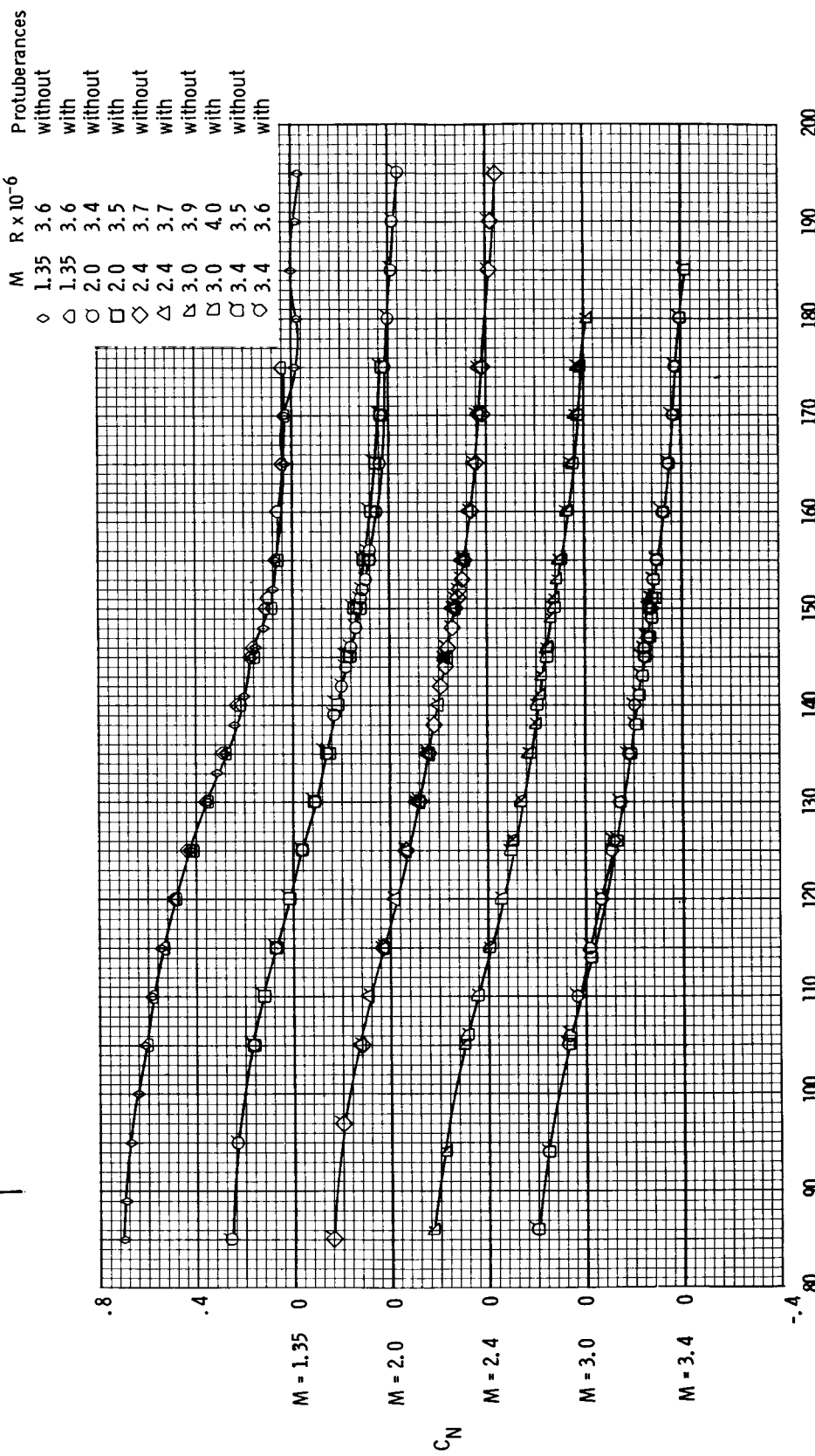


(e) Normal-force coefficient, $M = 0.7$ to 1.2 .

Figure 11.- Continued.

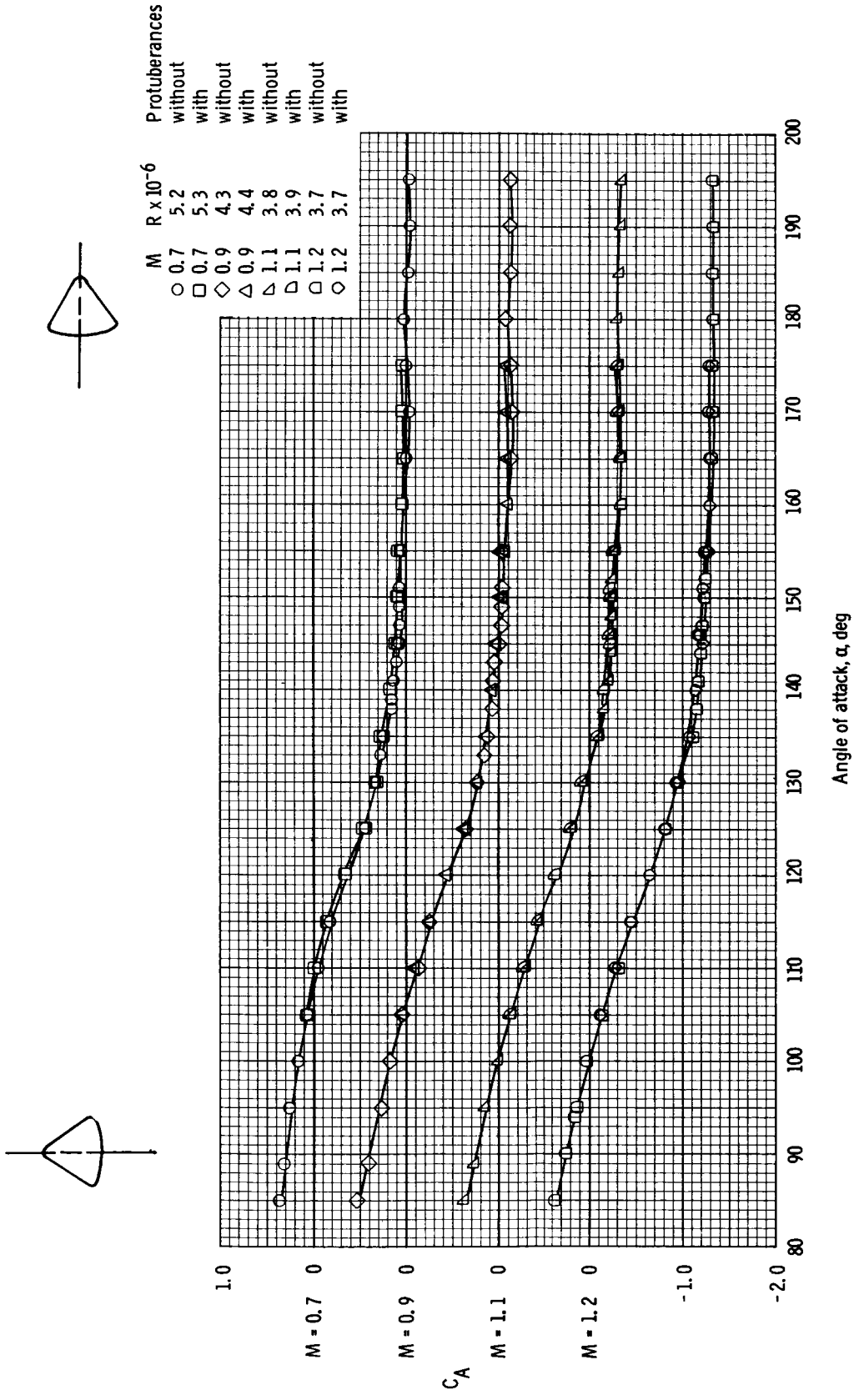


74



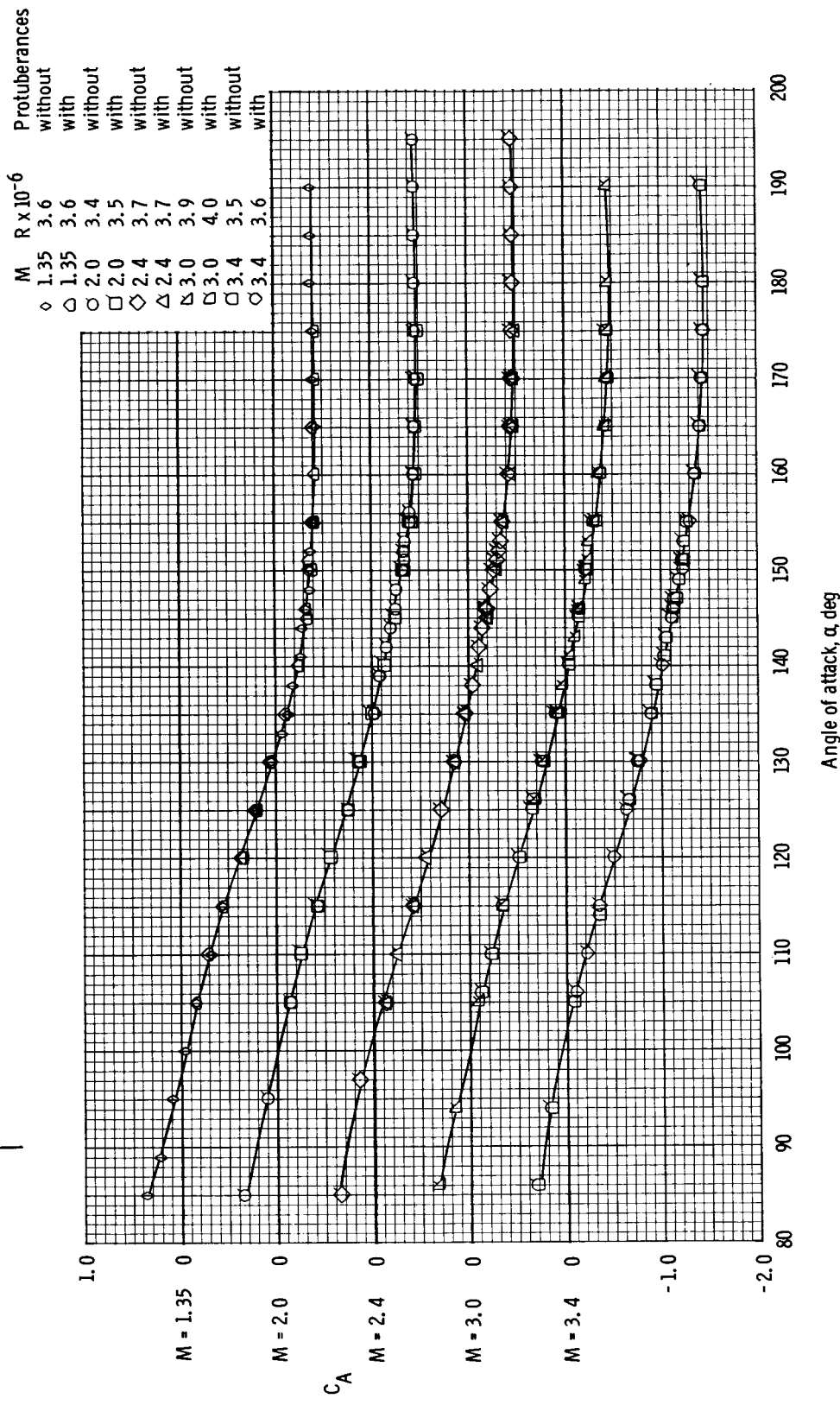
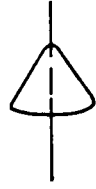
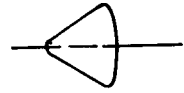
(f) Normal-force coefficient, $M = 1.35$ to 3.4 .

Figure 11. - Continued.



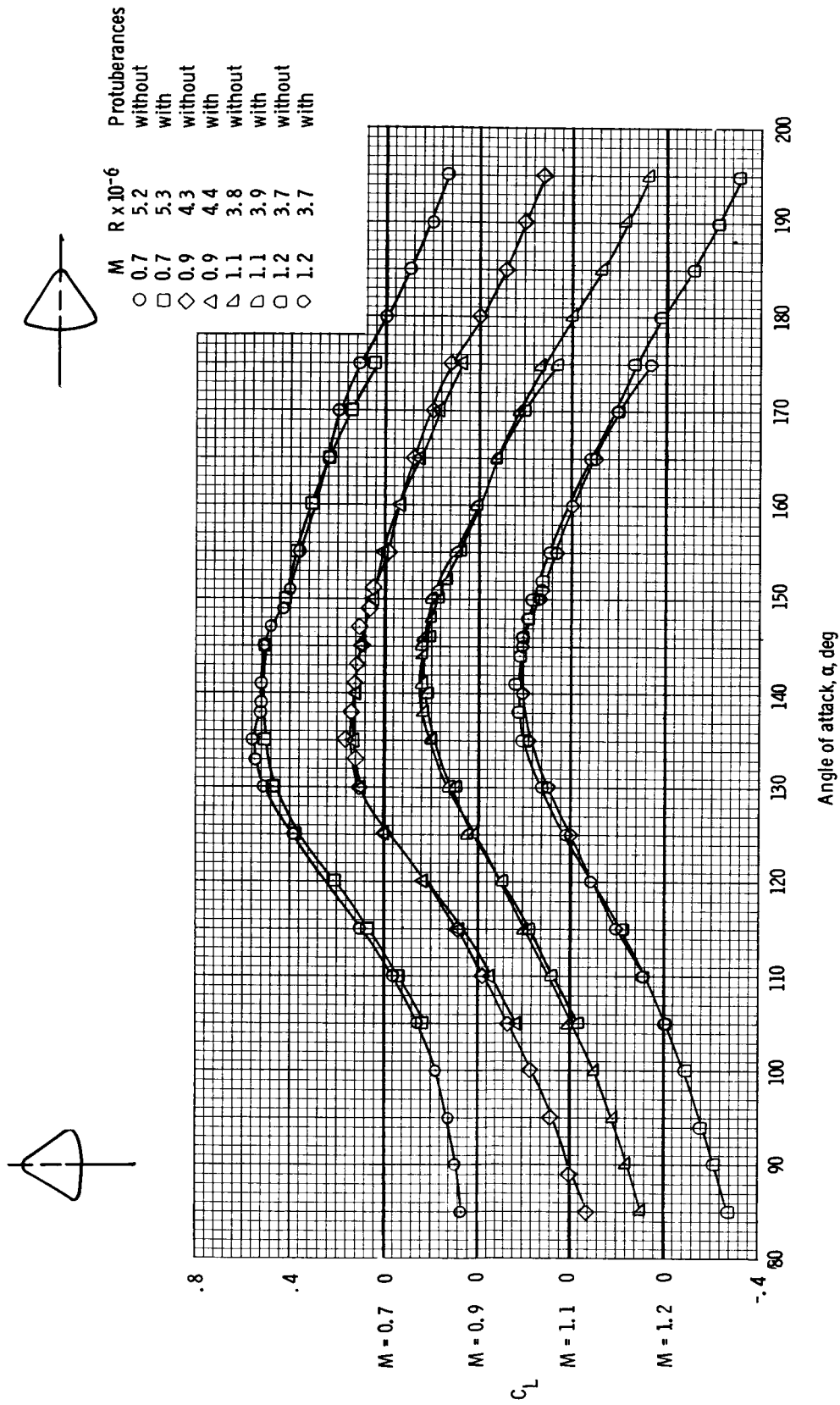
(g) Axial-force coefficient, $M = 0.7$ to 1.2.

Figure 11.- Continued.



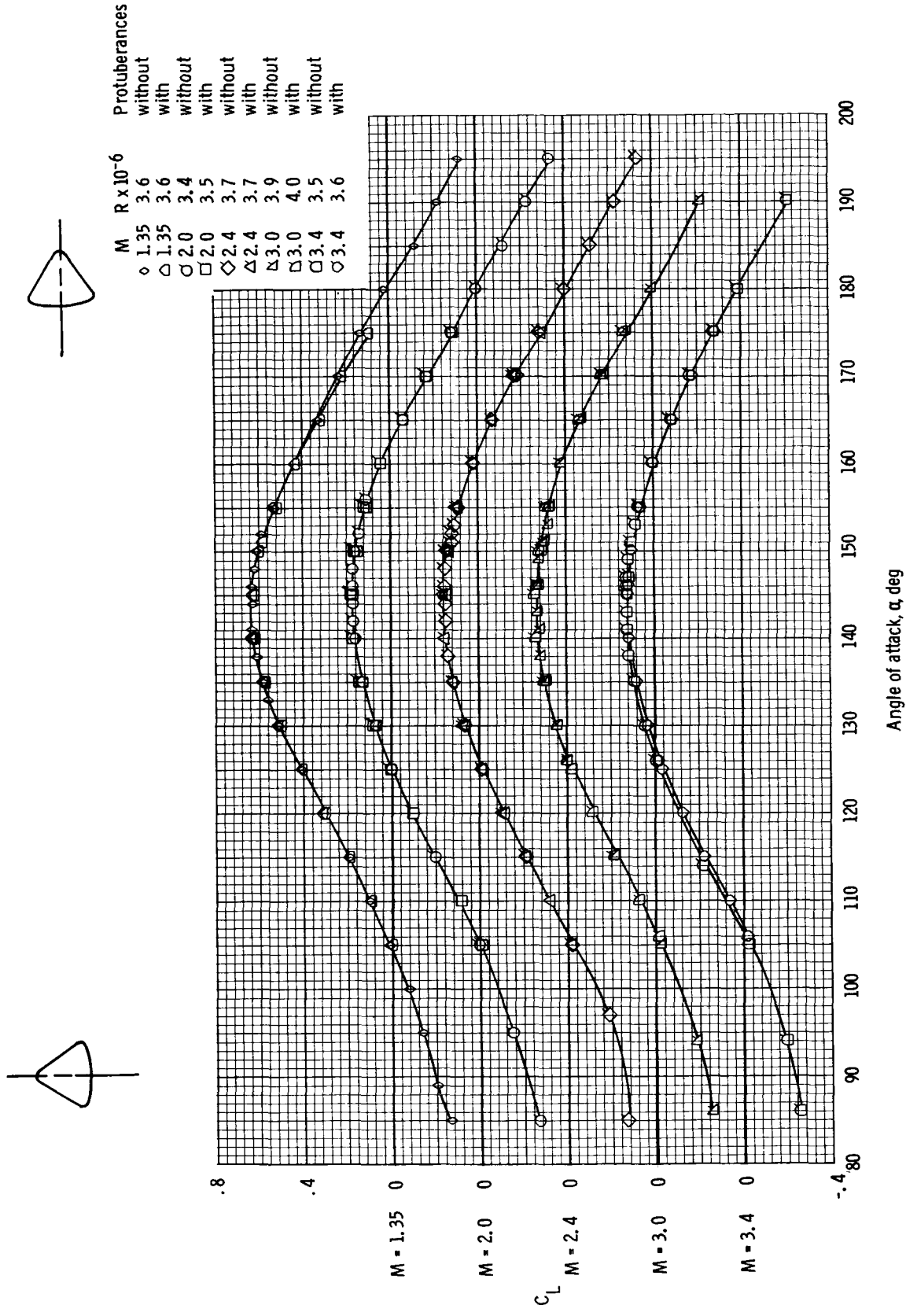
(h) Axial-force coefficient, $M = 1.35$ to 3.4 .

Figure 11. - Continued.



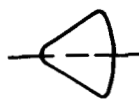
(i) Lift coefficient, $M = 0.7$ to 1.2 .

Figure 11. - Continued.



(j) Lift coefficient, $M = 1.35$ to 3.4 .

Figure 11. - Continued.



M

$R \times 10^{-6}$

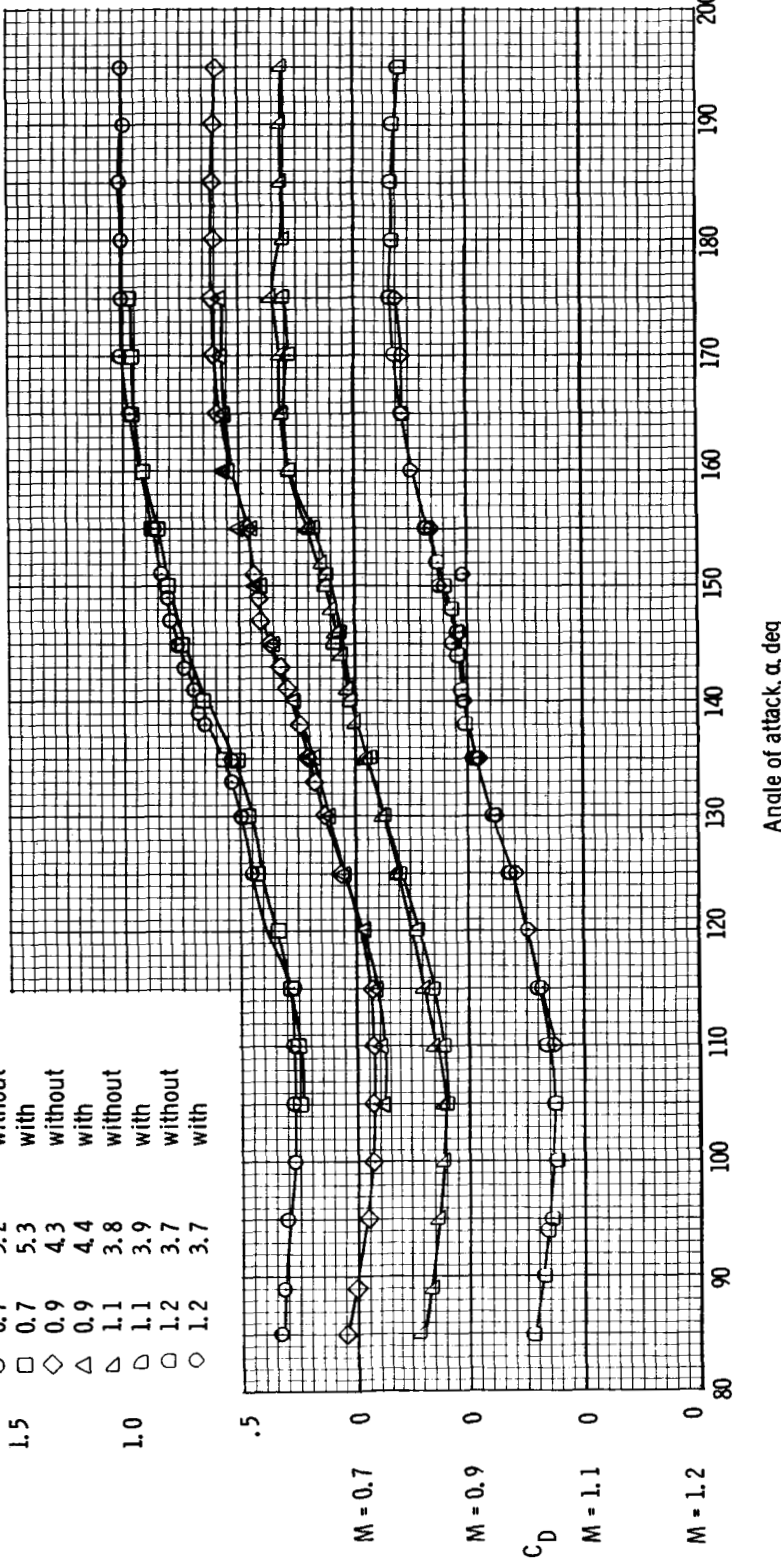
0.7 5.2
0.7 5.3

0.9 4.3
0.9 4.4

1.1 3.8
1.1 3.9

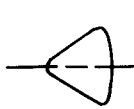
1.2 3.7
1.2 3.7

with
without



(k) Drag coefficient, $M = 0.7$ to 1.2 .

Figure 11. - Continued.



$M = 1.35$

$R \times 10^{-6}$

without protuberances

\diamond 1.35 3.6

\circ 1.35 3.6

with protuberances

\square 2.0 3.4

\circ 2.0 3.4

with protuberances

\square 2.4 3.5

\diamond 2.4 3.5

without protuberances

\triangle 2.4 3.7

\circ 2.4 3.7

with protuberances

\square 3.0 3.9

\diamond 3.0 3.9

without protuberances

\square 3.0 4.0

\circ 3.0 4.0

with protuberances

\square 3.4 3.5

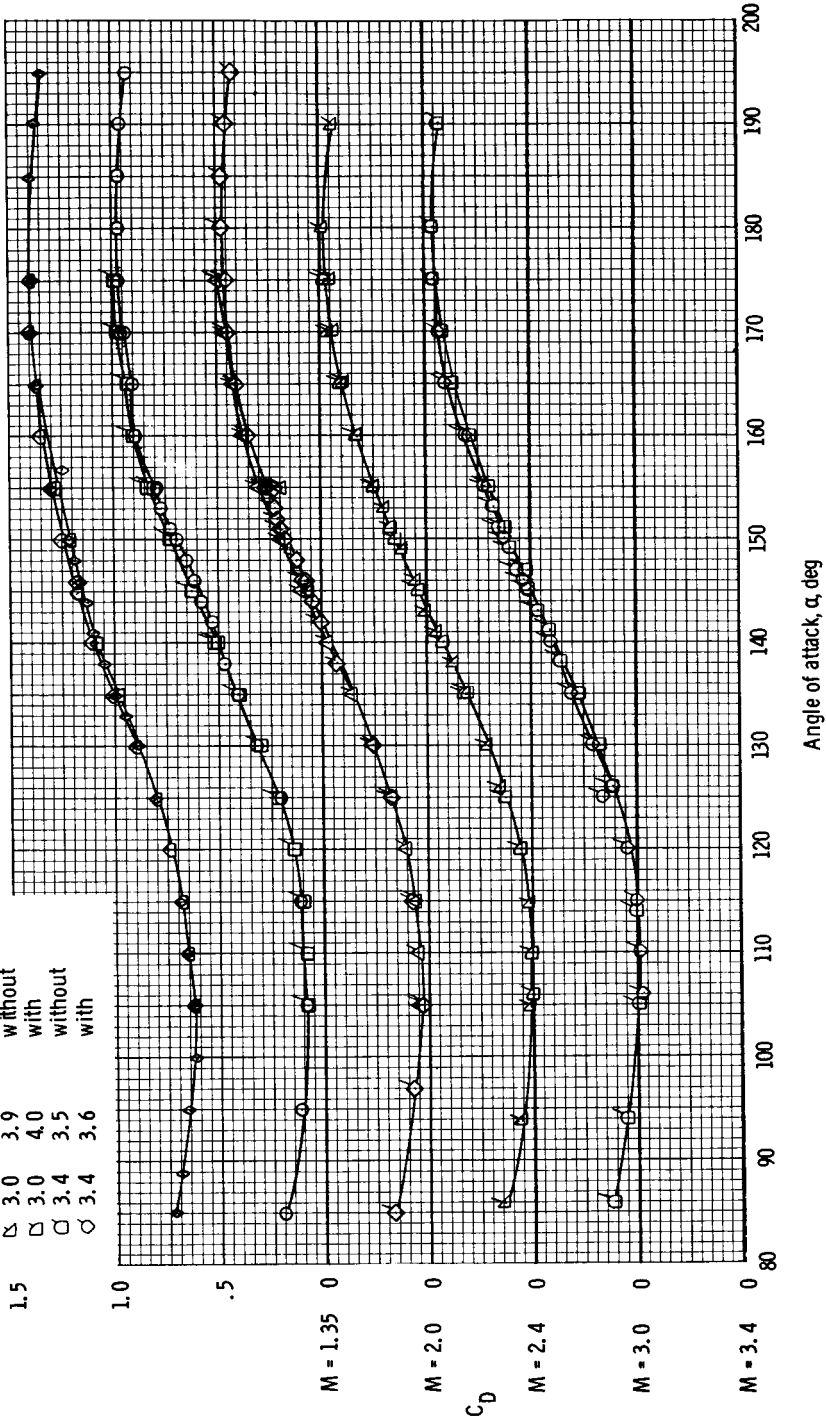
\diamond 3.4 3.5

without protuberances

\square 3.4 3.6

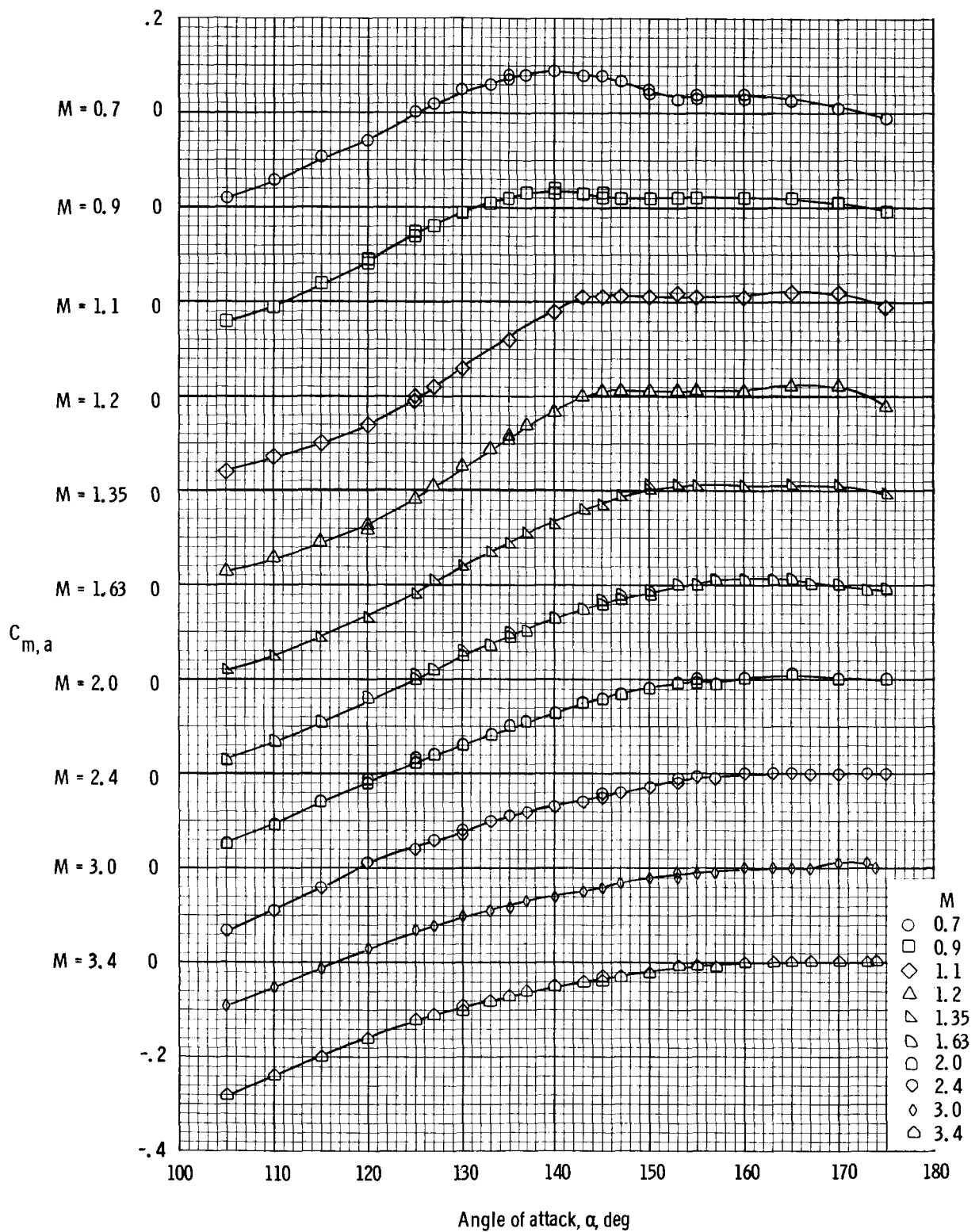
\circ 3.4 3.6

with protuberances



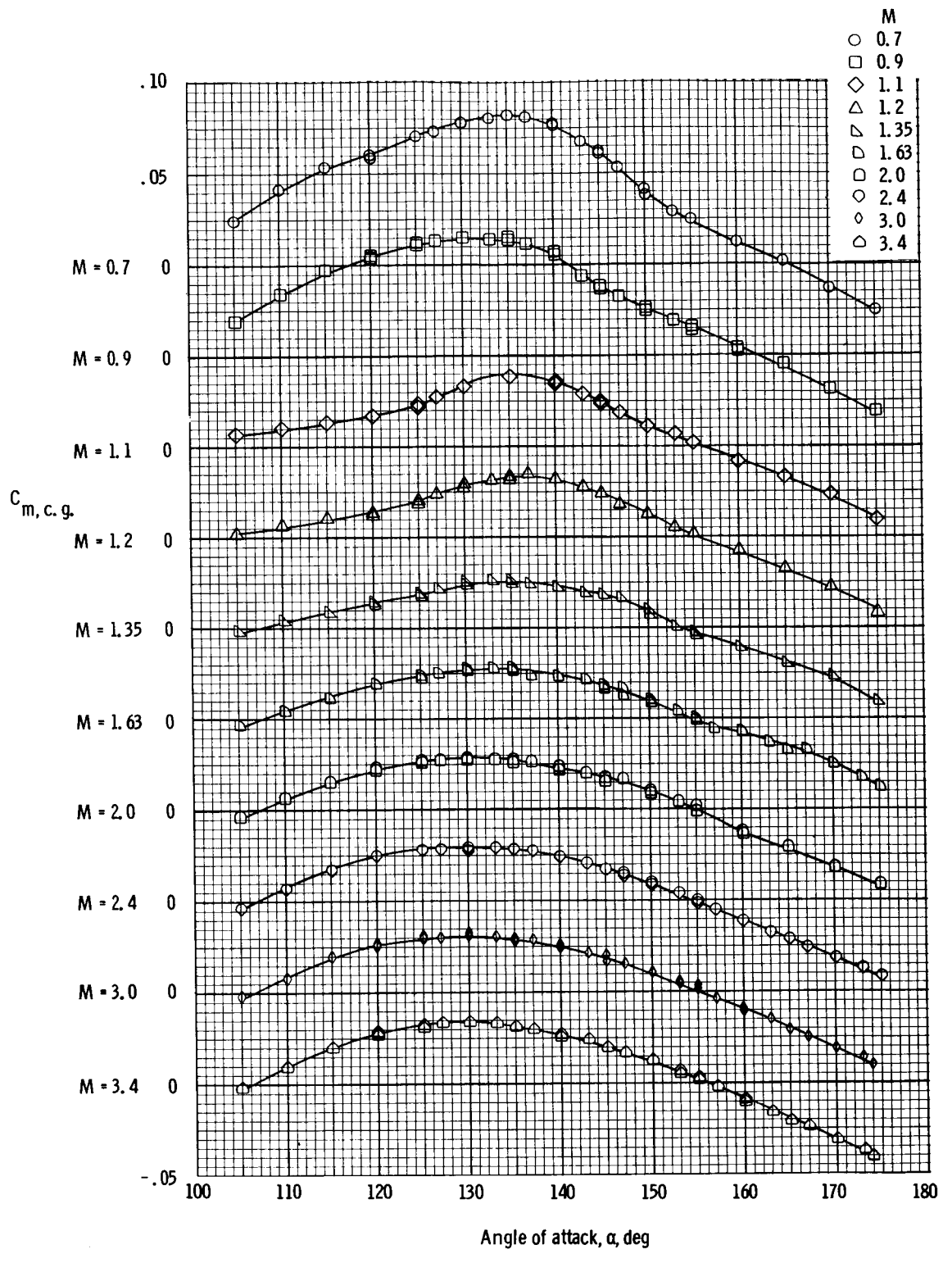
(1) Drag coefficient, $M = 1.35$ to 3.4 .

Figure 11. - Concluded.



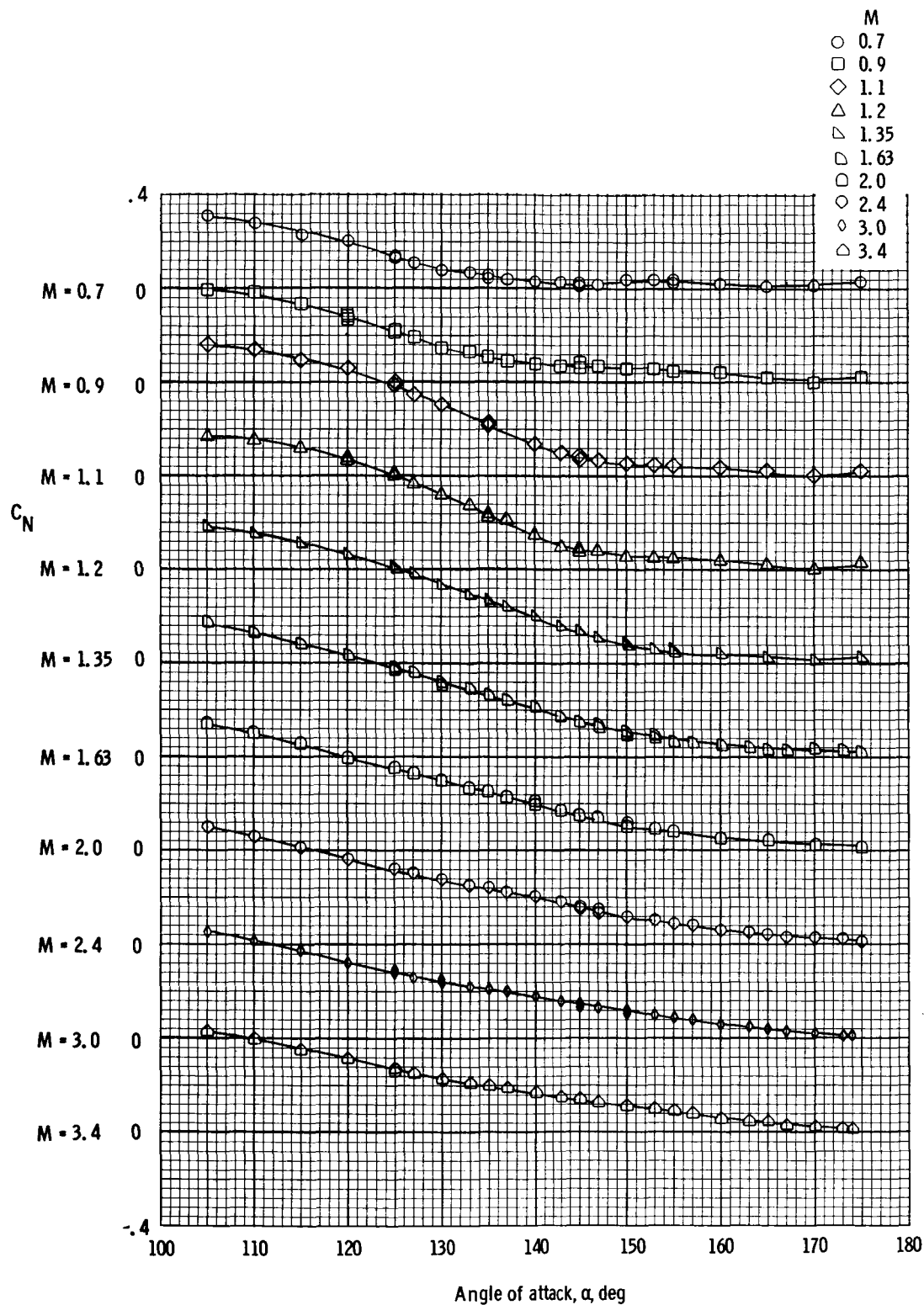
(a) Pitching-moment coefficient, apex.

Figure 12. - Aerodynamic characteristics of the Apollo Block II CM (without protuberances) obtained at Ames UPWT at $M = 0.7$ to 3.4.



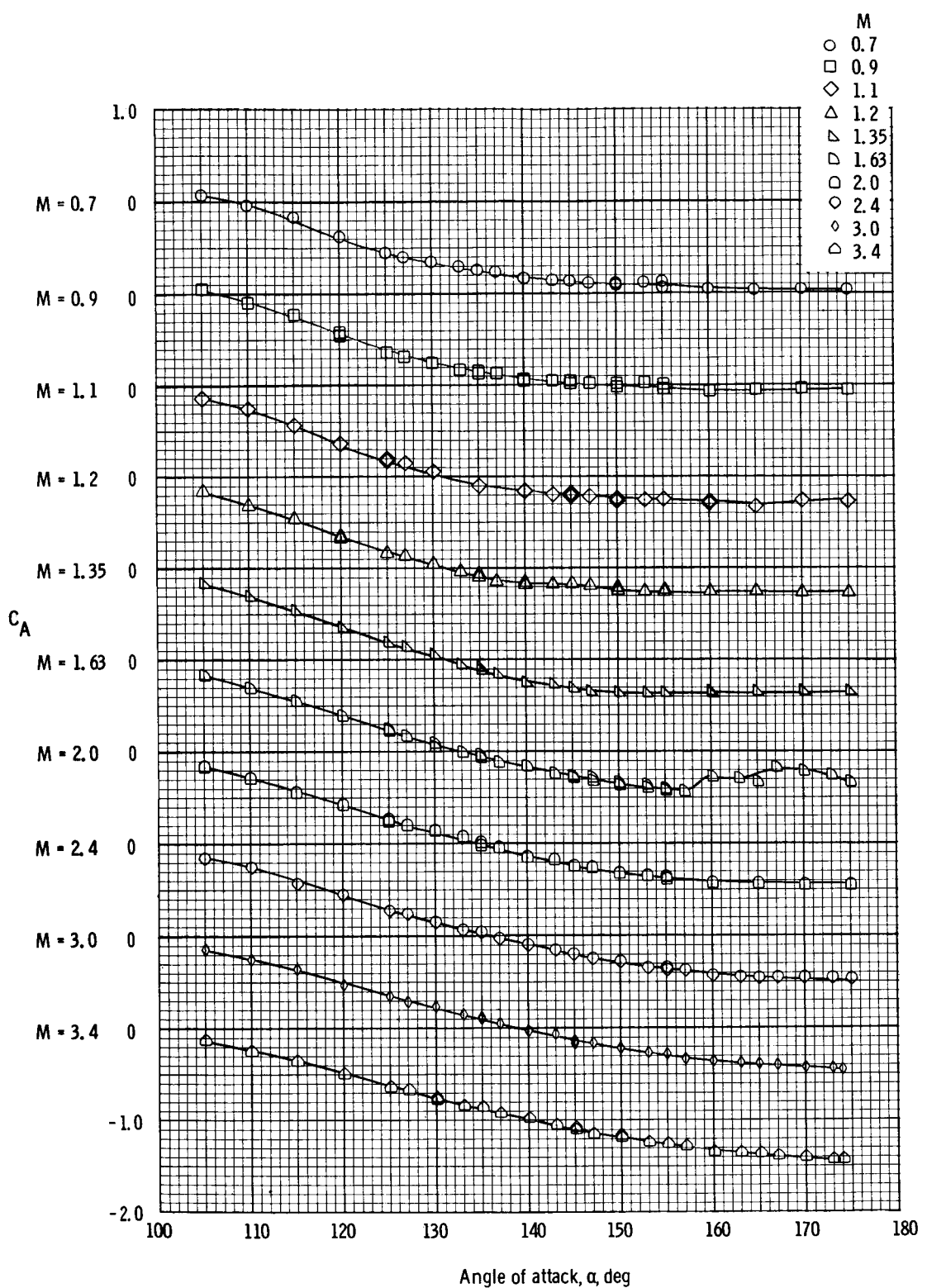
(b) Pitching-moment coefficient, c. g. $\left(\frac{x}{d} = -0.652, \frac{z}{d} = 0.044 \right)$.

Figure 12. - Continued.



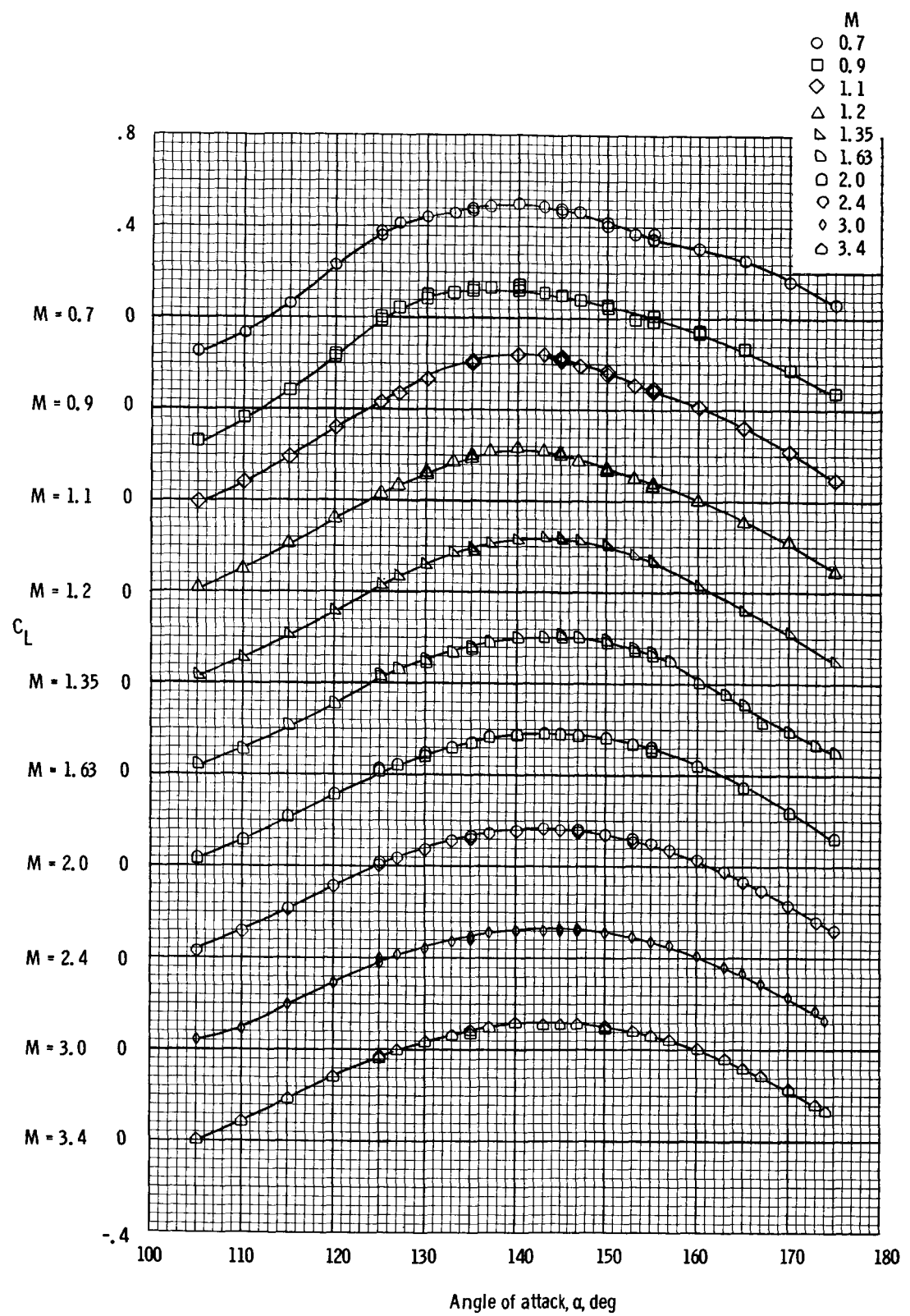
(c) Normal-force coefficient.

Figure 12. - Continued.



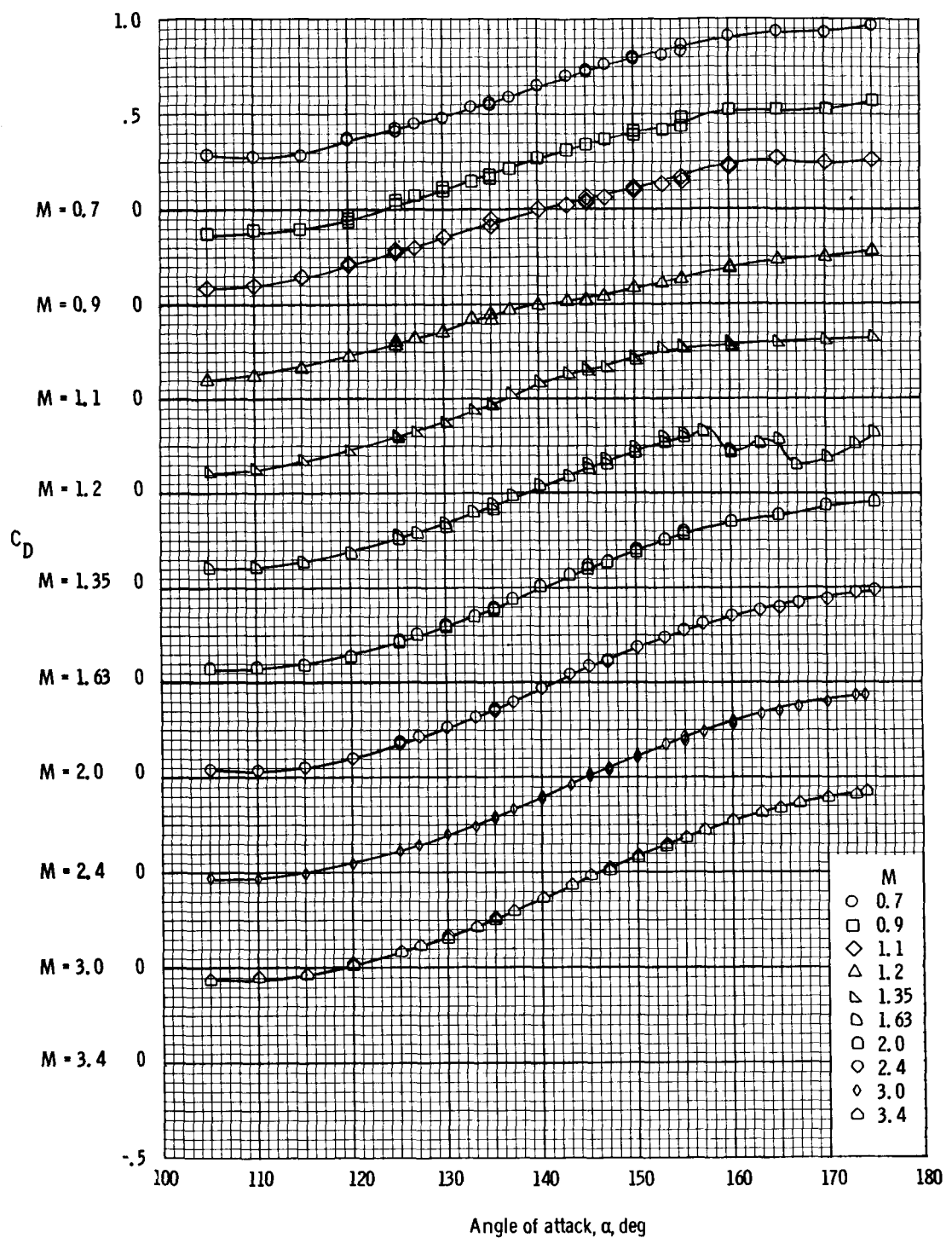
(d) Axial-force coefficient.

Figure 12. - Continued.



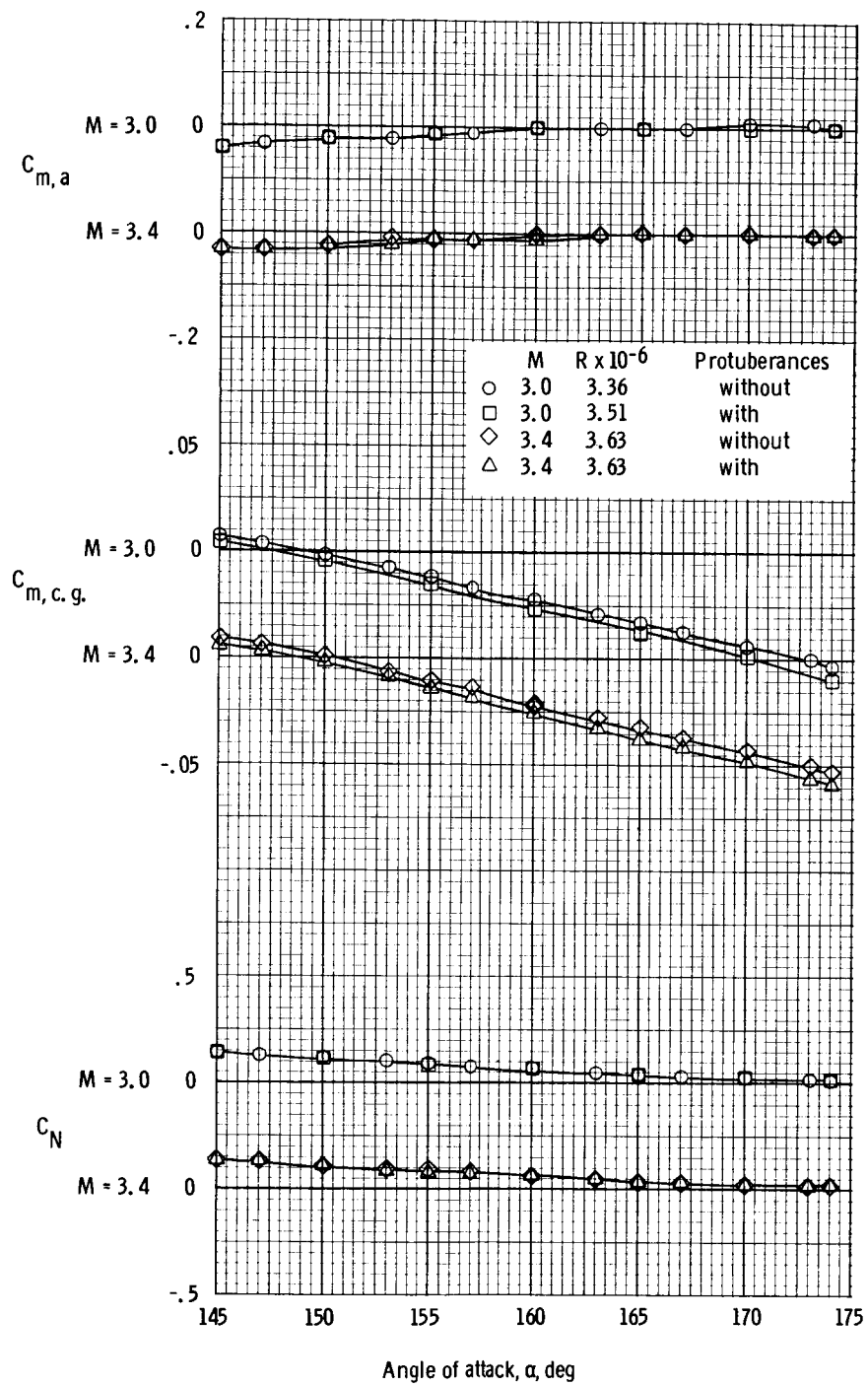
(e) Lift coefficient.

Figure 12. - Continued.



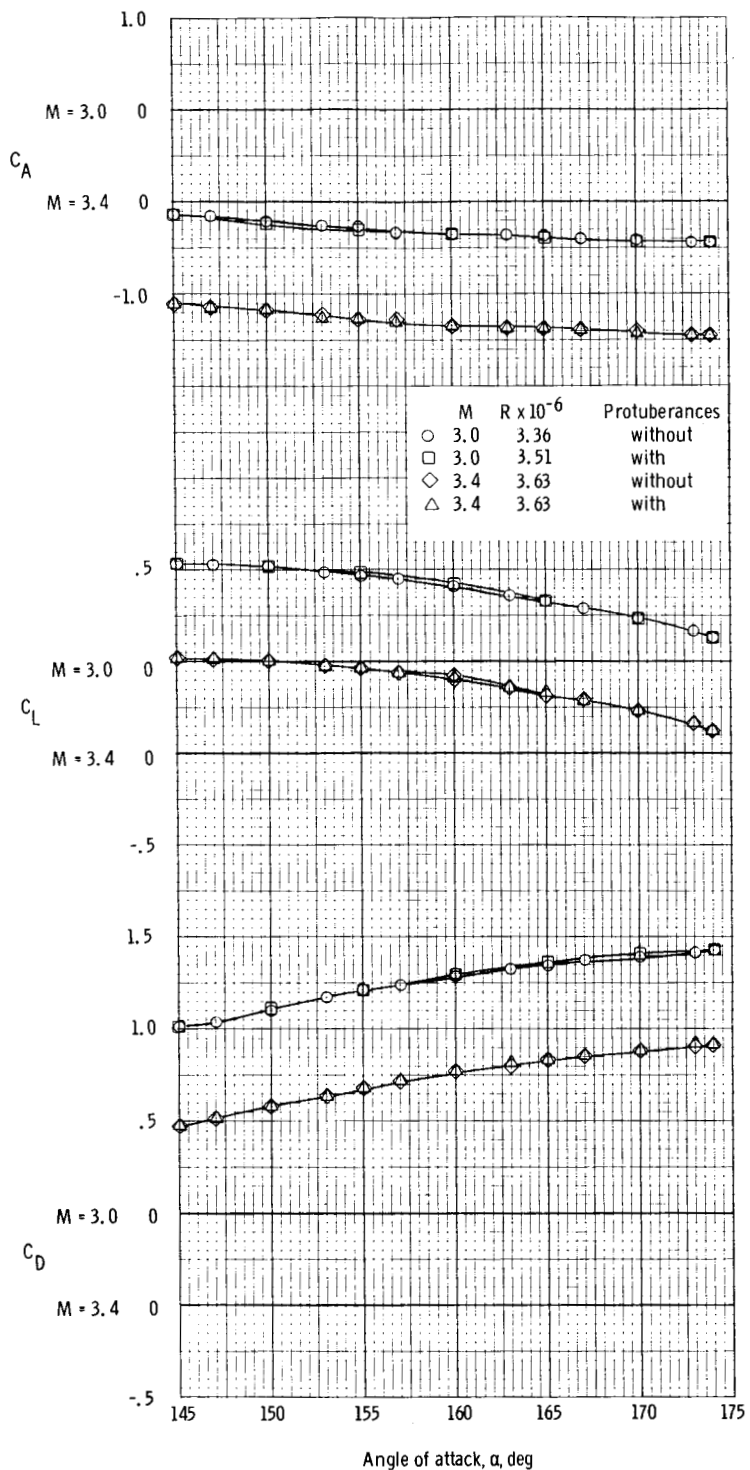
(f) Drag coefficient.

Figure 12. - Concluded.



(a) Pitching-moment and normal-force coefficients.

Figure 13. - Comparison of aerodynamic characteristics of the Apollo Block II CM (with and without protuberances) obtained at Ames UPWT at $M = 3.0$ and 3.4 ($\frac{x}{d} = -0.652$, $\frac{z}{d} = 0.044$).



(b) Axial-force, lift, and drag coefficients.

Figure 13. - Concluded.

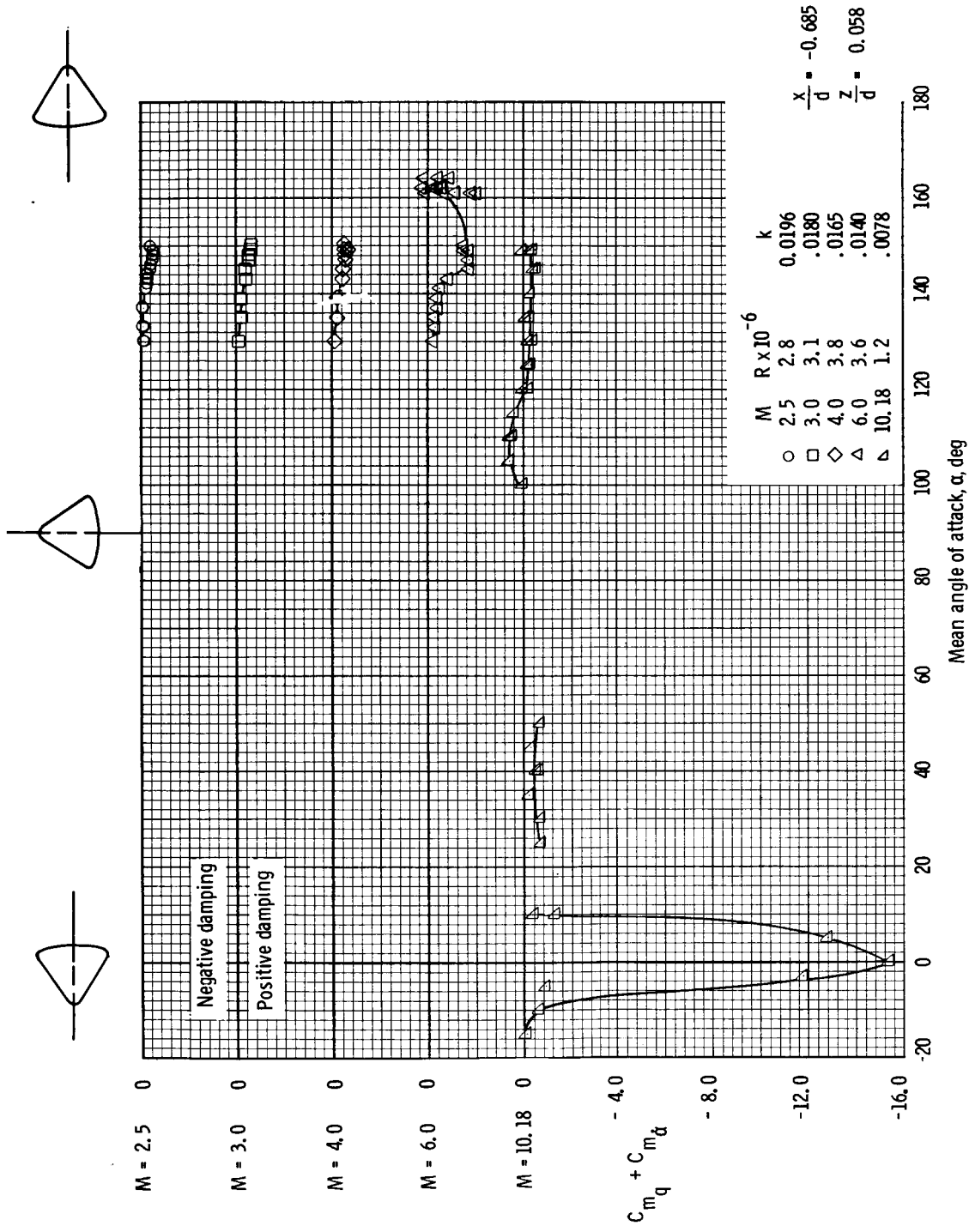


Figure 14. - Longitudinal oscillatory stability derivatives for the Apollo CM (without protuberances) obtained at AEDC-A and -C facilities at $M = 2.5$ to 10.18.

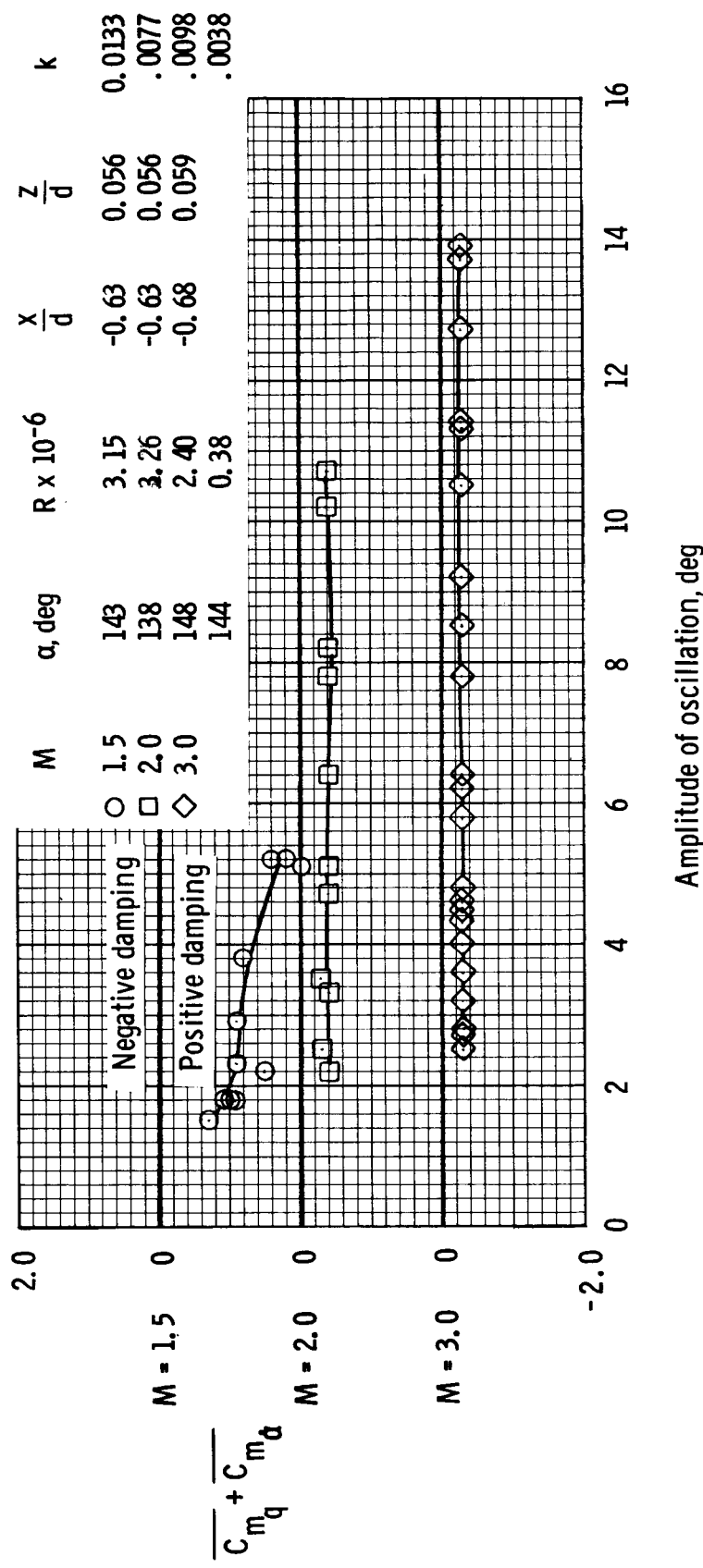


Figure 15.- Longitudinal oscillatory stability derivatives for the Apollo CM (without protuberances) obtained at AEDC-A facilities at $M = 1.5$ to 3.00 .

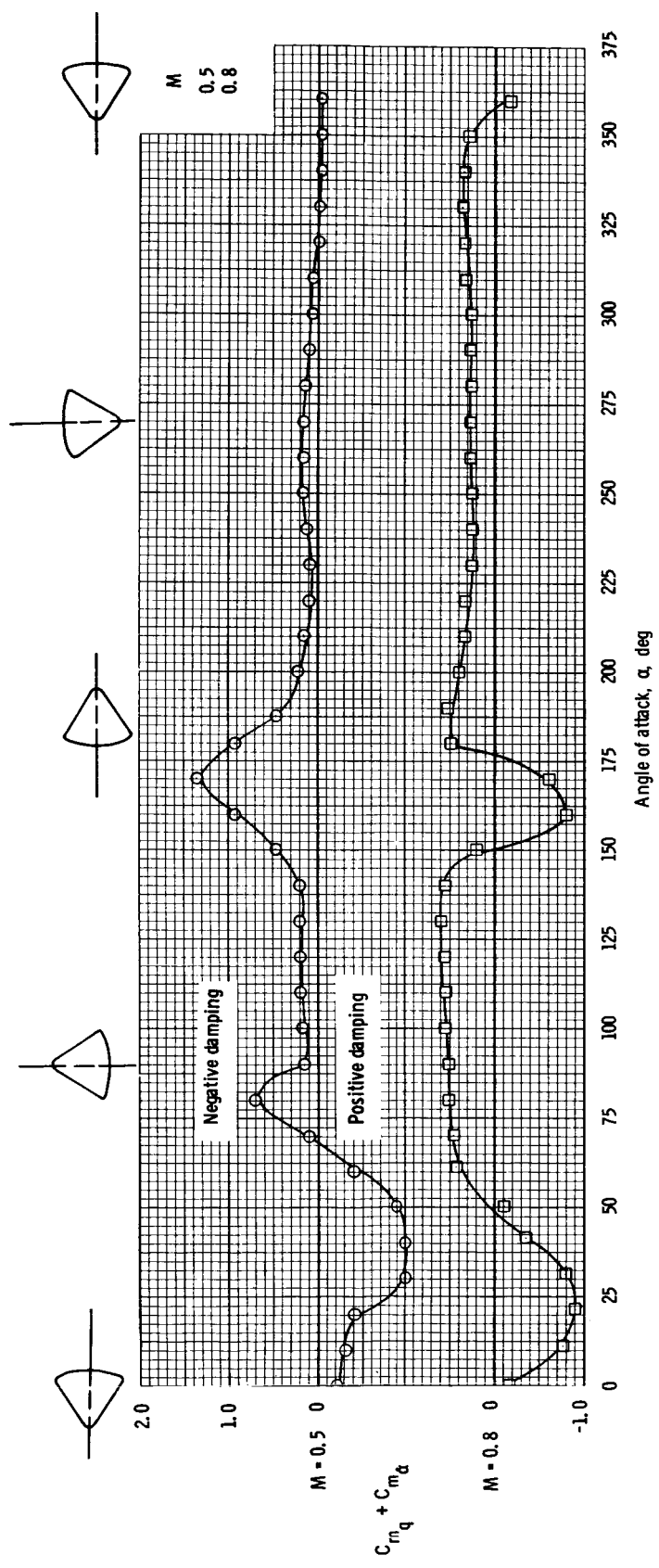


Figure 16. - Longitudinal oscillatory stability derivatives for the Apollo CM (with protuberances) obtained at NAA-TWT facility at $M = 0.5$ and 0.8 .

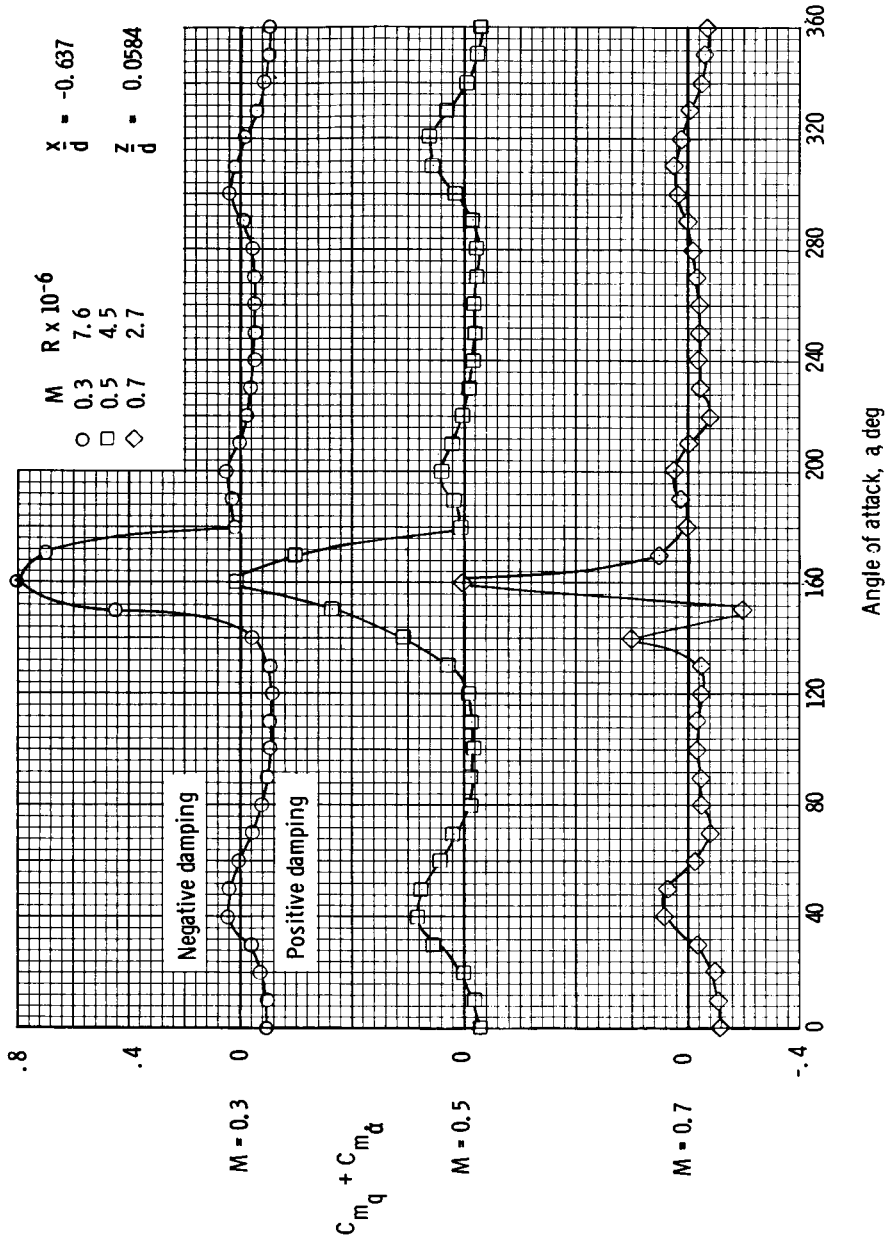
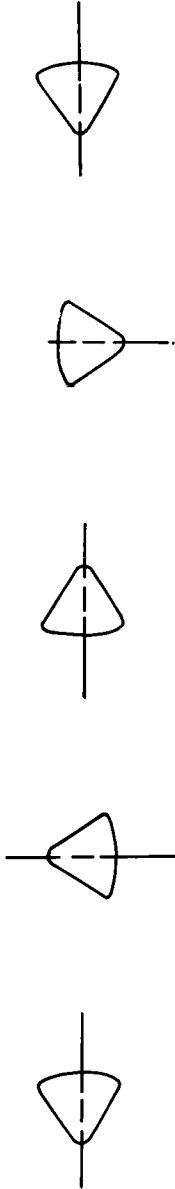
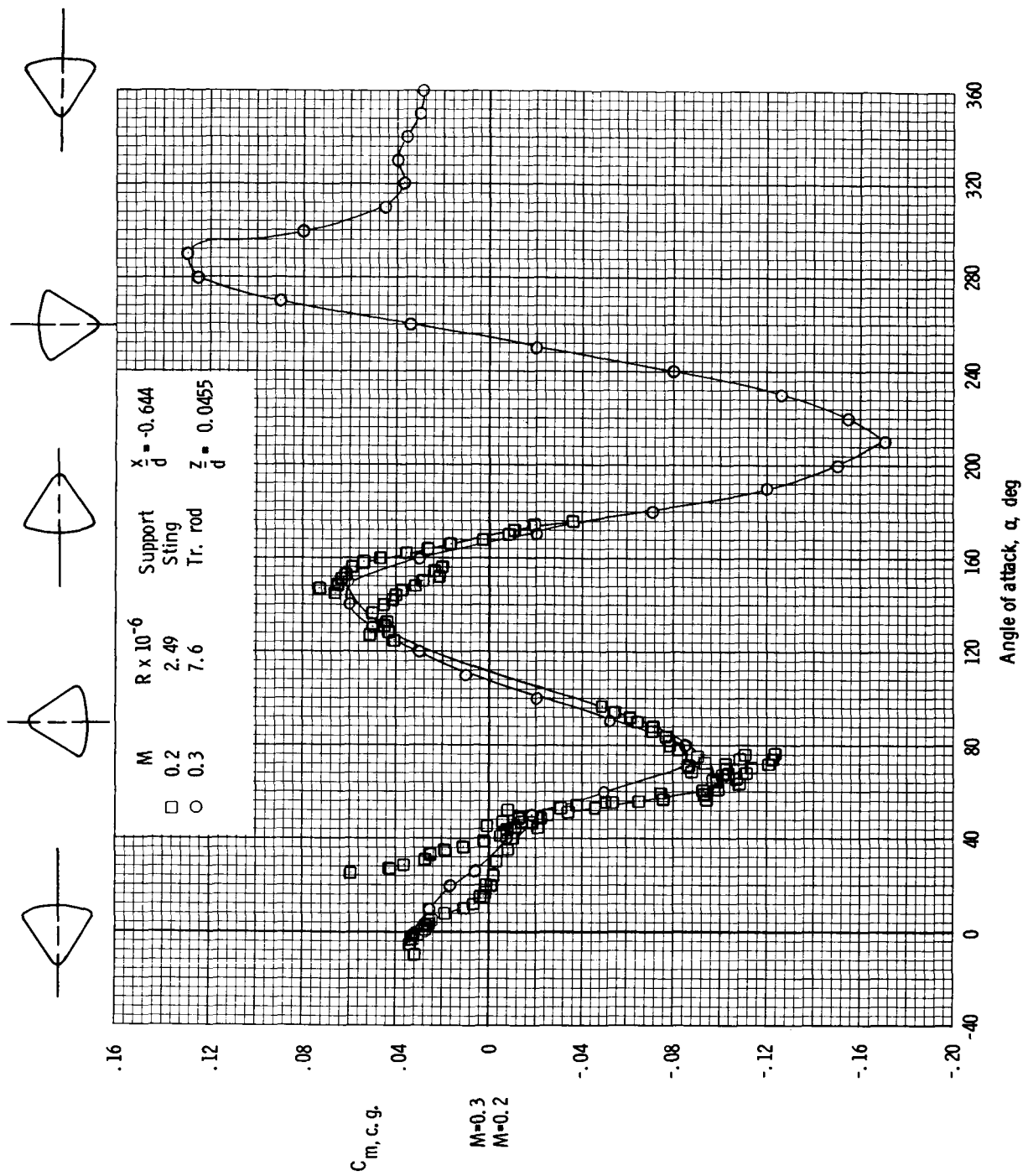
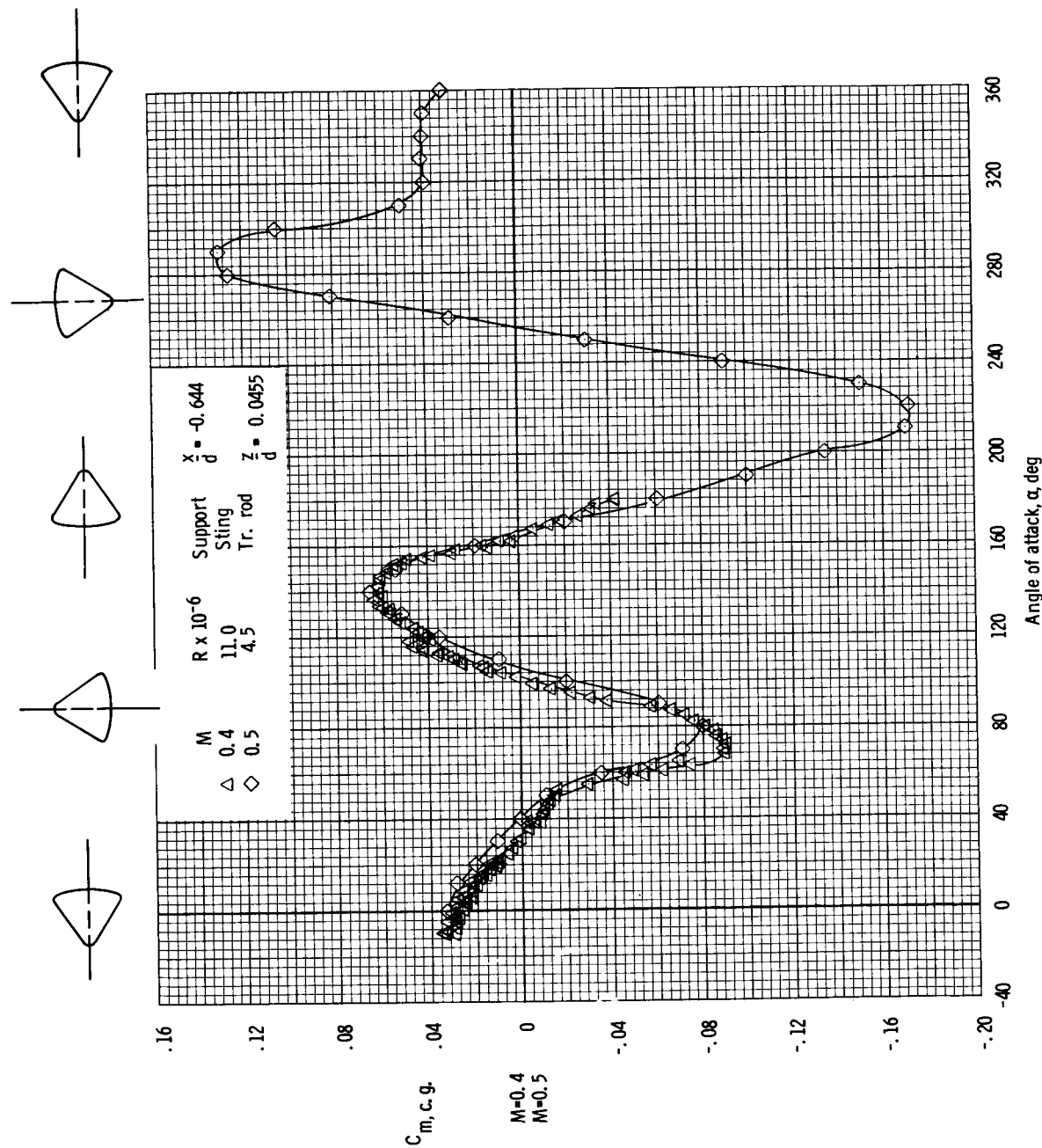


Figure 17. - Longitudinal oscillatory stability derivatives for the Apollo CM (with umbilical fairing, vent, and surviving antenna) obtained at Ames 12-ft facility at $M = 0.3$ to 0.7 .



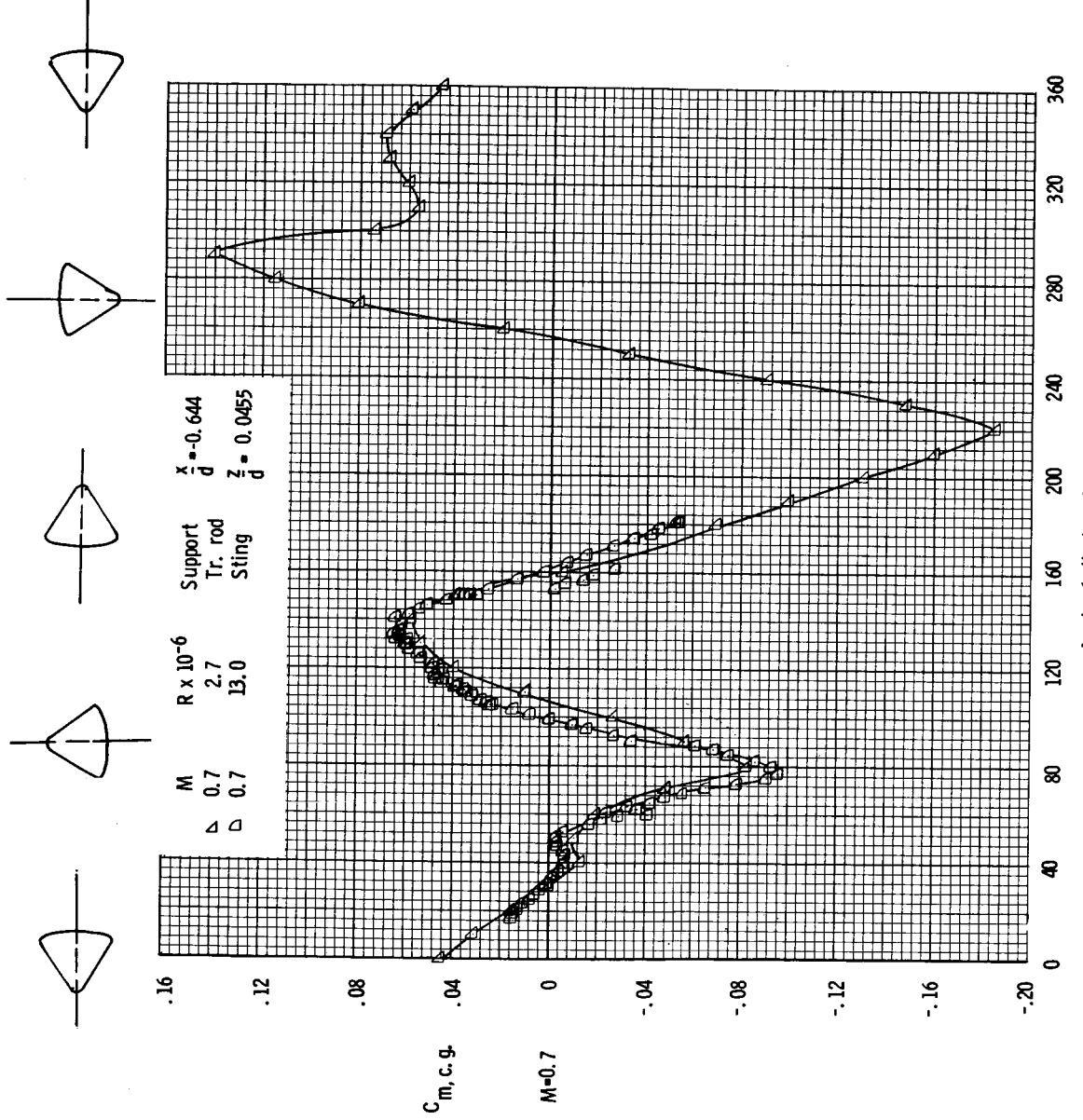
(a) Pitching-moment coefficient for $M = 0.2$ and 0.3 .

Figure 18. - Comparison of C_m values obtained from static tests and dynamic (free-to-tumble) tests at $M = 0.2$ and 0.9 .



(b) Pitching-moment coefficient for $M = 0.4$ and 0.5 .

Figure 18. - Continued.



(c) Pitching-moment coefficient for $M = 0.7$.

Figure 18. - Continued.

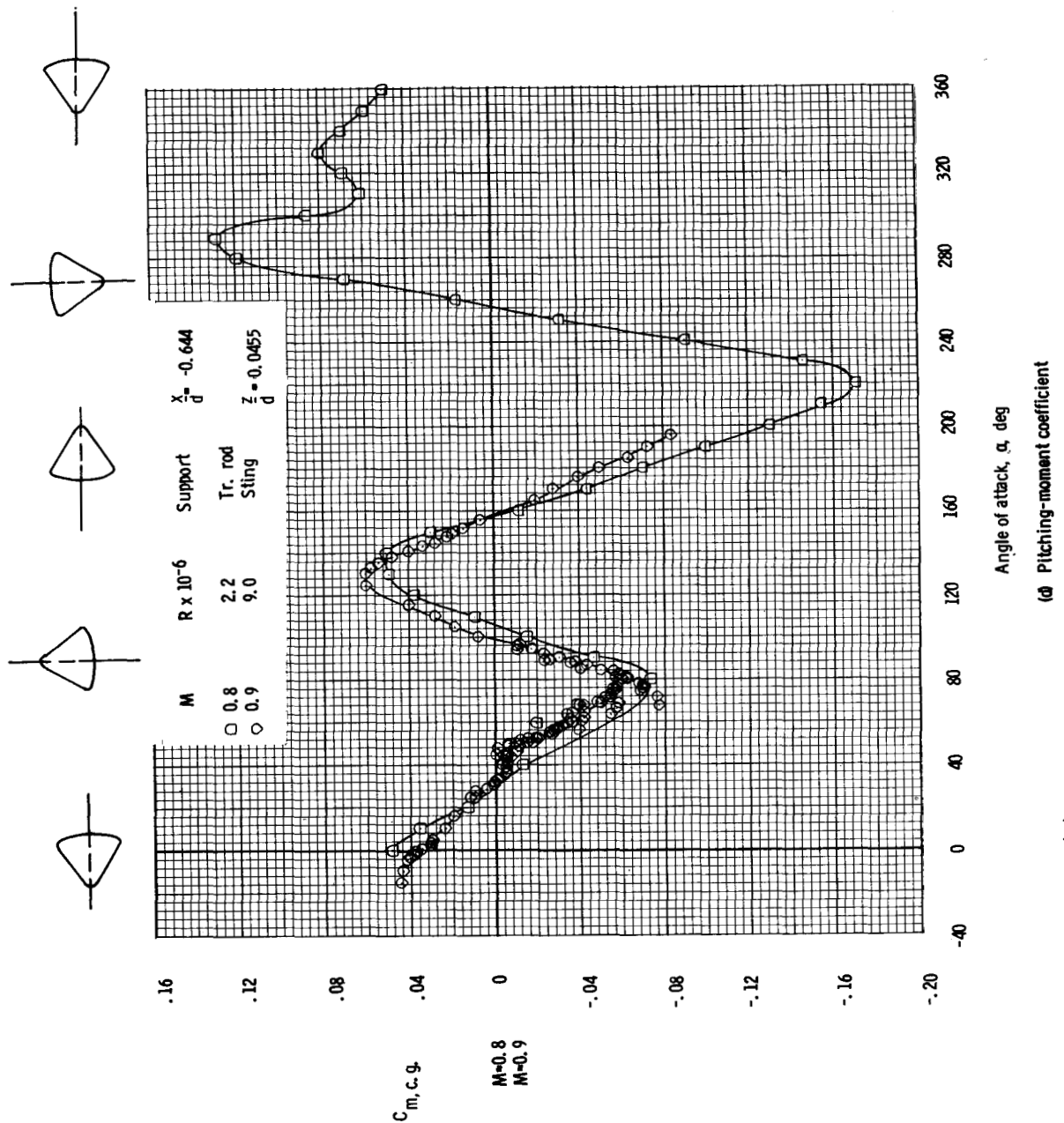
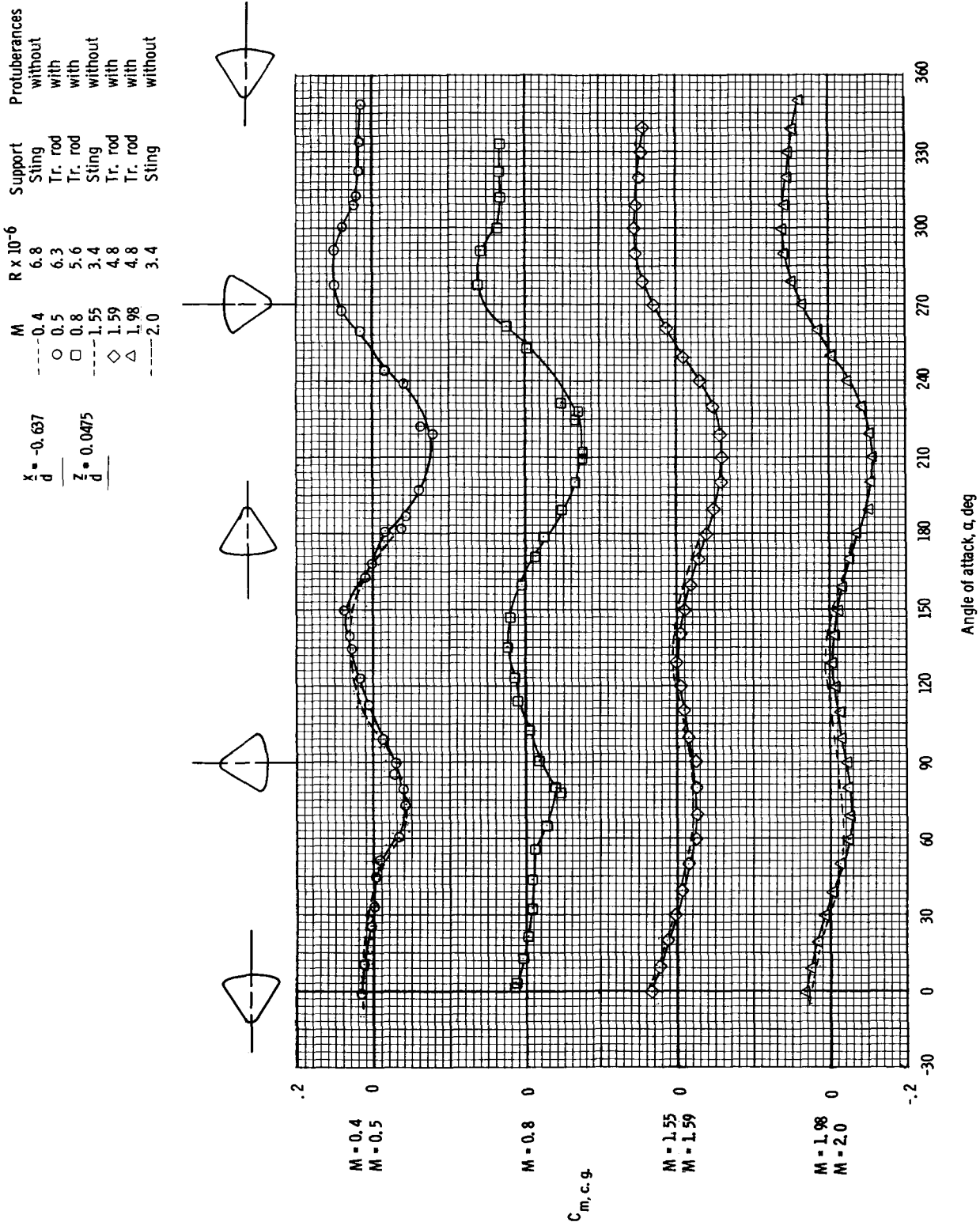


Figure 18.- Continued.

(d) Pitching-moment coefficient for $M = 0.8$ and 0.9 .

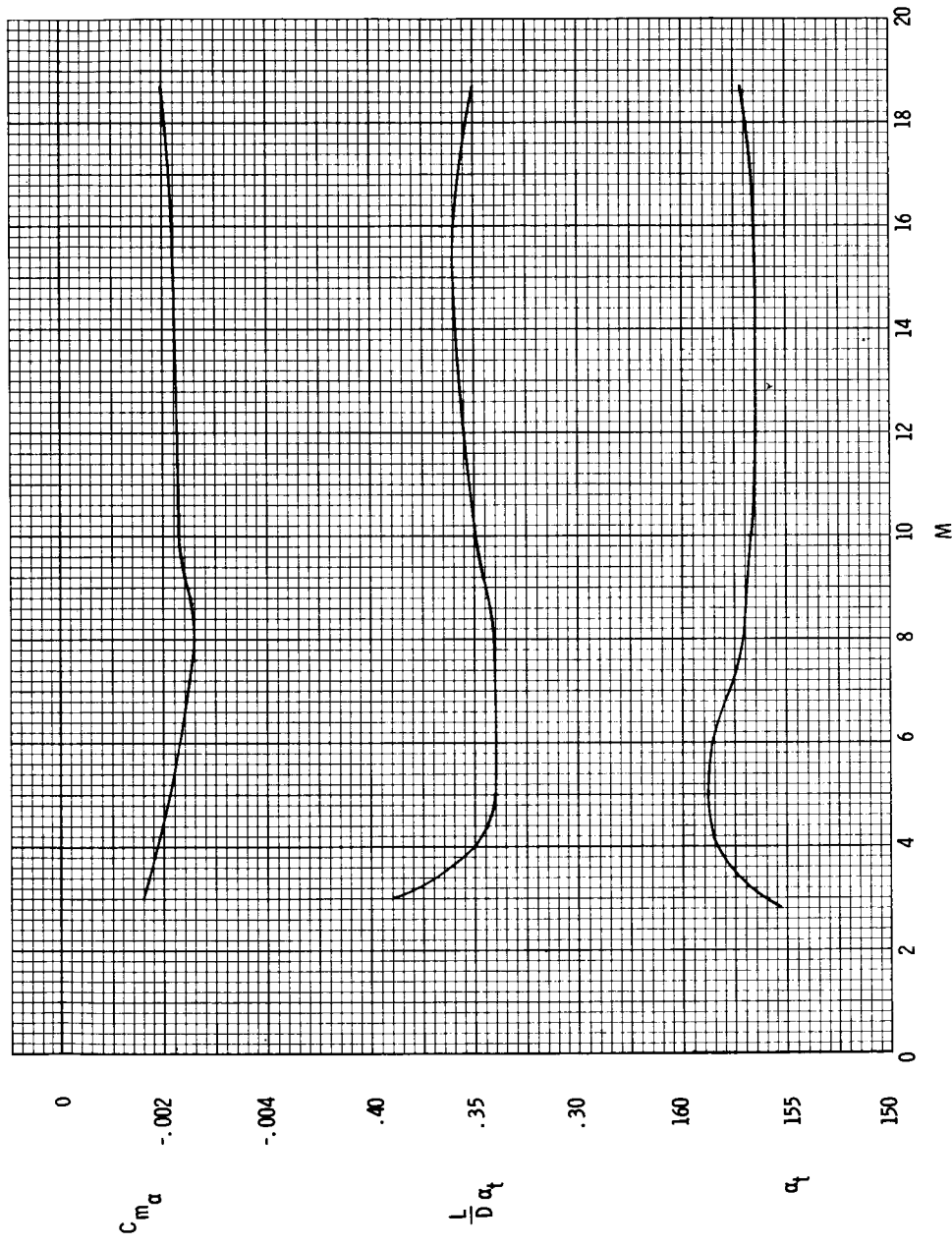


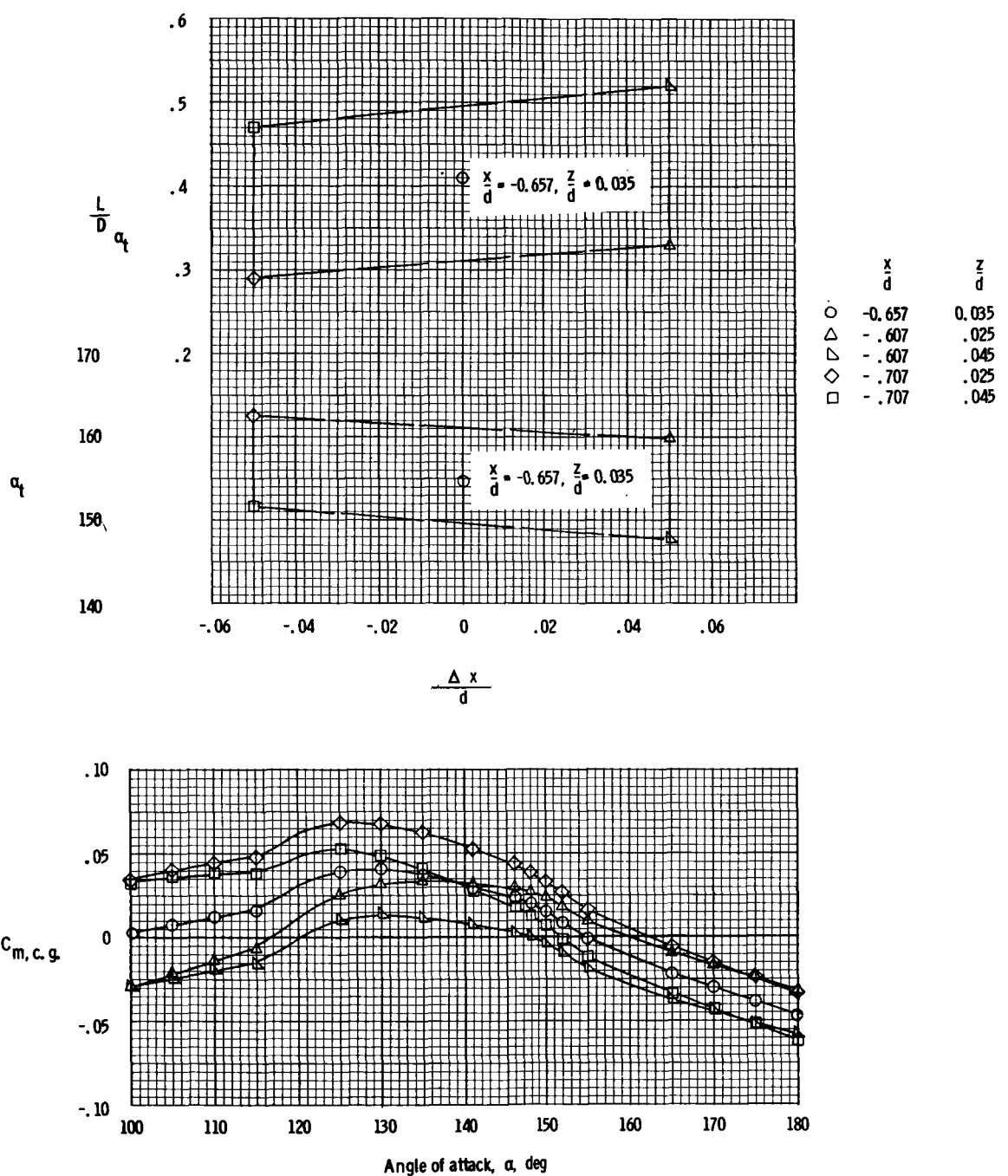
(e) Pitching-moment coefficient for $M = 0.4, 0.5, 0.8, 1.55, 1.59, 1.98$, and 2.0 .

Figure 18. - Concluded.

Nominal c.g. of $\frac{x}{d} = -0.657$, $\frac{z}{d} = 0.035$.

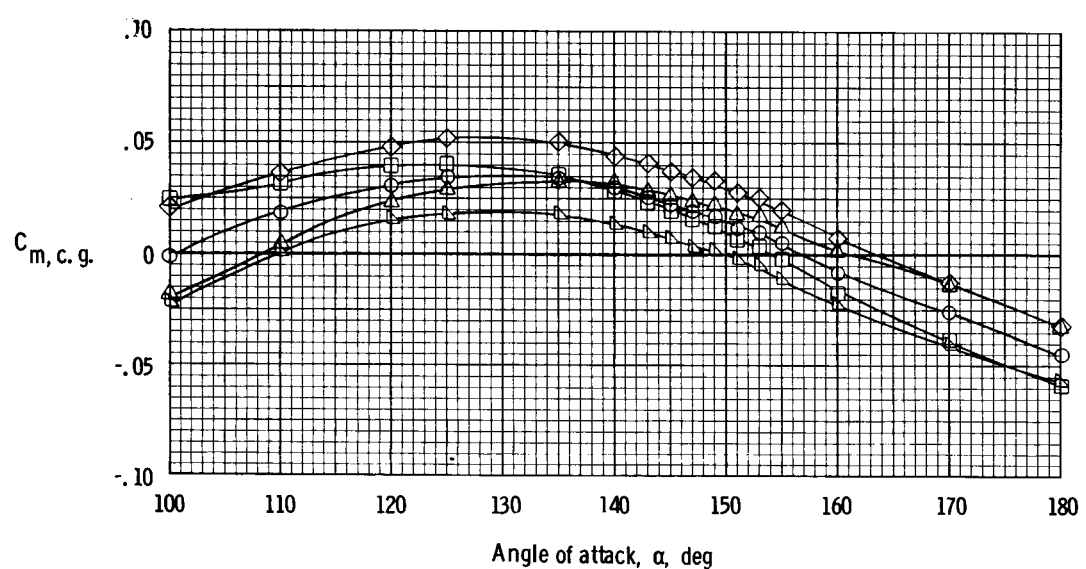
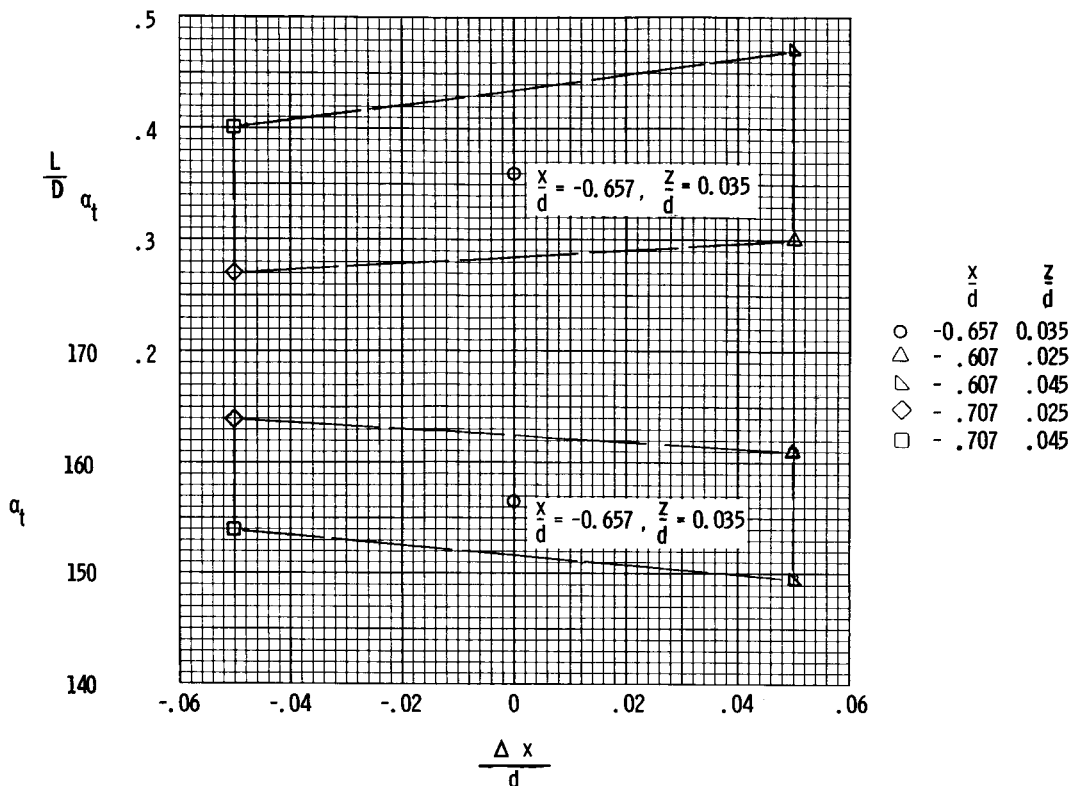
Figure 19. - Summary of the longitudinal stability characteristics of the Apollo CM.





(a) $M = 1.35$.

Figure 20. - Effect of c.g. variation of C_m , α_t , and $\frac{L}{D}$ for the Apollo CM.



(b) $M = 15.8$

Figure 20. - Concluded.